Ferdinand Rissner

SAM-Induced Work Function Modification and Energy-Level Alignment at the Interface between Organic Semiconductors

DIPLOMARBEIT

zur Erlangung des akademischen Grades Diplom-Ingenieur

Betreuer:

Ao.Univ.-Prof. Dipl.-Ing. Dr.techn. Egbert Zojer

Institut für Festkörperphysik

Graz, Februar 2009

EIDESSTATTLICHE ERKLÄRUNG

Ich erkläre an Eides statt, dass ich die vorliegende Arbeit selbstständig verfasst, andere als die angegebenen Quellen/Hilfsmittel nicht benutzt, und die den benutzten Quellen wörtlich und inhaltlich entnommenen Stellen als solche kenntlich gemacht habe.

Graz, am

Unterschrift

To Tatjana,
and to my parents.

Acknowledgements

This work would not have been possible without the help of many people. I would like to thank the colleagues from my group: Anna Track, Oliver Hofmann and Gerold Rangger as well as Georg Heimel from the *Humboldt-Universität Berlin* for inducting me into the computational work and for patient discussions during my diploma thesis.

Tomáš Bučko from the *University of Vienna* provided the GADGET code, which is the basis of an important part of this work. He adjusted it to our purposes and willingly answered my frequent questions concerning the work with this software and the mathematics it employs.

Special thanks go to my supervisor Egbert Zojer who introduced me to scientific work and kindly supported me during this thesis.

Abstract

In the field of organic electronics, self-assembled monolayers (SAMs) are frequently applied to enhance the performance of (opto)electronic devices. Over the past years considerable efforts have been made to better understand the influence of SAMs on surface properties. In particular, it has been shown that the deposition of self-assembled monolayers on metals can cause significant work function modifications. It is essential to understand to what extent a modification of the electrode work function can be directly translated into a change of the electron and hole injection barriers into an organic semiconductor (OSC) on top of the SAM, i.e., it needs to be tested under which conditions the simple Schottky-Mott limit applies.

Density functional theory based slab-type band-structure calculations were performed, adopting the VASP code. In order to model metal/SAM/organic interfaces, three-component systems were investigated, consisting of a metal surface, a SAM, and a monolayer of a prototypical organic semiconductor on top of the SAM. By varying the nature of the SAM interlayer, regions of Fermi level pinning and vacuum level alignment can be distinguished, where the former is found to be a consequence of polarization of the SAM in addition to significant charge transfer at the SAM/OSC interface.

Additionally, the geometry of a prototypical low coverage metal/SAM system was optimized in Cartesian as well as internal coordinates. A significant impact of the applied set of coordinates on the resulting geometry was found. The preliminary results suggest a very weak dependence of the total energy on the tilt angle of the SAM molecules.

Kurzfassung

In der organischen Elektronik werden selbst-assemblierte Monolagen (SAMs) geeigneter organischer Moleküle zur Steigerung der Effizienz (opto)elektronischer Bauelemente verwendet. Die Fähigkeit von SAMs Oberflächeneigenschaften von Materialien gezielt zu verändern, war Gegenstand intensiver Untersuchungen der letzten Jahre. Im Speziellen konnte gezeigt werden, dass SAMs auf Metalloberflächen die metallische Austrittsarbeit zu verändern vermögen. In Bauelementen werden durch die Einstellung der Austrittsarbeit einer Elektrode die Ladungsträgerinjektionsbarrieren in einen angrenzenden organischen Halbleiter optimiert. Daher ist es von Bedeutung zu verstehen, in welchem Ausmaß dies möglich ist.

Im Rahmen dieser Arbeit wurden auf der Dichtefunktionaltheorie basierende Bandstrukturrechnungen durchgeführt, um die elektronische Struktur an derartigen Dreikomponentensystemen (Metall + SAM + organischer Halbleiter) zu bestimmen. Der sogenannte "slab-approach" ermöglichte die Simulation solcher Grenzflächen. Durch Variation der chemischen Struktur der SAM konnte die Austrittsarbeit an einer Au(111)-Oberfläche um mehrere Elektronenvolt verändert werden. Allerdings lassen sich nur in einem bestimmten Energiebereich die Injektionsbarrieren in den organischen Halbleiter einstellen. Die außerhalb dieses Bereiches auftretenden Pinningeffekte am Ferminiveau des Metalls sind interessanterweise nicht auf einen Ladungstransfer zwischen organischem Halbleiter und Metall, sondern auf Ladungstransfer zwischen SAM und Halbleiter begleitet von Polarisationseffekten innerhalb der SAM zurückzuführen.

Weiters wurde der Einfluss der verwendeten Art von Koordinaten (kartesische vs. interne Koordinaten) auf das Ergebnis von Geometrieoptimierungsrechnungen von SAMs auf Metalloberflächen untersucht. Ein signifikanter Einfluss speziell auf den Kippwinkel der Moleküle wurde für kleine Packungsdichten der SAM gefunden. Interessanterweise scheint der Kippwinkel laut der vorläufigen Ergebnisse dieser Untersuchungen jedoch nur geringen Einfluss auf die Gesamtenergie des Systems zu haben.

Contents

1 Introduction

In organic electronics, the performance of devices strongly depends on the energy level alignment at interfaces between different functional materials. It is of great significance to understand and control the energy level alignment at such interfaces [1, 2, 3, 4, 5, 6]. For organic (opto)electronic devices such as thin film transistors (OTFTs), light emitting devices (OLEDs) or photovoltaic cells (OPVs), deviations from an optimum charge carrier injection barrier often imply a significant loss of efficiency [7, 8]. A method of optimizing the device performance is the application of self-assembled monolayers (SAMs) between the electrode and the active organic semiconductor (OSC) material. SAMs allow adjusting the work function Φ of an electrode, and therefore also the injection barriers, over a range of several electron volts (eV) [9, 10, 11, 12, 13, 14, 15]. Over the last years, considerable effort has been directed towards understanding the mechanisms that govern SAM-induced work function modification ($\Delta\Phi_{\mathrm{SAM}}$) [1, 4, 16, 17, 18].

As a next step, the consequences of $\Delta\Phi_{\mathrm{SAM}}$ on the level alignment at metal/SAM/OSC heterojunctions [19] are to be investigated. For applications, it is crucial to understand to what extend $\Delta\Phi_{\mathrm{SAM}}$ can be directly translated into a change of electron and hole injection barrier, i.e., the simple Schottky-Mott limit (vacuum level alignment) [4, 20] often observed at organic/organic heterojunctions applies. To address this problem, DFT calculations on three component systems, consisting of an Au(111) surface, a SAM interlayer, and an additional monolayer of a prototypical OSC on top of the SAM are performed in this diploma thesis. The latter represents the bulk of an organic semiconducting material.

In Chapter 2, an overview over the main concepts used in this work and a general description of the investigated systems is given.

Chapter 3 goes into detail about the applied methodology for the calculations, i.e., introduces DFT and explains some of the parameters important for assuring convergence of the numerical computations.

In Chapter 4, the SAMs which are used as interlayers in the investigated systems are presented. Comprehensive results on the energetics of most of them have already been published [21] and are roughly summarized here. Also, some additional metal/SAM systems were investigated and are presented in somewhat more detail.

The main results of the work, i.e., the calculations on the full three component systems, can be found in Chapter 5.

Finally, Chapter 6 deals with a methodological issue. Traditionally, band structure codes make use of Cartesian coordinates in geometry relaxation calculations. In many classical solid state band structure calculations there is no need for specially adapted systems of coordinates. In absence of rigid objects - such as molecules - which imply strong correlations between the ionic degrees of freedom, Cartesian coordinates perform well. Also the

optimizers integrated in the Vienna ab-initio Simulation Package (VASP) code, which is used in our group, make use of Cartesian coordinates.

For molecules, sets of so-called *internal coordinates* exist, which very efficiently describe molecular degrees of freedom. The impact of such coordinates on the geometry optimization process of a metal/SAM system is tested in this chapter. For this purpose, a tool called GADGET [22] is employed. The yet quite preliminary results on the impact of the chosen set of coordinates on the relaxation of metal/SAM systems are presented here.

2P biphenyl

BD bond dipole

CCDC Cambridge Crystallographic Data Centre

DFT Density Functional Theory

DIIS direct inversion in the iterative subspace

DOS density of states

EA electron affinity

EIB electron injection barrier

HIB hole injection barrier

HOMO highest occupied molecular orbital

HOPS highest occupied π-states

ID interface dipole

IP ionization potential

LUMO lowest unoccupied molecular orbital

LUPS lowest unoccupied π-states

MD molecular dynamics

OSC organic semiconductor

SAM self-assembled monolayer

VASP Vienna ab-initio Simulation Package

2 Main concepts & topics of the work

2.1 The work function Φ of metals

Literature: Refs. [23] & [1].

The work function Φ of a metal is often defined as the minimal energy necessary to remove an electron from the metal to the vacuum region *infinitely far* away from the metal surface, with zero kinetic energy remaining for the electron [1]. In a different, equivalent formulation, the electron is at *vacuum level at infinite distance* (VL (∞)). It is important to note that very often the energy to remove an electron from the metal to the vacuum region *near* the metal surface is a more convenient quantity; the electron is then said to be at *vacuum level at surface* (VL (s)). In the following, Φ refers to the latter definition. To clarify the difference between the two definitions and to understand which parameters influence Φ, one has to take a look at (i) the energy distribution of the electrons in a metal [23] and (ii) the shape of the electron potential energy near its surface [1].

Electrons as fermions obey the Fermi-Dirac statistics. According to this energy distribution, no more than two electrons (with counteracting spin) occupy the same quantum mechanical state. Due to energy minimization, at 0 K they occupy the states lowest in energy. This implies, that in a system at zero temperature all states up to a certain energy E_F are occupied, and none above E_F. The influence of a finite temperature T is to weaken this step-like distribution, yielding a nonzero propability of states with energies $\epsilon > E_\mathrm{F}$ and correspondingly a propability smaller than 1 for states with $\epsilon < E_\mathrm{F}$ for being occupied, in a symmetric way with respect to E_F. The symmetry axis of the energy distribution, i.e., the energy $\epsilon = E_\mathrm{F}$ at which the occupation probability amounts to 0.5, is denoted as the *Fermi energy* of the system. The Fermi-Dirac distribution reads as

$$f(\epsilon; T) = \frac{1}{e^{(\epsilon - E_\mathrm{F}(T))/k_\mathrm{B}T} + 1} \quad , \tag{2.1}$$

where k_B denotes Boltzmann's constant. It is depicted in Fig. 2.1 for several temperatures.

So far, the work function Φ of a metal can be regarded as the difference in energy between the *Fermi energy* E_F and the electrostatic energy of an electron in the vacuum near the metal surface. If the surface dimensions are finite, this value differs from the energy costs to remove an electron from the metal surface to a vacuum region *far* away from the surface. E_F takes a common value all over the metal. While the vacuum level at infinite distance from the surface is a constant too, it is influenced by the surface in its vicinity.

Due to the pronounced asymmetry at a crystal surface, i.e., the sudden end of crystalline repetition of atoms, electron density tails out into the vacuum region. The spilling out electron density corresponds to a lack of electrons inside of the metal, forming a *surface dipole layer* (Fig. 2.2). As described in more detail in the next section, an infinitely extended

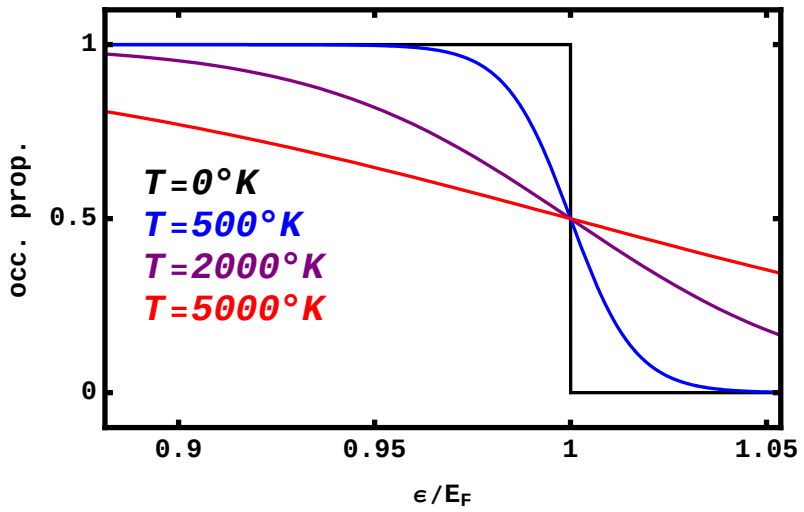

Figure 2.1: Fermi-Dirac statistics for several temperatures. E_F is defined as the energy with an occupation propability of 0.5.

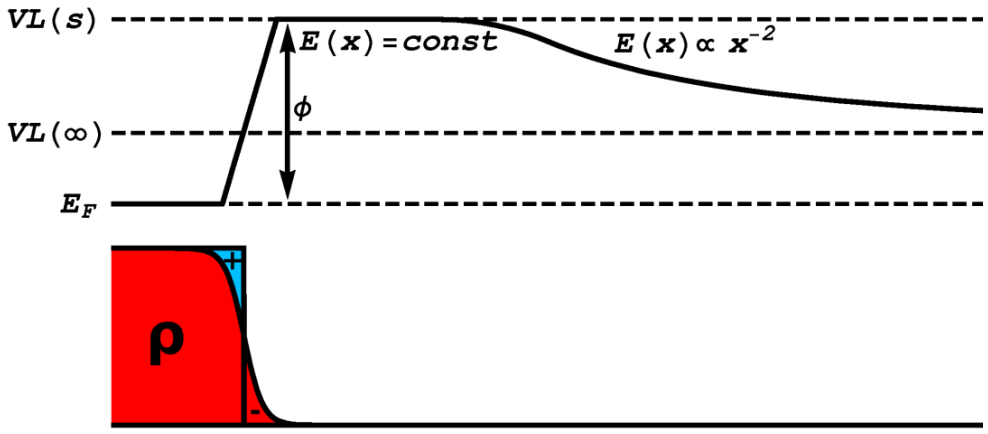

Figure 2.2: The electron cloud reaches out of the metal surface into the vacuum, giving rise to a surface dipole layer with the positive pole inside of the metal (bottom). Its impact on the electron potential energy implies an increase of the work function Φ. Starting from the vacuum level energy at surface VL (s), the energy decreases to a constant value VL (∞) far from a finite surface (top). The figure is reproduced from Ref. [1].

dipole layer causes a step in the electron potential energy. In contrast, the influence of a point dipole on the energy is proportional to x^{-2}. Since experimentally observed surfaces are of finite extension, a surface dipole layer appears as approximately infinite at small distances from the surface, and as a point dipole at large distances. The schematic shape of the resulting energy curve can be seen in the upper part of Fig. 2.2.

For different crystalline surfaces, different dipole layers arise. In addition to the electron cloud at the surface, for example also surface reconstructions and self-assembled monolayers (SAMs) adsorbed on the surface constitute such dipole layers. They affect the electrostatic potential and therefore the position of the vacuum level near the surface.

2.2 The effect of dipole layers on the electrostatic energy

The simplest and most lucid way to understand how an infinite[a] dipole layer affects the potential energy E of an electron is to invoke a plate capacitor as model for dipole layers [25]. The following paragraph about the electrostatics at a plate capacitor can be looked up in theoretical physics textbooks, e.g. Ref. [26].

The relation between the electrostatic potential Φ_{el} and the electrostatic field vector $\mathbf{E}$ is given by

$$\nabla\Phi_{\mathrm{el}} = -\mathbf{E} \quad . \tag{2.2}$$

For two plates at distance d, carrying an area charge density of Q/A, the relation $|\mathbf{E}| = Q/A\epsilon_0$ is valid. Here, ϵ_0 denotes the vacuum permittivity. Q/A may as well be expressed as the dipole moment μ per volume V, μ/V, with $\mu = Qd$. Eqn. (2.2) is solved by integration from the first ($z = 0$) to the second ($z = d$) plate of the capacitor (the plates being located along the z-axis). This way one obtains the change in the electrostatic potential $\Delta\Phi_{\mathrm{el}}$ between the plates:

$$\Delta\Phi_{\mathrm{el}} = \int_0^d \nabla\Phi_{\mathrm{el}}\, dz = \int_0^d -\frac{1}{\epsilon_0}\frac{\mu}{V}\, dz = -\frac{d}{\epsilon_0}\frac{\mu}{V} = -\frac{1}{\epsilon_0}\frac{\mu}{A} \quad . \tag{2.3}$$

$\Delta\Phi_{\mathrm{el}}$, and therefore the potential energy $E = -e\Delta\Phi_{\mathrm{el}}$ (with e being the (positive) elementary charge) grows linearly between the plates, resulting in a step of linear shape in the energy curve as depicted in Figs. 2.2 & 2.3. Therefore, an infinite layer of dipoles divides space into two inequivalent regions. The potential energy of a charge being located to the "left" of the layer differs from the energy the charge would have to its "right". Such a plate-capacitor like agglomeration of dipole moments may as well be generated by a SAM of dipolar molecules. However, the SAMs considered here do not show one single dipole moment across the long axis of the molecule, but dipoles at the left and right "ends" of the rod-like molecules (see Sec. 2.3).

2.2.1 Angle dependence $\Delta\Phi_{\mathrm{el}}(\mu(\varphi_{\mathrm{dip}}))$

In the derivation above, dipoles directed perpendicular towards the capacitor plates ($\varphi_{\mathrm{dip}} = 0$) are assumed. However, this assumption may not hold for the dipoles of SAMs on

[a] Finite and in other respects non-ideal dipole layers are studied in Ref. [24].

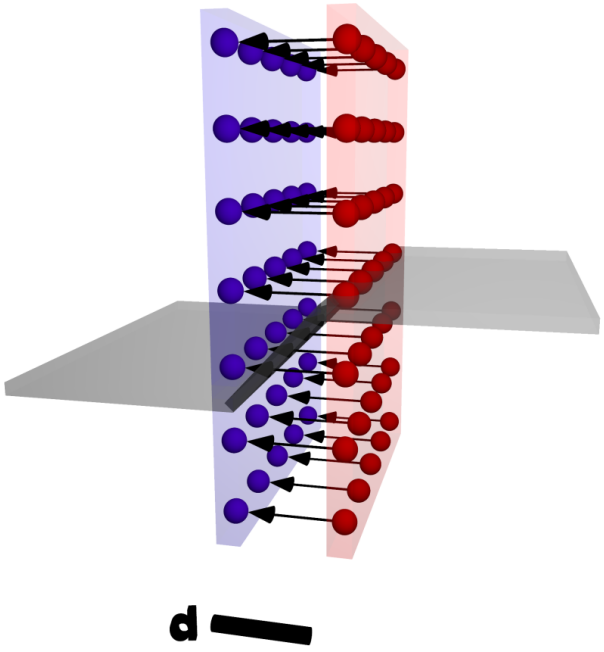

Figure 2.3: The plate capacitor as model for a dipole layer (red (blue) plate negatively (positively) charged). The potential energy of an electron crossing the capacitor is schematically depicted in gray color.

surfaces. Taking into account that the dipole moment μ is a vector, the effect of an inclination angle $\varphi_{\text{dip}} \neq 0$ of the dipoles can be determined. Only the projection of the dipole moment onto the axis that connects the plates (the z-axis), $\mu_z = \mu \cos(\varphi_{\text{dip}})$, affects $\Delta\Phi_{\text{el}}$. Hence, Eqn. (2.3) can be generalized:

$$\Delta\Phi_{\text{el}}(\varphi_{\text{dip}}) = -\frac{1}{\epsilon_0}\frac{\mu\cos(\varphi_{\text{dip}})}{A} = -\frac{1}{\epsilon_0}\frac{\mu_z}{A} \quad . \tag{2.4}$$

According to Eqn. (2.4), $\Delta\Phi_{\text{el}}(\varphi_{\text{dip}} \neq 0) < \Delta\Phi_{\text{el}}(\varphi_{\text{dip}} = 0)$.

2.3 SAMs as dipole layers

Literature: Refs. [16] & [21] & [25].

The SAMs introduced in this work have a common structure which is summarized in Fig. 2.4. They consist of three parts, being the docking group, the backbone and the head group (top of Fig. 2.4). A modified biphenyl (2P) or benzene (1P) molecule serves as backbone and provides the π-electron system. If adsorbed on a metal surface, the docking group is directed towards the surface and forms a bond, hence its name. Different head and docking group substituents provide handles to adjust the net dipole moment of the molecules. This goal is reached by exploiting the electron accepting or donating nature of the substituents. In total, the three different docking groups

- thiol (HS-), moderate donor
- pyridine (Pyr-), moderate acceptor
- isocyanide (CN-), strong acceptor

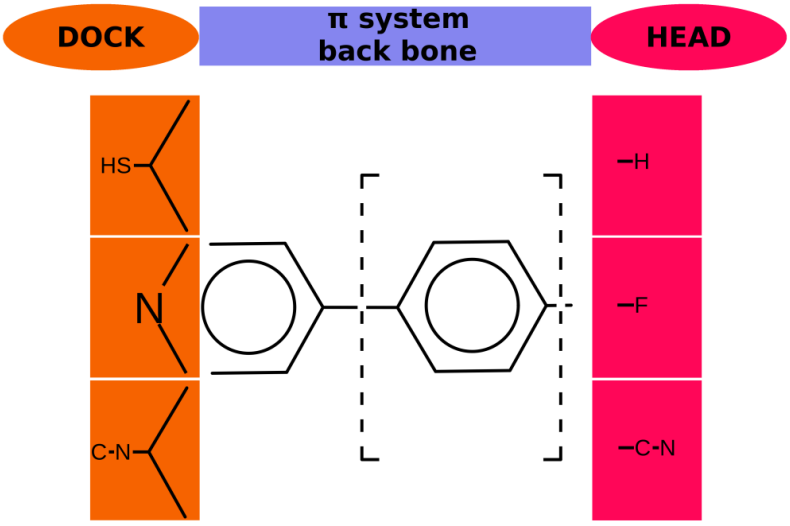

Figure 2.4: Schematic summary of the studied SAMs.

and the four head groups

- hydrogen (-H), unsubstituted
- fluorine (-F), moderate acceptor
- cyano (-CN), strong acceptor
- amino (-NH_2), strong donor

were used. It is convenient to use the naming convention *docking-group*|*number-of-rings*P|*head-group* to denote SAMs. The intrinsic dipole moment of those molecules can be independently controlled by the docking and the head group. Upon adsorption on a metal surface, different bond dipoles (see Sec. 2.4.1) arise for the different docking groups. While the HS-bond is *replaced* by a bond between sulfur and metal in case of the thiol docking group, a bond to the metal is *formed* in case of the other two docking groups.

If the net dipole moment of the self-assembled molecules is nonzero, the value of the electron potential energy at the left side of the SAM differs from its value at the right side for an infinitely extended monolayer. In other words, a left-side and a right-side vacuum level energy $\mathrm{VL}_{\mathrm{left}}$ and $\mathrm{VL}_{\mathrm{right}}$ can be defined. This effect is depicted in Fig. 2.5. It shows the electron potential energy across a quite polar SAM, averaged over the x, y-plane. This plane corresponds to the plane formed by the SAM. Pyr|2P|CN was chosen as SAM (see bottom part of the figure[b]). The left-side and right-side vacuum levels are denoted in the plot. Due to the non-zero net dipole moment of the molecules, $\mathrm{VL}_{\mathrm{right}} \neq \mathrm{VL}_{\mathrm{left}}$. Since this energetic difference is established within the thickness of a molecular monolayer, it is further on denoted as a step. In the following, such steps in the energy due to intrinsic dipole moments of SAMs are referred to as ΔE_{vac}.

As a consequence of the electrostatic properties of such a monolayer, the energy necessary to remove an electron from the layer (ionization potential (IP)) and the energy that is gained by attaching an electron to the layer (electron affinity (EA)) become directional

[b] 3D-visualizations of the various systems were generated using the XCrysDen program [27].

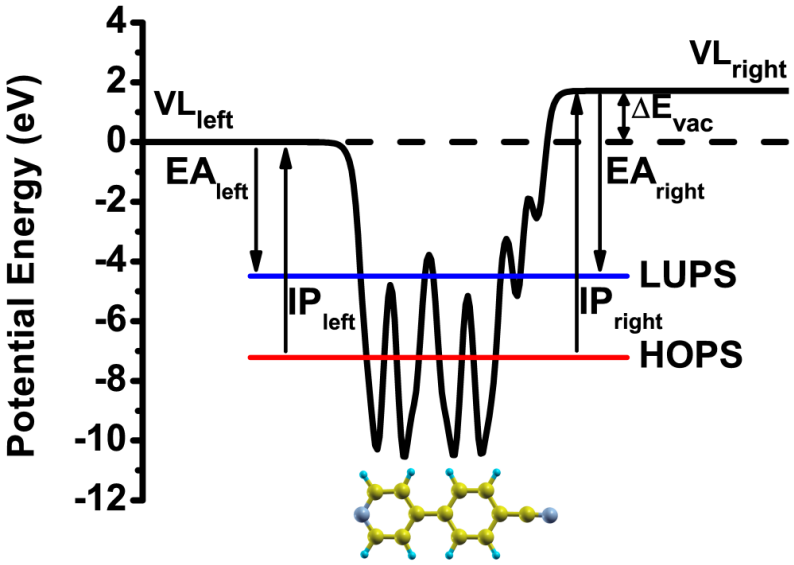

Figure 2.5: Electron electrostatic energy across a SAM, averaged over the plane corresponding to the plane formed by the SAM. Left and right side vacuum level energies VL_{left} and VL_{right} are denoted. The step in the electron potential energy caused by the monolayer (ΔE_{vac}) is illustrated. Left- and right-hand IP and EA are shown, too.

properties. The IP is approximated by the difference between the potential energy of an electron at vacuum level and the energy of the highest occupied states in the molecular layer, and the electron affinity (EA) by the difference between the potential energy of an electron at vacuum level and the energy of the lowest unoccupied states in the molecular layer [18]; they are plotted in Fig. 2.5 as well. A characteristic difference between semiconductors and metals is that for semiconductors the energy of the highest occupied states and the lowest unoccupied states, and therefore also IP and EA, differ significantly (at 0 K). This is described in the next section in more detail.

2.3.1 The density of states (DOS) of organic semiconductors (OSCs)

In contrast to metals, semiconductors show a *band gap* in the density of states (DOS). "Band gap" denotes the energy range between the highest occupied and the lowest unoccupied electronic states. Usually one denotes the highest occupied molecular orbital of a molecule as HOMO and the lowest unoccupied molecular orbital as LUMO. Quite ambiguously, this convention is frequently used for the corresponding states in an OSC bulk material too, where, physically more exact, the discrete molecular orbitals split up and form the DOS of the OSC. The resulting peaks in the DOS of SAMs and OSCs are in the following, more generally, denoted as highest occupied π-states (HOPS) and lowest unoccupied π-states (LUPS) [21].[c] For comparison, Fig 2.6 shows the DOS of a gold crystal

[c] Originally, the authors of Ref. [21] introduced this nomenclature for a different reason. Upon adsorption of a SAM on a metal surface, the corresponding peaks in the DOS can not unambiguously be associated

around E_F, an isolated Pyr|2P|CN molecule and a densely packed Pyr|2P|CN SAM around E_{HOMO} and E_{HOPS}, respectively. The discrete molecular orbitals (Fig 2.6b) are broadened in the DOS of the SAM (Fig 2.6c).

2.4 Interfaces

2.4.1 Metal|SAM interfaces

Literature: Refs. [21] & [25] & [18].

The previously introduced naming convention is slightly modified to denote extended systems in which a SAM is brought in contact with a metal by adding the component "*metal*" to its left: *metal*|*docking-group*|*number-of-rings*P|*head-group*. SAM and metal interact upon contact, meaning that the charges at the interface rearrange. Those charge rearrangements $\Delta\rho$ establish additional dipole layers at the interface. The consequence of the sum of all kinds of interactions that occur at such an interface on the electron potential energy are further on denoted as the *bond dipole* (BD). $\Delta\rho$ is a function of the three spatial variables. It is often integrated over the x, y-plane, which corresponds to the plane formed by the SAM.[d] The resulting function of the z-coordinate, $\Delta\rho(z)$ (unit: $-e/\text{Å}$), can then be shown in a 1D plot. The upper part of Fig. 2.7 shows such rearrangements for the adsorption of a Pyr|2P|CN SAM on an Au(111) surface. Note, that positive values stand for electron density accumulation. Hence, red areas indicate electron density accumulation and blue areas electron density depletion. By solving Poisson's equation for $\Delta\rho$ one obtains the effect of the charge rearrangements on the electron potential energy E:

$$\frac{d^2\Phi_{el}}{dz^2} = -\frac{\Delta\rho(z)}{\epsilon_0} \quad \Rightarrow \quad E = -e\Delta\Phi_{el} \quad , \tag{2.5}$$

with molecular orbitals anymore. It is therefore more adequate to refer to them with different names.
[d] See Chapter 4 for more details.

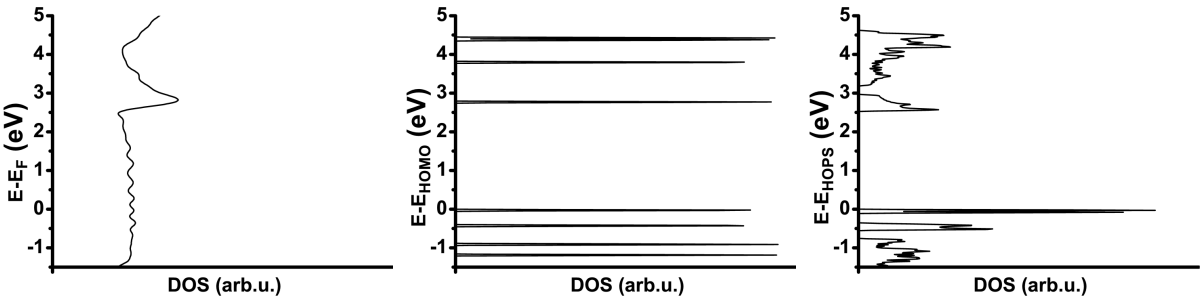

(a) (b) (c)

Figure 2.6: Comparison of the DOS of a gold crystal (a), the isolated molecule Pyr|2P|CN (b) and a densely packed SAM formed by Pyr|2P|CN molecules (c). (b) and (c) differ from (a) in the band gap, and (c) from (b) in the broadening of the peaks due to the splitting up of the molecular orbitals.

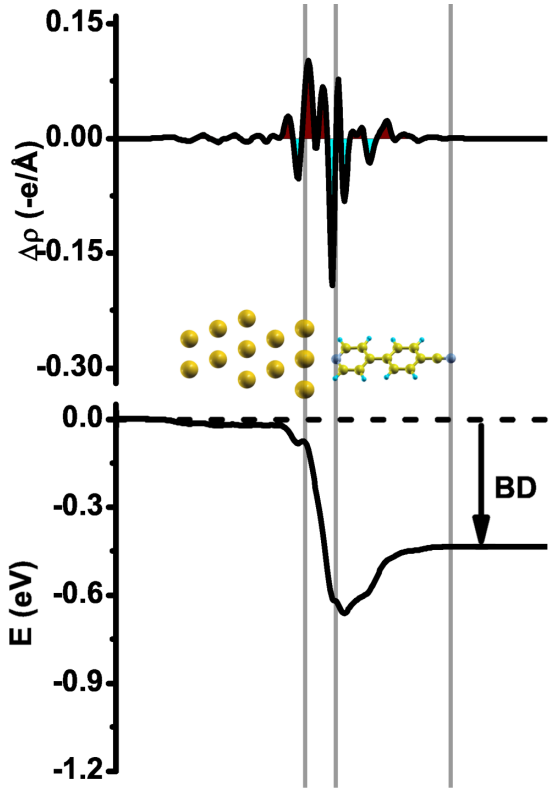

Figure 2.7: Plane integrated charge rearrangements $\Delta\rho(z)$ upon adsorption of a Pyr|2P|CN SAM on a Au(111) surface (upper panel), their effect on the electron potential energy E and the bond dipole (BD) (lower panel). Red areas indicate electron density accumulation and blue areas electron density depletion.

depicted in the lower panel of Fig. 2.7. The net effect of $\Delta\rho$ on E is referred to as the bond dipole (BD). BD and ΔE_{vac} together modify the metal work function:

$$\Delta\Phi_{\text{SAM}} = \Delta E_{\text{vac}} + \text{BD} \quad . \tag{2.6}$$

The BD may support or counteract ΔE_{vac}, depending on the actual interface. In the shown example, the negative BD (compare Fig. 2.7) counteracts the positive ΔE_{vac} (compare Fig. 2.5). Fig. 2.8 shows the plane averaged electrostatic potential before and after the adsorption process. It additionally shows the metal Fermi level and work function, HOPS and LUPS and the corresponding left- and right-hand IP and EA of the isolated (left) and contacted (right) SAM. Upon contact, the work function is modified to be

$$\Phi_{\text{mod}} = \Phi + \Delta E_{\text{vac}} + \text{BD} \quad . \tag{2.7}$$

The energy differences $\Delta E^{\text{SAM}}_{\text{HOPS}} := E^{\text{SAM}}_{\text{HOPS}} - E_{\text{F}}$ and $\Delta E^{\text{SAM}}_{\text{LUPS}} := E^{\text{SAM}}_{\text{LUPS}} - E_{\text{F}}$ differ somewhat from the intuitive (compare Fig. 2.8) relationships $\Delta E^{\text{SAM}}_{\text{HOPS}} = \Phi_{\text{Au(111)}} - \text{IP}_{\text{left}} + \text{BD}$ and $\Delta E^{\text{SAM}}_{\text{LUPS}} = \Phi_{\text{Au(111)}} - \text{EA}_{\text{left}} + \text{BD}$. The electronic structure of the SAM is slightly disturbed by the bond formation. This effect is described by the terms $E^{\text{HOPS}}_{\text{corr}}$ and $E^{\text{LUPS}}_{\text{corr}}$. Those correction energies can be quantified as the difference between IP_{right} of the isolated SAM and the corresponding energetic distance in the contacted system, IP_{SAM} (see Fig. 2.8). Consequently, $\Delta E^{\text{SAM}}_{\text{HOPS}}$ and $\Delta E^{\text{SAM}}_{\text{LUPS}}$ are determined to be

$$\begin{aligned} \Delta E^{\text{SAM}}_{\text{HOPS}} &= \Phi_{\text{Au(111)}} - \text{IP}_{\text{left}} + \text{BD} + E^{\text{HOPS}}_{\text{corr}} \quad , \\ \Delta E^{\text{SAM}}_{\text{LUPS}} &= \Phi_{\text{Au(111)}} - \text{EA}_{\text{left}} + \text{BD} + E^{\text{LUPS}}_{\text{corr}} \quad . \end{aligned} \tag{2.8}$$

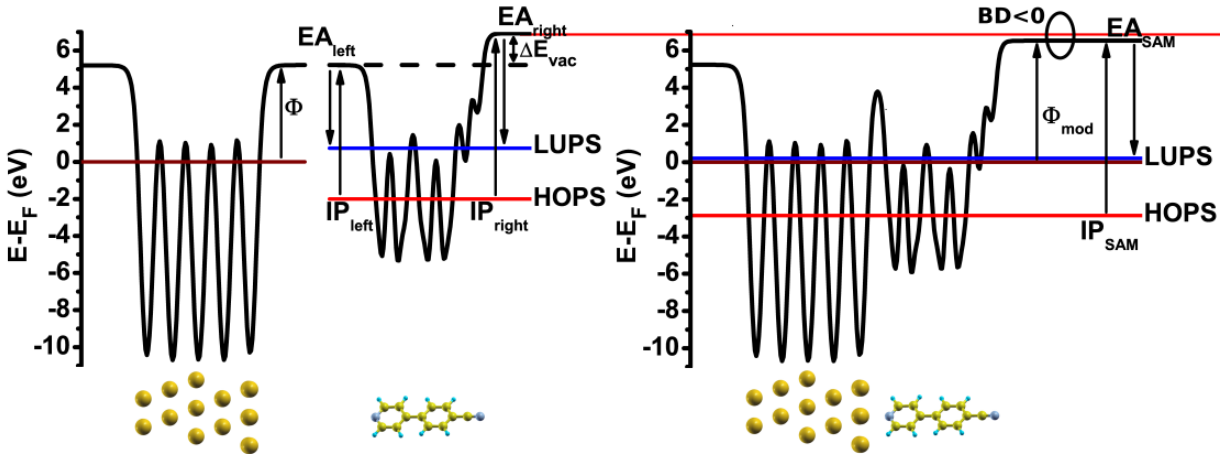

Figure 2.8: Plane averaged electron potential energy at an Au(111) surface and a Pyr|2P|CN SAM *before* (left panel) and *after* (right panel) adsorption of the SAM. Additionally, HOPS and LUPS and the corresponding left- and right-hand side IPs and EAs, ΔE_{vac} and the consequence of the BD are shown. The metal Fermi level is drawn as black line; the energy axis is shifted by E_{F} in both figures.

2.4.2 Metal|SAM||OSC interfaces

The systems are now additionally extended to include the last component of the investigated three component systems, an OSC. The notation then goes like *metal*|*docking-group*|*number-of-rings*P|*head-group*||*OSC*. Here, "||" hints to the weak, van der Waals dominated interaction usually found at organic interfaces [20]. To keep the computational costs moderate, the OSC is represented by a single monolayer of semiconducting material in the present calculations. The chosen material is 2P, which has no intrinsic dipole moment and therefore an almost vanishing ΔE_{vac}.[e] See Sec. 5.1 for details about the 2P layer.

Usually, no interfacial dipole layers are formed at organic/organic interfaces due to the weak van der Waals interaction that governs such interfaces. Hence, the vacuum levels of the isolated systems are often found to align [20, 4]. Vacuum level alignment is often referred to as the Schottky-Mott limit.

Highly interesting quantities at interfaces are the *injection barriers*. They are the energy barriers charge carriers have to overcome in order to cross the interface. In the following, those quantities are estimated by the differences between the metal Fermi level and the peak maxima of the frontier energy levels of the 2P: the hole injection barrier (HIB) is estimated by the energetic distance

$$\Delta E^{\text{2P}}_{\text{HOPS}} := (E_{\text{F}} - E^{\text{2P}}_{\text{HOPS}}) \tag{2.9}$$

[e] Actually, a small ΔE_{vac} arises across the 2P monolayer. It is attributed to asymmetries in the unit cell and to computational issues in the determination of the compensating dipole moment; see Sec. 5.1 for details.

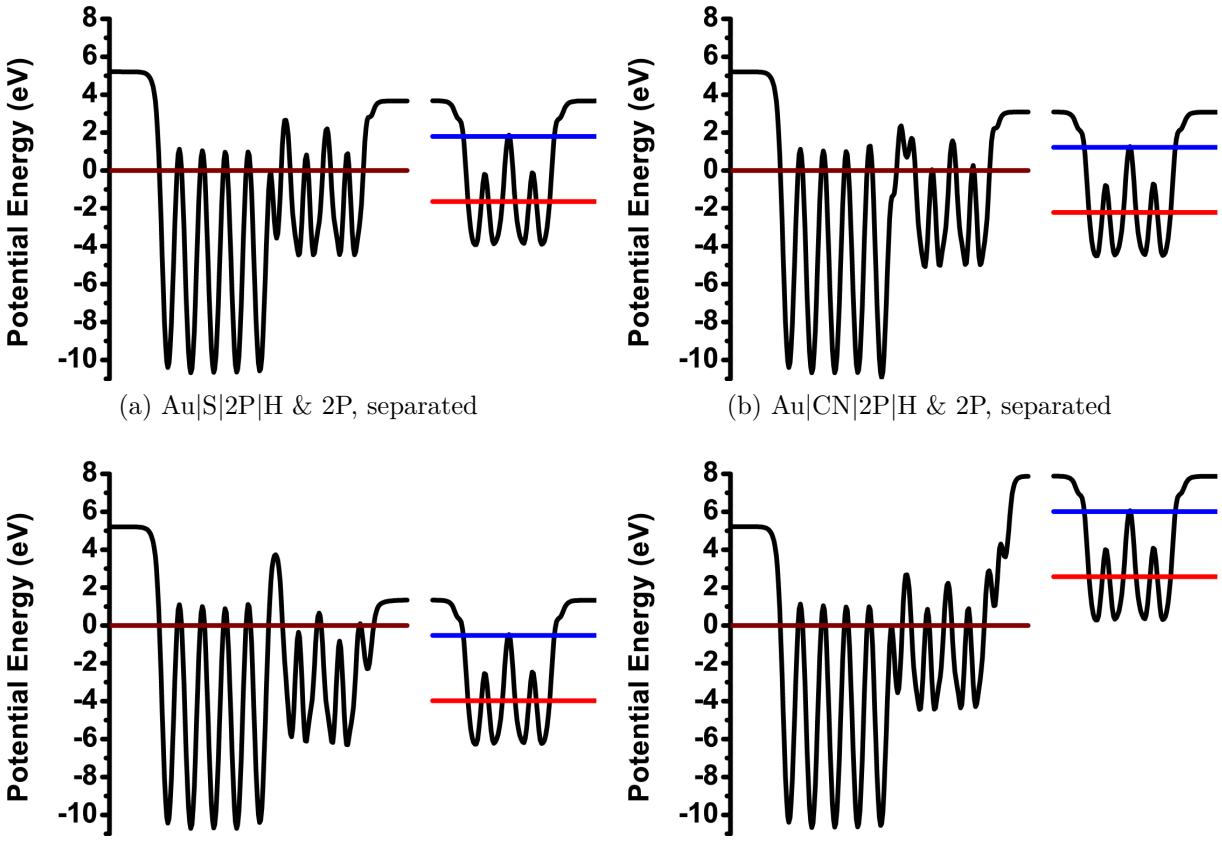

(a) Au|S|2P|H & 2P, separated

(b) Au|CN|2P|H & 2P, separated

(c) Au|Pyr|2P|NH_2 & 2P, separated

(d) Au|S|2P|CN & 2P, separated

Figure 2.9: Plane-averaged electrostatic energy curves for different Au(111) surface modifications and a monolayer of 2P, isolated from the former. The dark red, red and blue horizontal lines mark the Fermi level of the metal and HOPS and LUPS of 2P, respectively.

and

$$\Delta E^{\mathrm{2P}}_{\mathrm{LUPS}} := (E^{\mathrm{2P}}_{\mathrm{LUPS}} - E_{\mathrm{F}}) \tag{2.10}$$

is regarded as a measure for the electron injection barrier (EIB). Fig. 2.9 shows the potential energy curves and relevant energy levels of an Au(111) surface covered by different SAMs. Additionally, each diagram contains the same information for a 2P layer isolated from the surface. Assuming for the moment that the vacuum levels of the separated systems align upon contact, the capability of the SAM to modify the carrier injection barriers becomes apparent. A comparison of panels (a) & (b) shows, that the exchange of the SAM interlayer would increase the HIB under this assumption of a common vacuum level. Accordingly, the EIB would decrease (the 2P LUPS would approach E_{F}). Such a control of the injection barriers is a motivation for the use of SAMs in organic electronics.

The first main topic of this work is to test whether this direct control of the injection barriers is indeed realized for systems which show an energetic configuration comparable to those in Fig. 2.9a&b.

More interesting configurations can be seen in panels (c) and (d). In those systems, the SAM-induced work function modification would cause the LUPS (HOPS) of the 2P layer to

lie below (above) the metal Fermi level. While the assumption of vacuum level alignment appears to be reasonable in the former cases, this Schottky-Mott limit is not going to be thermodynamically stable here. Since all states in a system below E_F are occupied and none above E_F[f], an unfilled (filled) LUPS (HOPS) below (above) E_F is not expected to be realized. The avoidance of such configurations is commonly referred to as *Fermi level pinning*. Pinning can be observed experimentally at metal/organic interfaces [4, 5] as well as at organic/organic heterojunctions [6]. The second main topic of this diploma thesis is to analyze and understand junctions of the latter kind.

The analysis of such systems conceptually follows the analysis of the metal|SAM systems. One studies in which way the charges in the system rearrange upon addition of the OSC. Such charge rearrangements may effect the potential energy (compare Eqn. (2.5)). In complete analogy to Eqn. (2.6) one can write:

$$\Delta\Phi_{\mathrm{OSC}} = \Delta E_{\mathrm{vac}} + \mathrm{BD} \quad . \tag{2.11}$$

However, since no covalent bonds are formed at the organic/organic interface, the name bond dipole appears to be inappropriate here. Instead, this quantity is merely referred to as the *interface dipole (ID)*. Additionally, the net dipole moment vanishes in case of a monolayer of 2P. This causes ΔE_{vac} to be zero as well. Hence, one ends up with

$$\Delta\Phi_{\mathrm{2P}} = \mathrm{ID} \quad . \tag{2.12}$$

$\Delta\Phi_{\mathrm{2P}} = 0$ corresponds to vacuum level alignment and $\Delta\Phi_{\mathrm{2P}} \neq 0$ describes the deviation from vacuum level alignment. The measures for the injection barriers $\Delta E^{\mathrm{2P}}_{\mathrm{HOPS}}$ and $\Delta E^{\mathrm{2P}}_{\mathrm{LUPS}}$ are given by

$$\begin{aligned} \Delta E^{\mathrm{2P}}_{\mathrm{HOPS}} &= -(\Phi_{\mathrm{Au(111)}} + \Delta\Phi_{\mathrm{SAM}} + \Delta\Phi_{\mathrm{2P}} - \mathrm{IP}_{\mathrm{2P,c}}) \quad , \\ \Delta E^{\mathrm{2P}}_{\mathrm{LUPS}} &= \Phi_{\mathrm{Au(111)}} + \Delta\Phi_{\mathrm{SAM}} + \Delta\Phi_{\mathrm{2P}} - \mathrm{EA}_{\mathrm{2P,c}} \quad . \end{aligned} \tag{2.13}$$

$\mathrm{IP}_{\mathrm{2P,c}}$ and $\mathrm{EA}_{\mathrm{2P,c}}$ stand for the IP and EA of this prototypical organic semiconductor. The indices "c" are used to account for changes of those quantities that may arise upon ***c***ontact with the metal|SAM system. They are defined in complete analogy to $\mathrm{IP}_{\mathrm{SAM}}$ and $\mathrm{EA}_{\mathrm{SAM}}$ in Fig. 2.8.

Before presenting the energetics of the used SAM interlayers in Chapter 4 and the analysis of the full three component systems later on in Chapter 5, the methodology for the calculations is presented in the following chapter.

[f] This is true at 0 K only (Fig. 2.1). However, the performed calculations are zero temperature calculations.

3 Methodology

3.1 Periodic boundary conditions

To simulate infinitely extended surfaces, *band structure calculations* are employed. In a band structure calculation, a unit cell is defined that periodically repeats in the three spatial dimensions. Quantum mechanical calculations are then performed on the resulting infinite system. Repetition in only two dimensions would of course be sufficient to model surfaces. The third dimension is handled by inserting a vacuum gap above the surface to prevent interaction between the adjacent surfaces. Tests in our group have proven a vacuum gap of about 20 Ångström to be sufficient for this purpose. The described technique is commonly referred to as the *repeated slab approach*.

Representative unit cells are shown in Fig 3.1 from different perspectives. Fig 3.1a shows the repetition in all directions. The unit cells of interest are highly asymmetric in z-direction. To match the electrostatic potentials at the bottom and at the top region of the unit cell, a dipole layer is inserted in the middle of the vacuum. It compensates the work function modification induced by the SAM.

3.2 Structure of the unit cells

As visible in Fig 3.1, the metal bulk is approximated by five layers of gold atoms. Supported by experimental data [28], the SAMs are structured in a so-called herringbone pattern. In this structure, the molecules are arranged in a zigzag-like fashion. Two inequivalent (almost) upright standing molecules, enclosing a certain angle, define a $p(3 \times \sqrt{3})$ surface superstructure[a] as depicted in Fig 3.1b. "p" indicates that a ***p***rimitive unit cell is used. Multiplied with the length of the translation vectors $\mathbf{a}_s$ and $\mathbf{b}_s$, which define the surface unit cell of the ***s***ubstrate, the numbers give the dimensions of the surface superstructure; it is rectangular in this case. In our group, we use a gold lattice constant of 4.175 Å. It was found to be the energetically most favorable gold bulk lattice constant according to calculations [18]. For the Au(111) surface, this implies $|\mathbf{a}_s| = |\mathbf{b}_s| \approx 2.95$ Å. Hence, the resulting surface superstructure dimensions are 8.86 Å × 5.11 Å. Since the substrate surface unit cell will not be mentioned anymore, this superstructure will further on be denoted as the surface unit cell with lattice vectors $\mathbf{a}$ and $\mathbf{b}$ for reasons of simplicity.

A monolayer of 2P is placed on top of the SAM. The 2P bulk structure is a herringbone structure too, but its unit cell differs from the metal|SAM surface unit cell. Hence, it had to be assumed that the biphenyl monolayer adopts the structure of the SAM, i.e., the 2P bulk lattice constants were modified accordingly. For additional details about this

[a] For a more detailed explanation of *Wood's Notation*, see e.g. Ref. [29].

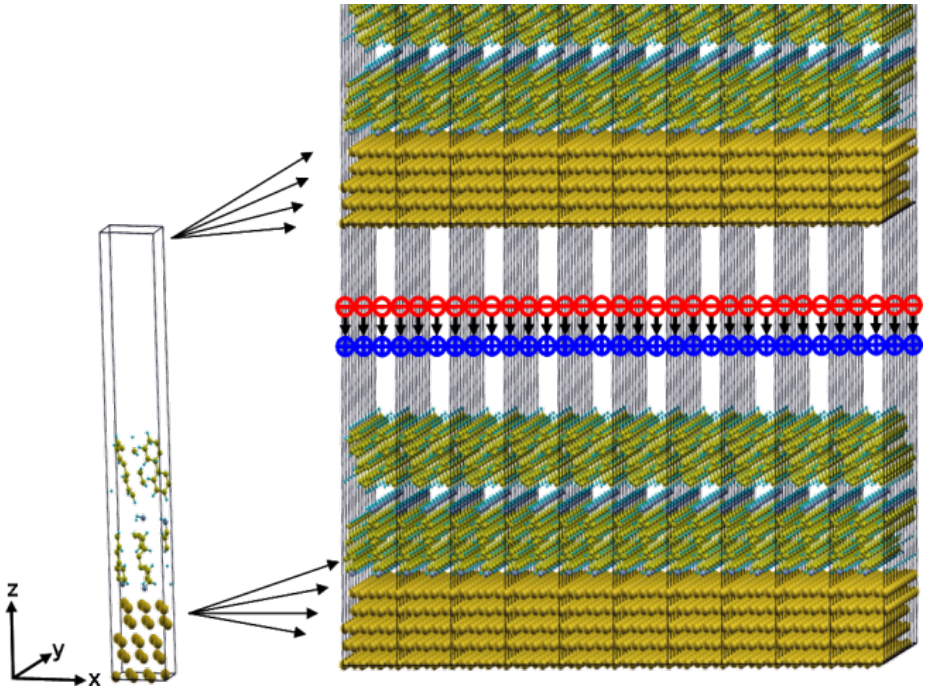

(a)

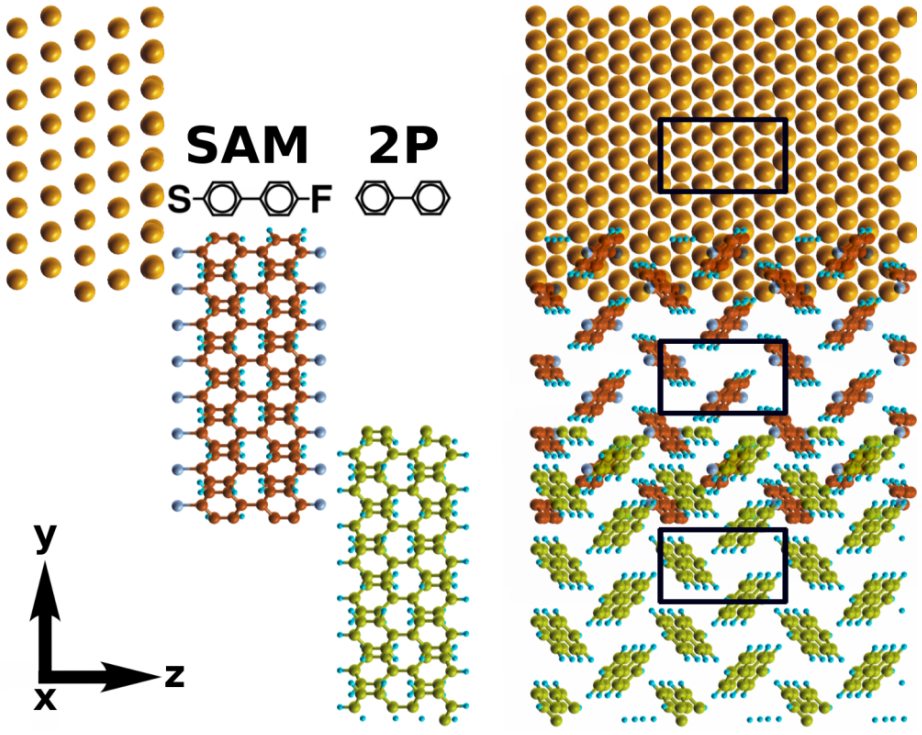

(b)

Figure 3.1: Representative unit cells from different perspectives. (a): The repetition of the unit cell in the x, y-plane models the surface. Insertion of a vacuum gap in z-direction and a dipole layer in its middle prevents interaction between the slabs. (b): Side and top view of a $p(3 \times \sqrt{3})$ surface unit cell to illustrate the herringbone structured SAM and 2P, shifted for the sake of clarity. The black rectangles mark the unit cell.

approach, see Sec. 5.1. The height of the three components amounts to approximately 30 Å, so that in any case a unit cell height of 60 Å is sufficient.

Geometry relaxation calculations. To find energetically favorable positions of the atoms of the system, *geometry relaxation calculations* were performed. Different approaches exist to perform such calculations. A somewhat more detailed account of the used technique is given in Sec. 6.2.2.

When the geometry of a metal|SAM system was relaxed, the coordinates of the lower three metal layers were kept fixed to represent the bulk. The upper two layers - representing the interface to the SAM - were free to move.

The isolated biphenyl monolayer in the adjusted unit cell was optimized too. The z-coordinates of the lowermost hydrogen atoms of the layer were kept fixed to guarantee evenness.

The complete metal|SAM||OSC systems were not relaxed due to reasons explained in the next section.

All geometry relaxations were stopped as soon as the maximum force on an atom fell below 0.01 eV/Å.

3.3 Density Functional Theory (DFT)

Literature: Refs. [30], [31], [32] & [33].

The term Density Functional Theory refers to the approach to find the ground state of a quantum mechanical system through functionals which only depend on the electron density $n(\mathbf{r})$, instead of solving the Schrödinger equation of the many particle problem. Since $n(\mathbf{r})$ is a function of only three variables, while the many particle wave function $\Psi(\mathbf{x}_1, \mathbf{x}_2, \ldots, \mathbf{x}_N)$ depends on $3N$ spatial variables r_i^α and N spin variables s_i for N electrons ($\mathbf{x}_i = \{r_i^\alpha; s_i\}$; $\alpha = 1, 2, 3$), this approach implies a drastic reduction of complexity in the description.

In principle, this approach is legitimated by the proven first theorem of Hohenberg and Kohn [34] which states, that such a functional indeed exists. Though, no expression for it could be found so far. According to the second theorem of Hohenberg-Kohn the ground state electron density and total energy are solutions of a variational problem, i.e., the exact ground state electron density minimizes the functional for the total energy. This theorem is proven as well [34].

An example for such a functional is the expression for the total energy according to the Thomas-Fermi model:

$$E[n(\mathbf{r})] = \frac{3}{10}(2\pi^2)^{2/3} \int n^{5/3}(\mathbf{r}) d^3r - \sum_{a=1}^{M} Z_a \int \frac{n(\mathbf{r})}{|\mathbf{r} - \mathbf{R}_a|} d^3r + \frac{1}{2} \iint \frac{n(\mathbf{r}) n(\mathbf{r}')}{|\mathbf{r} - \mathbf{r}'|} d^3r d^3r' \quad . \tag{3.1}$$

Here, $\mathbf{R}_a$ and Z_a denote the coordinates and the charge of the a-th nucleus of a system of M nuclei. The first term describes the kinetic energy of the electrons, while the second and the third term describe the Coulomb interaction of the electrons with the nuclei and with each other.

Actually, the Thomas-Fermi model (1927) predates the theorems of Hohenberg and Kohn (1964), which theoretically justify the DFT approach. Early attempts to find the desired functional, such as Eqn. (3.1), led to quite unsatisfying results. Such a description is purely electrostatic and therefore fails to account for exchange and correlation between the electrons. In 1965, Kohn and Sham suggested to replace the description of the N electron system with the description of a fictitious system of non-interacting particles with single particle wave functions φ_i. The Kohn-Sham equations read as follows:

$$\left\{-\frac{1}{2}\nabla^2 + \sum_{a=1}^{M}\frac{Z_a}{|\mathbf{r}-\mathbf{R}_a|} + \int\frac{n_{\mathrm{KS}}(\mathbf{r}')}{|\mathbf{r}-\mathbf{r}'|}d^3r' + \frac{\delta E_{xc}[n_{\mathrm{KS}}(\mathbf{r})]}{\delta n_{\mathrm{KS}}(\mathbf{r})}\right\}\varphi_i(\mathbf{r},s) = \epsilon_i\varphi_i(\mathbf{r},s) \quad , \tag{3.2}$$

where ϵ_i is the eigenenergy of the i-th of N fictitious particles and $n_{\mathrm{KS}}(\mathbf{r})$ is their density. The famous e<u>x</u>change-<u>c</u>orrelation potential $\delta E_{xc}[n_{\mathrm{KS}}(\mathbf{r})]/\delta n_{\mathrm{KS}}(\mathbf{r})$ captures exchange and all correlations whatsoever between the electrons. Eqns. (3.2) do not describe a system directly as a function of $n_{\mathrm{KS}}(\mathbf{r})$, as, for example, Eqn. (3.1) does. However, the description is still in accordance with the density functional approach because of the relation

$$\sum_{i}^{N}|\varphi_i|^2 = n_{\mathrm{KS}}(\mathbf{r}) \quad . \tag{3.3}$$

The Kohn-Sham Hamiltonian lacks many particle operators and is, therefore, still more convenient than the original Schrödinger equation, although more complex than a direct description like Eqn. (3.1). However, it does not describe the real system one is interested in. Hence the question arises, how solving the Kohn-Sham equations can help to understand real world physics. The connection between the real and the "replacement" system is given by the fact that, as long as the correct xc-functional is used, the particle densities of the real and the artificial system coincide,

$$n_{\mathrm{KS}}(\mathbf{r}) \equiv n(\mathbf{r}) \quad . \tag{3.4}$$

As a consequence, also the total energies of the systems equal, as dictated by the first theorem of Hohenberg and Kohn. In contrast, no relation between the eigenstates φ_i and eigenenergies ϵ_i and the electronic states and energies can be derived theoretically. This renders them, in a strict sense, meaningless. Anyhow, there is an interesting and important exception: it can be proven, that the energy of the highest occupied state corresponds to the ionization potential (IP) or, in case of a metal, the work function [35, 36].

Unfortunately, the exact xc-term remains unknown in Kohn-Sham theory. Hohenberg and Kohn have proven its existence and universality, i.e., that it is independent of the described system. However, approximations have to be used at the present. The functional used in our group is called PW91 [37]. Like other state-of-the-art xc-functionals, it is *local*. A functional is said to be local, if its value $\delta E_{xc}[n_{\mathrm{KS}}(\mathbf{r})]/\delta n_{\mathrm{KS}}(\mathbf{r})$ at a point $\mathbf{r}$ depends only on the density $n_{\mathrm{KS}}(\mathbf{r})$ (and the gradient of the density $\nabla n_{\mathrm{KS}}(\mathbf{r})$ at the same coordinate). Hence, such functionals are not capable of describing *non-local* phenomena. Important non-local interactions are van der Waals forces. Efforts are being made to develop *non-local* functionals capable of describing such interactions [38, 39].

To sum up, Kohn-Sham orbitals may be interpreted with caution only [40, 41]. Given that a high quality approximation to the correct xc-functional is used, one can expect

reliable electron densities $n(\mathbf{r})$, IPs and, according to the first theorem of Hohenberg and Kohn, a good approximation to the total energy. Especially when looking at the band gap of a semiconductor one has to expect a significantly wrong value due to a wrong electron affinity (EA). Additionally, state-of-the-art *xc*-functionals do not properly account for van der Waals forces.

In the present work, *qualitative* effects at interfaces are investigated, and all arguments apply to the *relative* positions of energy levels. Errors in the absolute values of energy levels do not weaken the drawn conclusions, since the systems shall be regarded as model systems only. The inability to account for van der Waals forces is, unlike for the description of covalently bonded SAMs, a restriction when dealing with the SAM||OSC interface. Details on the modeling of this interface are given in Sec. 5.2.

Since the desired electron density $n(\mathbf{r})$ needs to be known already to construct the Kohn-Sham Hamiltonian, Eqns. (3.2) have to be solved in a self consistent fashion. In the VASP code [42], which was chosen as implementation of Kohn-Sham DFT, the self consistent cycles are in principle performed as follows [43]: a start density $n_{\text{in}}(\mathbf{r})$ is chosen to construct a Hamiltonian $\mathcal{H}$. Eqns. (3.2) are then solved iteratively to find wave functions of satisfying accuracy for the present $\mathcal{H}$. According to Eqn. (3.3), a new charge density $n_{\text{out}}(\mathbf{r})$ is obtained. Before this charge density is used as input for the next cycle, a charge density mixing [43] is applied for reasons of stability of the calculation:

$$n_{\text{in}}(\mathbf{r}) \quad \rightarrow \quad \mathcal{H} \quad \rightarrow \quad \varphi_i \quad \rightarrow \quad n_{\text{out}}(\mathbf{r}) \quad .$$

mixing

As soon as a certain total energy convergence criterion is fulfilled, the calculation stops. It is set to $\Delta E < 1.10^{-4}\,\text{eV}$ in the present calculations.

3.4 Convergence of the numerical calculations

VASP provides a set of parameters which regulate the accuracy of calculations. The chosen values of those parameters have to be carefully tested on their impact on the precision of the calculations. Besides the convergence criterion for the total energy of $\Delta E = 1 \cdot 10^{-4}\,\text{eV}$, the importance of two other parameters was tested in this work.

3.4.1 Cutoff energy and k-point grid

To construct the wave functions, VASP uses a plane wave basis set. The accuracy (and the speed!) of a calculation can be regulated by the specification of a *cutoff energy* E_{cut}. Only plane waves with kinetic energies smaller than E_{cut} are included in the basis set.[b] For every atomic species X, a certain value $E_{\text{cut,X}}$ is recommended by VASP. If various species are present in the unit cell, the highest of the recommended cutoff energies should be chosen.

[b] Plane wave basis sets in general converge very slowly with increasing E_{cut}. In VASP, the use of the projector augmented wave (PAW) method to describe valence-core electron interactions allows for quite low cutoff energies. For details, see Ref. [44].

Table 3.1: k-point grids used in the convergence tests. The inverse ratio between the lengths of the real space lattice vectors b and a is given by $1/(b/a) \approx 1.73$.

$k_x \times k_y$	k_y/k_x	$k_x \times k_y$
2×3	1.50	6
3×4	1.33	12
3×5	1.66	15
4×6	1.50	24
5×8	1.60	40
6×10	1.66	60
6×11	1.83	66
7×10	1.43	70
8×12	1.50	96
8×15	1.88	120
9×15	1.66	135
10×15	1.50	150
10×16	1.60	160
10×17	1.70	170
12×18	1.50	216

The second parameter is the k-point grid; it establishes the number and the positions of points in k-space at which numerical calculations in k-space are evaluated (the supporting points).[c] The finer the grid is, the more accurate the results are. Since space and reciprocal space are three dimensional, densities along three axis have to be chosen to define a certain grid. Additionally, shifts can be introduced to avoid symmetries. They lead to the computationally undesirable effect that two or more k-points are equivalent. In this case computation time would be lost, since every quantity evaluates to the same value at equivalent points.

If the surface unit cell is not square, the k-point density along the axes has to be chosen in a way that the grid fineness is approximately equal along the two dimensions. This assures comparable accuracy along both axes. This goal is reached by setting the ratio between the number of k-points along the $\mathbf{k}_y$- and $\mathbf{k}_x$-axes, k_y/k_x, approximately equal to the reciprocal value of the ratio between the unit cell vectors $\mathbf{b} = b\mathbf{e}_y$ and $\mathbf{a} = a\mathbf{e}_x$, $\frac{1}{b/a}$. In $\mathbf{k}_z$-direction, only a single point is used. This is sufficient for the present unit cells, (i) because of the great magnitude of the lattice vector $\mathbf{c}$ pointing in the z-direction and (ii) because it is not our intention to account for periodicity in this direction. This value remains unchanged in the following convergence tests and is therefore not explicitly mentioned. A ratio of $k_y/k_x = a/b \approx 8.86/5.11 \approx 1.73$ is approximately realized by the k-point value combinations listed in Tab. 3.1. The positions of those points in k-space are chosen according to the Monkhorst-Pack scheme [45]. Here, the points are distributed

[c] Instructive information is provided by two sessions of a VASP workshop: see http://cms.mpi.univie.ac.at/vasp-workshop/slides/k-points.pdf (Session 5) and http://cms.mpi.univie.ac.at/vasp-workshop/slides/accuracy.pdf (Session 10).

uniformly, according to

$$\mathbf{k} = \mathbf{k}_x \frac{n_1 + 1/2}{N_1} + \mathbf{k}_y \frac{n_2 + 1/2}{N_2} + \mathbf{k}_z \frac{n_3 + 1/2}{N_3} \quad , \quad n_i = 0, \ldots, N_i - 1 \quad , \tag{3.5}$$

where a k-point grid is commonly denoted as $N_1 \times N_2 \times N_3$.

The dependence of two important quantities on E_{cut} and the chosen k-point density is investigated: (i) the total free energy E_{tot} and (ii) the magnitude of the dipole moments μ_z placed in the vacuum region to guarantee periodicity of the electrostatic energy in z-direction. The latter quantity is highly interesting because it is closely related to the work function modification at the surface (Eqn. (2.3)). Therefore, the corresponding plot does not show μ_z itself, but its effect on the electron potential energy E. E_{tot} is especially important for the comparison of different SAM conformations, since a lower energy corresponds to a more favorable geometry than a higher energy.

In Fig. 3.2a, the total energy is plotted as a function of the number of k-points for three different cutoff energies. The chosen cutoff energies are $E_{\text{cut,C}} = 273.894\,\text{eV}$, $E_{\text{cut,S}} = 280.000\,\text{eV}$ and $1.3 \times E_{\text{cut,S}} = 364.000\,\text{eV}$. The recommended cutoff energy for sulfur $E_{\text{cut,S}}$ is the highest among the recommended values for the species used in the present work (*Au*, *S*, *C*, *H*, *N*, *F*). It can be seen that the total energy converges relatively fast, independent of the cutoff energy. However, it converges to different values! Hence, only energy *differences* converge fast. Also, one has to be aware of the fact, that only energies from calculations with the same cutoff energy can be compared. In our group, traditionally $E_{\text{cut}} = 273.894\,\text{eV}$ is used for all calculations, even if, e.g., sulfur atoms exist in the unit cell. This is reasonable, because it allows for a comparison of different calculations. A 5×8 k-point mesh (No. of k-points: 40) for the typical $p(3 \times \sqrt{3})$ SAM surface unit cell is traditionally used in our group (dashed line in the plots). As the convergence test shows, the total energy is not fully converged at this k-point density. For the sake of comparability with other calculations performed by our group and because of the reasonable tradeoff between speed and accuracy this choice provides, the same k-point grid is used in the computations of this work. The total energy values for the calculations denoted as "*cont1*" are obtained by restarting the previous calculations. This time, the output wave function of those calculations are taken as input wave functions instead of starting from scratch (by setting `ISTART = 1`, see Sec. 3.6). Consequently, the calculation rapidly converges. Calculations marked as "*cont2*" are performed the same way, except that the calculation is forced to continue for a few self consistent cycles beyond reached energy convergence (using the tag `NELMIN`, see Sec. 3.6). As expected, those procedures do not change the results, since the total energy has already converged; they are important in the next paragraph.

More interesting is the dependence of the step in the electron potential energy resulting from the dipole layer in the middle of the vacuum region. It is the key quantity for the calculation of the work function modification, and therefore its accuracy should be well known. This step is depicted in Fig. 3.2b for the cutoff energies mentioned above. Even for a grid as fine as 10×17, deviations of almost 0.1 eV are found for $E_{\text{cut,C}} = 273.894\,\text{eV}$. This is not primarily due to the cutoff energy, as can be seen in Fig. 3.2c. It shows the results obtained by reading in the energy-converged wave functions again and performing a

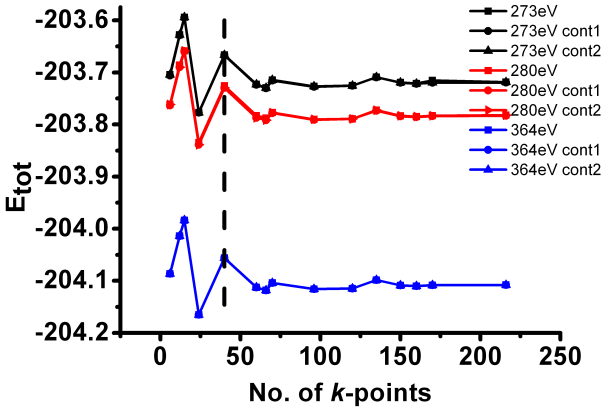

(a) Dependence of the total free energy on the chosen k-point mesh for three different cutoff energies. The calculations "*cont1*" and "*cont2*" yield the same results.

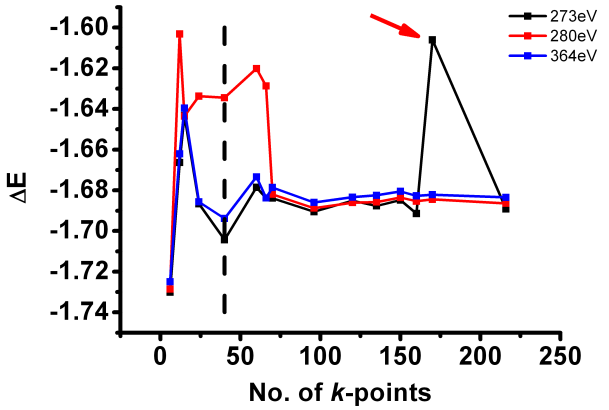

(b) Convergence of the step in the electrostatic energy due to the inserted dipole layer.

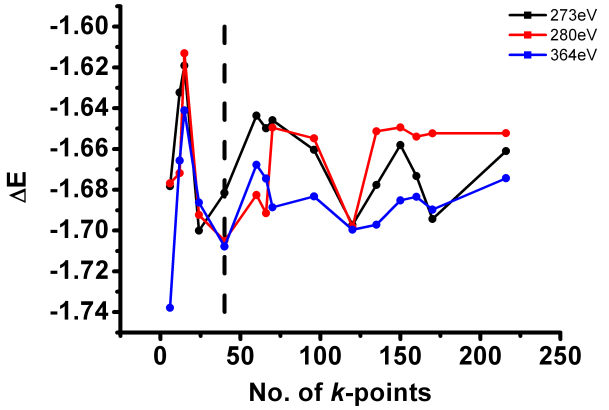

(c) Convergence of the step in the electrostatic energy when reading in the energy-converged wave functions ("*cont1*").

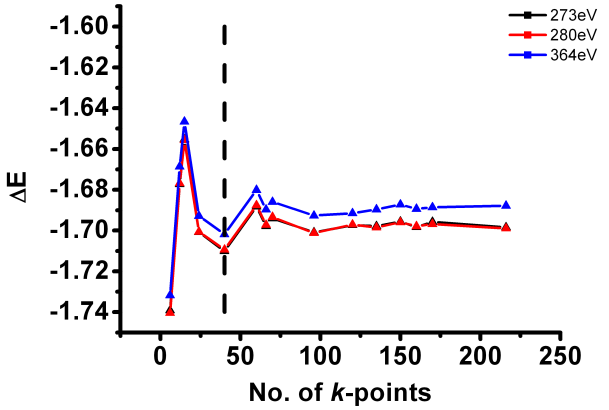

(d) Convergence of the step in the electrostatic energy when VASP is forced to continue the calculation for 5-10 cycles beyond energy convergence ("*cont2*").

(e) A $8.86 \times 5.11 \times 50$ Au|S|1P|H unit cell with three layers of gold was used in the convergence tests.

Figure 3.2: Results of the convergence tests performed for the unit cell depicted in (e). The black, dashed vertical lines mark the $5 \times 8 \times 1$ k-point grid which was chosen in the subsequent calculations. "*cont1*": energy-converged wave functions are used as initial wave functions in a continuation of the energy-converged calculation. "*cont2*": like *cont1*; this time the calculation is forced to continue beyond energy convergence.

continuation of the electronic relaxation ("*cont1*"). They allow for an excellent first input charge density, which reduces the number of self consistent cycles until energy convergence to a minimum. The quality of the obtained step in the potential energy, however, gets worse!

This result can be interpreted as follows. No convergence criterion exists for the inserted dipole layer. In general, its quality increases with increasing number of performed self consistent cycles. Its convergence speed may, however, differ significantly from the convergence speed of the energy. The calculations depicted in Fig. 3.2b started from scratch. As many cycles were performed as necessary for a converged energy. In most cases, also the dipole moment has converged by then. Nevertheless, there are important exceptions (arrow in Fig. 3.2b). The different speed of convergence is illustrated best in a continued calculation, which uses the converged wave functions as input guesses ("*cont1*"). The energy converges rapidly, in most cases faster than the dipole moment (Figs. 3.2a & 3.2c). A stable dipole moment can be reached by forcing the calculations to continue for 5 to 10 cycles beyond energy convergence ("*cont2*"). A significantly improved accuracy of the step in the electron potential energy is reached this way, as depicted in Fig. 3.2d.

To summarize, the energy and the dipole moment do not necessarily converge at the same speed. Since VASP does not allow the user to set a convergence criterion for the latter, its convergence has to be checked manually. If necessary, the wave functions of the energy-converged calculation are read in in a second calculation. About 10 self consistent cycles are usually sufficient to reach convergence of the dipole moment as well.

As for the total energy, the chosen 5×8 k-point mesh does not yield fully converged results, but is a good tradeoff between accuracy and computation speed with the advantage of being consistent with former calculations performed in our group. An accuracy of about 0.02 eV with respect to the k-point grid is found for the step in the potential energy. According to Eqn. (2.4), this corresponds to an accuracy of $\Delta\mu_z < 0.005\,\text{eÅ}$ of the inserted dipole layer. Every electronic relaxation was therefore continued until the stability of μ_z was smaller than a somewhat stricter value, approx. $\Delta\mu_z < 0.002\,\text{eÅ}$. "Stability" here means, that the criterion for $\Delta\mu_z$ is fulfilled for approximately ten subsequent cycles.

3.5 Methfessel-Paxton occupation scheme

Besides the 5×8 Monkhorst-Pack k-point grid and the PW91 exchange-correlation functional, a Methfessel-Paxton occupation scheme [46] with 0.2 eV broadening was used.

The meaning and importance of the latter is explained in the following. When performing calculations in k-space, equations of the form

$$I = \int_{\text{BZ}} S(E(\mathbf{k}) - E_{\text{F}}) f(\mathbf{k}) d\mathbf{k} \tag{3.6}$$

often appear, where $S(x)$ stands for the Fermi-Dirac distribution at 0 K, $S(x) = 1 - \Theta(x)$, $\Theta(x)$ for the Heaviside step function, f for a function of physical relevance and BZ for the

irreducible wedge of the first *Brillouin zone*[d]. An equivalent one dimensional integral

$$I = \int_{-\infty}^{\infty} S(\epsilon - E_{\mathrm{F}}) F(\epsilon) d\epsilon \tag{3.7}$$

exists, where F and f are connected via $F(\epsilon) = \int_{\mathrm{BZ}} f(\mathbf{k}) \delta(\epsilon - E(\mathbf{k})) d\mathbf{k}$. For example, if the total number of electrons is to be calculated, the DOS is integrated: $F(\epsilon) = 2 * \mathrm{DOS}(\epsilon)$. In metals, where the highest band is not completely filled ($\mathrm{DOS}(E_{\mathrm{F}}) \neq 0$), S sharply cuts off the integrand at E_{F}. Due to fundamental relations between real and reciprocal space, a high quality representation of such a step requires a lot of Fourier coefficients and therefore a prohibitively fine k-point mesh. Methfessel and Paxton suggested a technique to improve the k-point convergence of such calculations at a good level of accuracy [46]. According to this approach, S is replaced by a smoother function S_N. Instead of $S(\epsilon - E_{\mathrm{F}})$ one then uses $S_N(\frac{\epsilon - E_{\mathrm{F}}}{W})$. The meaning of W, the *broadening*, will become apparent below. Like the Dirac δ-function is the "derivation" of the Heaviside Θ-function, the derivation of S_N is an approximation to δ, termed D_N. The analytic form of the latter is

$$D_N(x) = \sum_{n=0}^{N} A_n H_{2n}(x) e^{-x^2} \quad , \tag{3.8}$$

with

$$A_n = \frac{(-1)^n}{n! 4^n \sqrt{\pi}} \quad . \tag{3.9}$$

Here, H_n is the Hermite polynomial of degree n. D_N is an approximation to $\delta(x)$ insofar, as

$$\lim_{N \to \infty} D_N(x) = \delta(x) \quad . \tag{3.10}$$

$S_N(x) = \int_{-\infty}^{x} D_N(t) dt$ evaluates to

$$S_N(x) = \frac{1}{2} \left(1 - \mathrm{erf}\,(x)\right) + \sum_{n=1}^{N} A_n H_{2n-1}(x) e^{-x^2} \quad . \tag{3.11}$$

Both functions are depicted in Fig. 3.3 for different orders N. The important fact in order to understand the connection between the numerical convergence issues at the Fermi edge and a broadening is, that integrals over physical quantities $F(\epsilon)$ multiplied with $S_N(\frac{\epsilon - E_{\mathrm{F}}}{W})$ can be interpreted as integrals over the quantity F, broadened with the broadening function $\frac{1}{W} D_N(\frac{\epsilon - E_{\mathrm{F}}}{W})$:

$$F_{\mathrm{br}}(\epsilon) = \int_{-\infty}^{+\infty} \frac{1}{W} D_N(\frac{\epsilon - t}{W}) F(t) dt \quad , \tag{3.12}$$

$$\int_{-\infty}^{\infty} S_N(\frac{\epsilon - E_{\mathrm{F}}}{W}) F(\epsilon) d\epsilon = \int_{-\infty}^{E_{\mathrm{F}}} F_{\mathrm{br}}(\epsilon) d\epsilon \quad . \tag{3.13}$$

For, e.g., $F(\epsilon) = 2 * \mathrm{DOS}(\epsilon)$, this corresponds to a broadening of the DOS. The broadening amounts to 0.2 eV in the present calculations. As illustration, Fig. 3.4 shows the DOS of a gold bulk as obtained with two different broadening values W.

[d] The concept of Brillouin zones is fundamental and described in many textbooks about solid state physics.

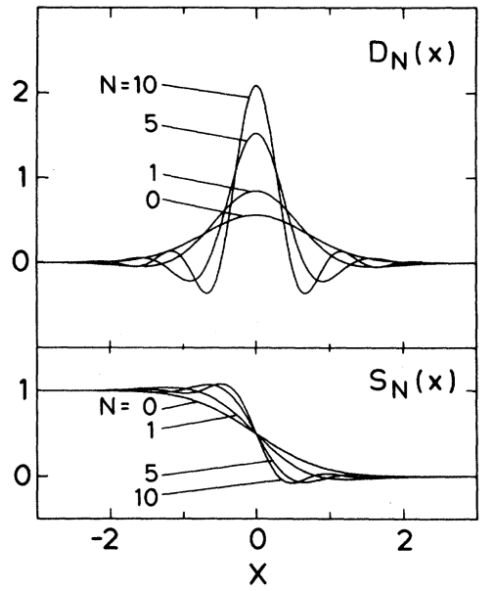

Figure 3.3: (taken from Ref. [46]) The functions S_N and D_N for different indices N. They approximate the Fermi-Dirac distribution S and the δ-function.

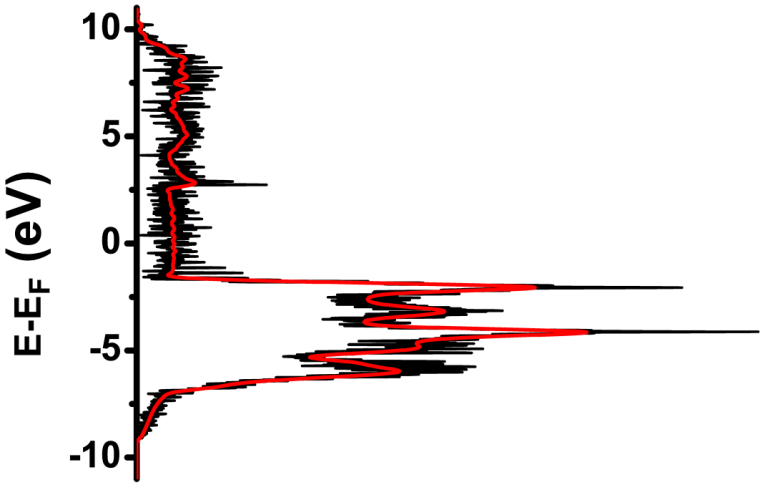

Figure 3.4: Comparison of the DOS of gold, obtained with $W = 0.02\,\text{eV}$ (black curve) and $W = 0.2\,\text{eV}$ (red curve).

In a k-space converged regime, integrals of the form (3.12) and (3.13) converge to the correct results as $W \to 0$. However, the convergence speed might be quite low.[e] A striking feature of the function S_N (D_N) is the parameter N. In a k-space converged regime, integrals (3.13) (or (3.12)) are *exact* for a certain N, as long as the function F is representable as a polynomial of degree $2N$ ($2N+1$) or less. The error is already negligible, if this requirement is fulfilled in an interval of approx. $5W$ around E_F.

3.6 Used parameters in the VASP INCAR file

In this section, the main input file for VASP calculations is presented. A standard INCAR file as it was used in the present calculations is quoted below.

```
SYSTEM = SAM_on_Au
ENCUT = 273.894
```

[e] For examples, see Ref. [46].

```
ISTART = 1
NWRITE = 2
PREC = Normal
ISPIN = 1

EDIFF = 1.E-04
EDIFFG = -1E-02
NELMIN = 50
NELM = 70
NSW = 0
IBRION = -1
POTIM = 0.17
SMASS = 0.35
ISIF = 0
ISYM = 0


Flags for Pair-Correlation function output are set to default

LORBIT = 11
EMIN = -40.
EMAX = 20.
NEDOS = 5001
ISMEAR = 1
SIGMA = 0.2
LREAL = Auto
VOSKOWN = 1
ALGO = Fast
LDIAG = .TRUE.
LPLANE = .TRUE.
NSIM = 4
NPAR = 4

Mixing tags are left at their default values

LWAVE = .TRUE.
LCHARG = .TRUE.
LELF = .FALSE.
LVTOT = .TRUE.

IDIPOL = 3
LDIPOL = .TRUE.
```

Italicized lines were present in every calculation, with their values set as quoted. They are not explained here. The other parameters are briefly introduced below as far as they were modified in this work (a comprehensive overview can be found in the VASP manual [43]):

- `SYSTEM`: Name of the calculation.
- `ENCUT`: Cutoff energy. Except for tests, 273.894 eV were used.
- `ISTART`: Read in wave functions from WAVECAR file, if present. Set to `0`, if not wanted.
- `PREC`: Sets default values for a few parameters. Except for tests, `Normal` was used.
- `EDIFF`: Convergence criterion for the total (free) energy, in eV. Except for tests, 10^{-4} eV were used.
- `EDIFFG`: Convergence criterion for the forces in geometry relaxation calculations, in eV/Å.
- `NELMIN`: Minimum number of performed self consistent cycles. Used to control the dipole moment convergence, if necessary.
- `NELM`: Maximum number of self consistent cycles (default: `60`).
- `NSW`: Maximum number of ionic steps. Set to `0` in singlepoint calculations.
- `IBRION`: Algorithm to update ionic positions. Set to `-1` in singlepoint calculations, and usually to `3` in geometry relaxations.
- `POTIM`: Parameter to control geometry relaxations. A decrease increases the reliability of the convergence progress at the cost of reduced speed. Reduced to up to `0.05` in case of convergence problems.
- `SMASS`: Parameter to control geometry relaxations. An increase increases the reliability of the convergence progress at the cost of reduced speed. Increased to up to `0.50` in case of convergence problems.
- `ISMEAR`: Smearing method; positive integers stand for the Methfessel-Paxton order. Except for tests, $N = 1$ was used.
- `SIGMA`: Smearing width. Except for tests, $W = 0.2$ eV was used.
- `LREAL`: See VASP manual [43]. In some cases, VASP asks the user to explicitly set `LREAL` to `.TRUE.` (or `.FALSE.`).
- `ALGO`: In case of convergence problems, `Normal` and `VeryFast` were tried instead of `Fast`.
- `LWAVE`: Whether to write out the resulting wave functions into the file WAVECAR. Caution: WAVECAR files need a lot of disk space!
- `LDIPOL`: Whether to use a compensating dipole layer. May cause convergence problems (in case of a vanishing dipole moment). In such cases, the wave functions of a calculation with `LDIPOL` set to `.FALSE.` are excellent starting guesses for a next calculation using `LDIPOL = .TRUE.`.

In case of convergence problems, also mixing tags were manually set.[f] In some cases, the setting

```
BMIX=3.0
AMIN=0.01
```

was successfully used.

[f] The used procedure is recommended by authors of VASP, see http://cms.mpi.univie.ac.at/vasp-workshop/slides/optelectron.pdf.

4 Metal|SAM systems

4.1 The isolated monolayers

This chapter presents the SAMs used as interlayers in the investigated three component systems. In total, nine interlayers were used. Detailed data on five of them has been published already [21] and is partly summarized here.[a] An analysis of the four remaining systems is presented in the following.

Fig. 4.1 shows the potential energies ($E - E_{\mathrm{HOPS}}$) across the layers HS|2P|F, CN|2P|CN, Pyr|2P|CN and Pyr|2P|NH_2. According to Sec. 2.4.1, the left- and right-hand IPs and EAs are depicted. Those quantities are summarized in Tab. 4.1, together with ΔE_{vac} across the respective monolayers. This table further contains the results for the previously published systems [21].

[a] Calculations were done on another system, namely Au|S|2P|F, see Ref. [47]. However, since this article does not contain detailed results, the system is investigated once more in the present work.

Table 4.1: Step in the electron potential energy ΔE_{vac} across a 2D infinite layer of molecules and left- and right-hand side IPs (EAs) $\mathrm{IP}_{\mathrm{left}}$ ($\mathrm{EA}_{\mathrm{left}}$) and $\mathrm{IP}_{\mathrm{right}}$ ($\mathrm{EA}_{\mathrm{right}}$), in eV. Data on the last five systems is taken from Ref. [21]. The system HS|2P|F is published in Ref. [47], although lacking detailed data. The numbers in the 2nd column refer to the ordering of the systems in the next chapter.

system	No.	ΔE_{vac}	$\mathrm{IP}_{\mathrm{left}}$	$\mathrm{IP}_{\mathrm{right}}$	$\mathrm{EA}_{\mathrm{left}}$	$\mathrm{EA}_{\mathrm{right}}$
HS|2P|F	6	1.41	5.23	6.64	2.15	3.56
CN|2P|CN	8	0.77	8.34	9.11	5.50	6.27
Pyr|2P|CN	7	1.72	7.21	8.93	4.48	6.20
Pyr|2P|NH_2	1	-3.36	7.23	3.87	4.13	0.77
reproduced from Ref. [21]:						
Pyr|2P|H	2	-2.45	7.19	4.74	4.31	1.86
CN|2P|H	3	-3.40	8.47	5.07	5.38	1.98
HS|1P|H	4	-0.52	5.57	5.05	1.49	0.97
HS|2P|H	5	-0.37	5.27	4.89	2.18	1.80
HS|2P|CN	9	3.84	5.17	9.01	2.34	6.18

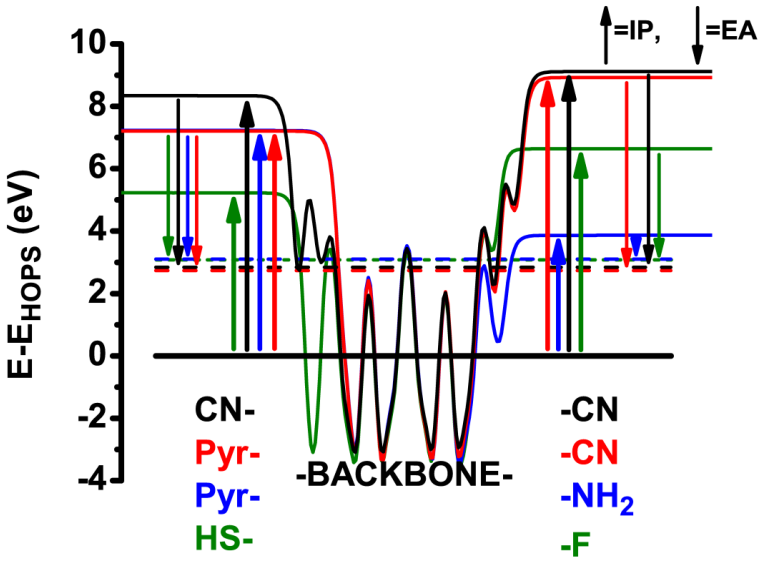

Figure 4.1: The electrostatic potential across the monolayers CN|2P|CN (black), Pyr|2P|CN (red), Pyr|2P|NH_2 (blue) and HS|2P|F (green). The systems are aligned by plotting $(E - E_{\mathrm{HOPS}})$, the HOPS is indicated by the horizontal, black line and the respective LUPS levels by dashed colored lines. Left- and right-hand IPs and EAs are indicated as vertical arrows.

4.2 Charge rearrangements & level alignment

The bond dipole (BD) that occurs upon interaction between metal and SAM is due to charge rearrangements at the interface. Those charge rearrangements are the difference between the charge density of the complete, contacted system and the sum of the charge densities of the non-interacting, separated systems (units: $-e/\text{Å}^3$), where e denotes the positive elementary charge:

$$\Delta\rho = \rho_{\mathrm{metal|SAM}} - (\rho_{\mathrm{metal}} + \rho_{\mathrm{SAM}}) \quad . \tag{4.1}$$

In case of thiol-bonded SAMs, a S-H bond is replaced by a S-Au bond upon adsorption. In this case the charge rearrangements evaluate to

$$\Delta\rho = \rho_{\mathrm{metal|SAM}} - [(\rho_{\mathrm{metal}} + \rho_{\mathrm{SAM}}) - \rho_{\mathrm{H}})] \quad , \tag{4.2}$$

where ρ_{H} denotes the charge density of the hydrogen atoms only. Altough the charge rearrangements are of course a function of the three spatial variables, it is in general more convenient to integrate $\Delta\rho(x, y, z)$ over the x, y-plane and depict the resulting function of the z-coordinate, $\Delta\rho(z) = \iint \Delta\rho(x, y, z)dxdy$ (in $-e/\text{Å}$). Integrating once over $\Delta\rho(z)$ yields the quantity

$$Q(z) = \int_0^z \Delta\rho(z')dz' \quad , \tag{4.3}$$

Table 4.2: The bond dipole (BD), the work function modification $\Delta\Phi_{\mathrm{SAM}}$, ionization potential $\mathrm{IP}_{\mathrm{SAM}}$ and electron affinity $\mathrm{EA}_{\mathrm{SAM}}$ of the bonded SAM, energetic distortion of the HOPS and LUPS ($\mathrm{E}_{\mathrm{corr}}^{\mathrm{HOPS}}$, $\mathrm{E}_{\mathrm{corr}}^{\mathrm{LUPS}}$) upon bond formation and energetic distances $\Delta E_{\mathrm{HOPS}}^{\mathrm{SAM}}$ and $\Delta E_{\mathrm{LUPS}}^{\mathrm{SAM}}$ for nine metal|SAM systems; all quantities in units of eV. The numbers in the 2nd column refer to the ordering of the systems in the next chapter, where they are sorted by ascending $\Delta\Phi_{\mathrm{SAM}}$. Uppermost part: investigated systems; middle part: reproduced from Ref. [21] for the rest of the systems; lowermost part: data on the systems in the middle part as far as accessible from the calculations presented in Chapter 5.

system	No.	BD	$\Delta\Phi_{\mathrm{SAM}}$	$\mathrm{IP}_{\mathrm{SAM}}$	$\mathrm{EA}_{\mathrm{SAM}}$	$E_{\mathrm{corr}}^{\mathrm{HOPS}}$	$E_{\mathrm{corr}}^{\mathrm{LUPS}}$	$\Delta E_{\mathrm{HOPS}}^{\mathrm{SAM}}$	$\Delta E_{\mathrm{LUPS}}^{\mathrm{SAM}}$
Au|S|2P|F	6	-1.18	0.23	6.43	3.42	0.21	0.14	-1.00	2.01
Au|CN|2P|CN	8	1.30	2.07	9.12	6.70	-0.01	-0.43	-1.81	0.61
Au|Pyr|2P|CN	7	-0.43	1.29	9.39	6.31	-0.46	-0.11	-2.87	0.21
Au|Pyr|2P|NH_2	1	-0.50	-3.86	4.23	1.11	-0.36	-0.34	-2.86	0.26
reproduced from Ref. [21]:									
Au|Pyr|2P|H	2	-0.58	-3.03	5.56	1.97	-0.83	-0.11	-3.37	0.22
Au|CN|2P|H	3	1.28	-2.12	5.06	2.50	0.00	-0.53	-1.94	0.62
Au|S|1P|H	4	-1.05	-1.57	4.72	1.08	0.32	-0.11	-1.09	2.55
Au|S|2P|H	5	-1.17	-1.55	4.69	1.70	0.21	0.11	-1.03	1.96
Au|S|2P|CN	9	-1.18	2.65	8.84	6.12	0.16	0.05	-0.99	1.73
no analysis performed:									
Au|Pyr|2P|H	2	-	-3.05	5.55	1.96	-	-	-3.37	0.22
Au|CN|2P|H	3	-	-2.12	5.05	2.50	-	-	-1.93	0.62
Au|S|1P|H	4	-	-1.54	4.74	1.10	-	-	-1.09	2.55
Au|S|2P|H	5	-	-1.54	4.68	1.70	-	-	-1.02	1.96
Au|S|2P|CN	9	-	2.66	8.84	6.12	-	-	-0.98	1.74

which describes the cumulative charge transfer along the z-axis of the unit cell (units: $-e$). A positive value of Q at a certain position z', $Q(z') = Q' > 0$, stands for the fact that Q' electrons are transferred from regions with larger to regions with smaller z-coordinates. Q crossing the zero line, $Q(z') = 0$, stands for the fact that *no* charge is transferred across the x, y-plane with z-coordinate z'.

By solving the one-dimensional Poisson equation for $\Delta\rho$ one obtains their effect on the electron potential energy E:

$$\frac{d^2\Phi_{\mathrm{el}}}{dz^2} = -\frac{\Delta\rho(z)}{\epsilon_0} \quad \Rightarrow \quad E = -e\Delta\Phi_{\mathrm{el}} \quad , \qquad [2.5]$$

with ϵ_0 being the vacuum permittivity. The overall effect on E is denoted as the BD (compare Fig. 2.7).

Those three quantities are depicted in Fig 4.2 for the systems (**6**), (**8**), (**7**) and (**1**). For the systems Au|S|2P|F and Au|CN|2P|CN, the charge rearrangements upon adsorption of the SAM are localized at the metal|SAM interface. The red areas indicate electron density accumulation and the blue areas electron density depletion. Essentially vanishing

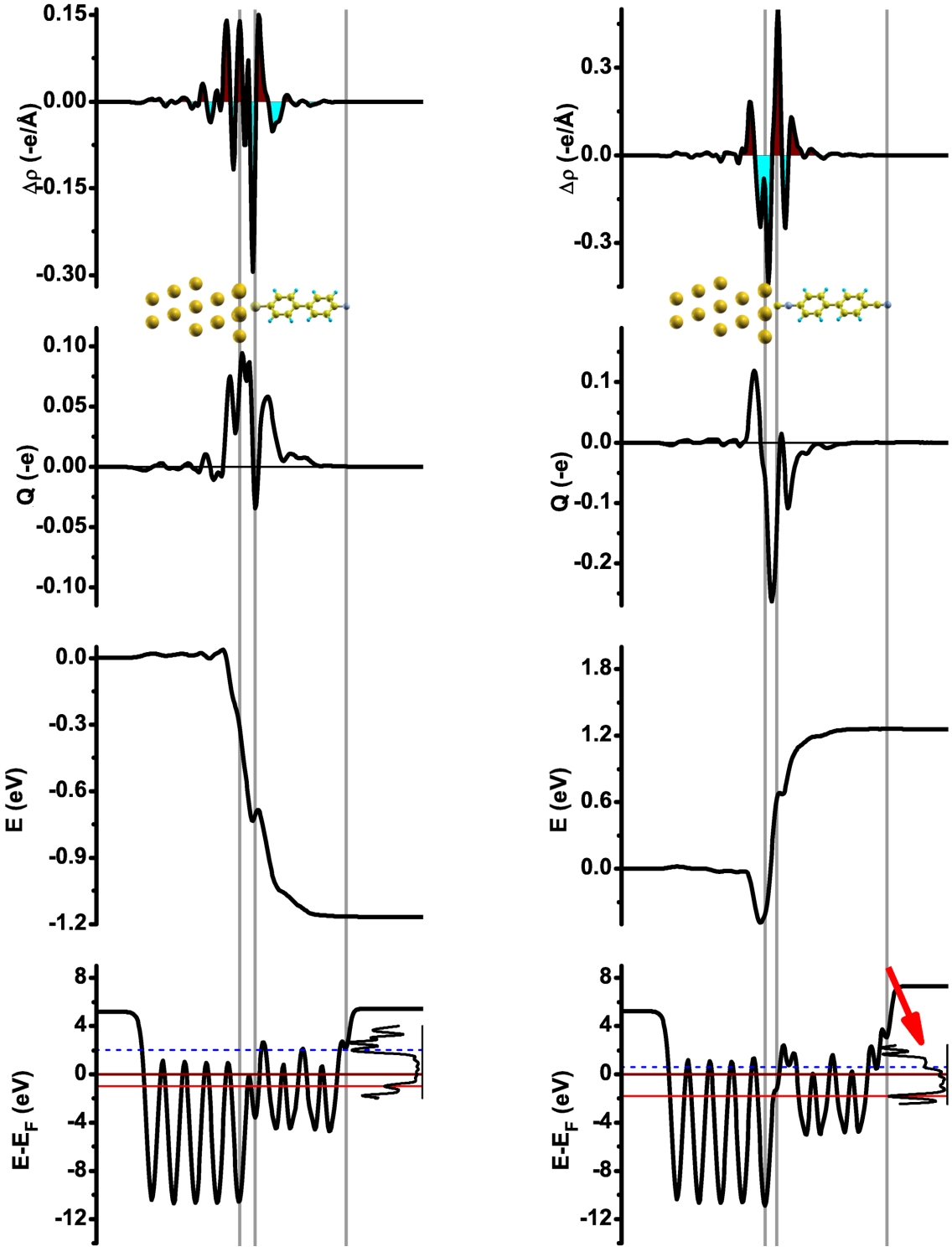

(a) (**6**): Au|S|2P|F (b) (**8**): Au|CN|2P|CN

Figure 4.2: (1st part) The top panels show the charge rearrangements $\Delta\rho$ upon adsorption of the SAM, integrated over the plane parallel to the gold surface (units: $-e/\text{Å}$). The red areas indicate electron density accumulation and the blue areas electron density depletion. Below, the accumulated charge transfer $Q(z)$ (unit: $-e$) is depicted. Additionally, the effect of $\Delta\rho$ on the electrostatic energy of an electron E is shown in eV. The lowermost panels show the electron potential energy across the systems, the energy levels E_F (dark red), HOPS (red) and LUPS (dashed blue) of the SAM and the DOS of the SAM atoms around E_F.

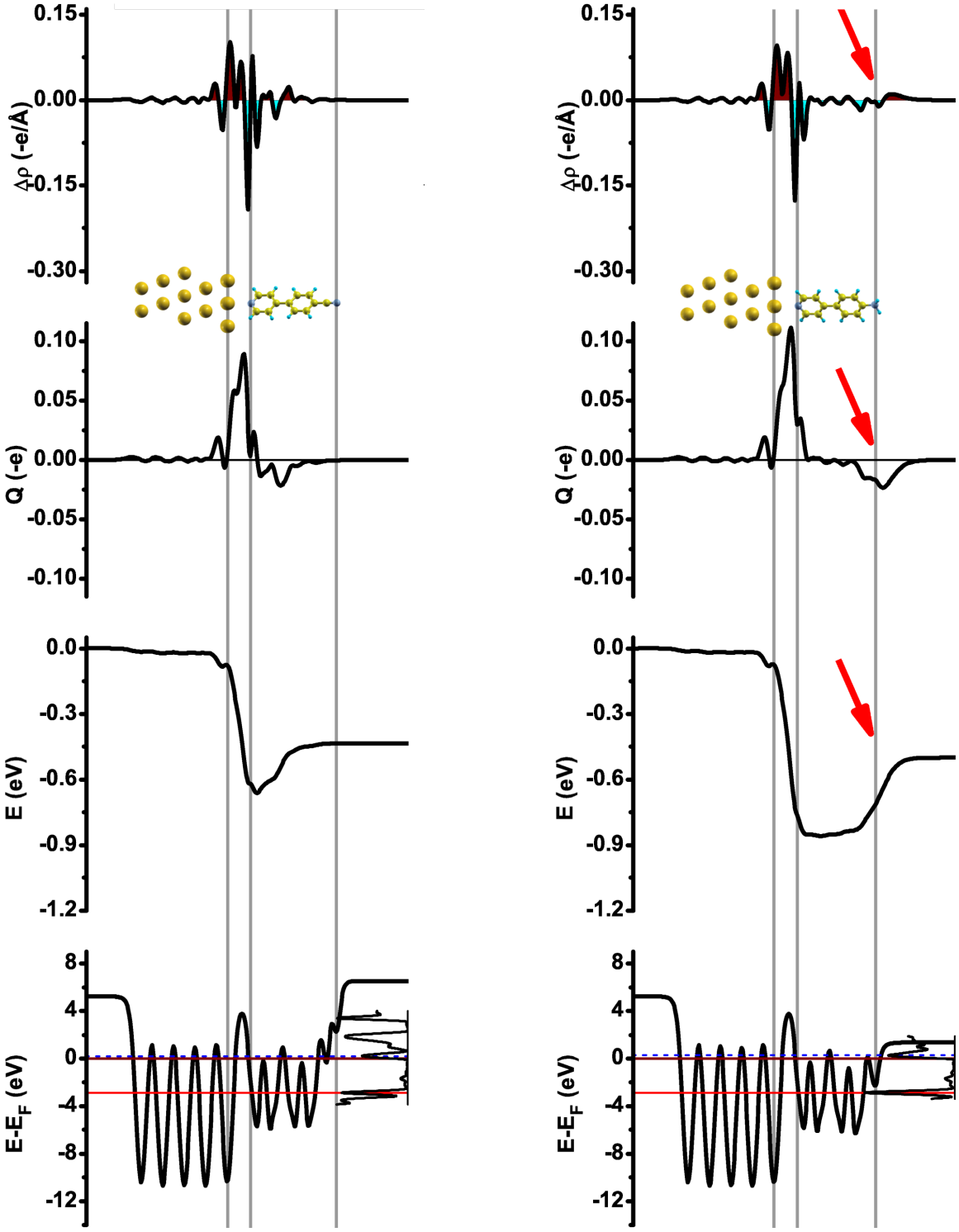

(c) (**7**): Au|Pyr|2P|CN (d) (**1**): Au|Pyr|2P|NH_2

Figure 4.2: (2^{nd} part) Mind that the plots in (b) differ by a factor 2 in scale from the plots in (a), (c) and (d) (except the lowermost plots). The meaning of the results denoted by the arrows is explained in the text.

net charge transfer takes place across the metal|SAM interface, as can be seen from the Q-plot for those systems. Instead, dipoles emerge in the topmost metal layers and in the lowermost SAM-region. They give rise to significant BDs of -1.18 and $1.30\,\mathrm{eV}$ (see E-plots & Tab. 4.2). The two docking groups thiolate (Au|S...) and isocyanide (Au|CN...) differ in the sign of the BD, while they are comparable in magnitude.

In the system Au|Pyr|2P|CN, $\Delta\rho$ looks similar to the previous two curves at first glimpse. However, there is an interesting difference, which can be seen best in the Q-plot. The direction of the local charge transfer within the SAM differs from the transfer direction at the interface. Hence, $\Delta\rho$ introduces a shift in the electron potential energy that counteracts the shift at the interface. As a result, the BD of approx. $-0.66\,\mathrm{eV}$ directly at the interface is reduced to $-0.43\,\mathrm{eV}$ by the rearrangements in the backbone of the SAM. This effect can be rationalized by looking at the energy level alignment in this system. As the lowermost panel illustrates, the distance between the maximum of the SAM LUPS peak and E_F is very narrow. According to Tab. 4.2, which summarizes the interface energetics numerically, it amounts to only $\Delta E_\mathrm{LUPS} = 0.21\,\mathrm{eV}$. If the BD was not reduced by $0.23\,\mathrm{eV}$, the energetic distance ΔE_LUPS would even be negative: $0.21 - 0.23 = -0.02\,\mathrm{eV}$. The observed $\Delta\rho$ prevent such an energetically unfavorable situation of a LUPS below E_F. Interestingly, this is reached by a polarization of the backbone instead of charge transfer from the metal to the SAM. This can be seen from the rearrangements in the molecular region of the system, which correspond to the two negative dips in the Q-plot. To summarize, the LUPS of the SAM is *pinned* at the metal Fermi level. As a consequence, polarization of the backbone reduces the magnitude of BD by about $0.23\,\mathrm{eV}$.

An interesting and not yet fully understood result is obtained for Au|Pyr|2P|NH_2, where ΔE_LUPS amounts to $0.26\,\mathrm{eV}$. Here, this value is not the result of LUPS pinning as can be seen from the corresponding E-plot: the BD of approx. $-0.85\,\mathrm{eV}$ at the interface is not reduced throughout the backbone of the SAM; no pronounced polarization of the backbone is seen in $\Delta\rho$ and Q. However, charge transfer is found from the upper ring and the head group to *above* the SAM (see red arrows in the plots for this system)! While $\Delta\rho$ in this part of the system is not significant regarding the magnitude, it extends over a considerable distance (see Q-plot). Hence, the charge rearrangements reduce the BD to $-0.50\,\mathrm{eV}$ near the head group of the SAM. This result appears to be a computational artifact, although various tests did not support this interpretation so far.

The following tests were performed:

1. a finer k-point mesh was used: $10 \times 16 \times 1$
2. a finer k-point mesh was used: $5 \times 8 \times 2$
3. a higher cutoff energy was used: $E_\mathrm{cut} = 547.788\,\mathrm{eV}$
4. `PREC` was set to `Accurate` in the INCAR file
5. the position of the compensating dipole layer was set manually using the tag `DIPOL` in the INCAR file (see Ref. [43])
6. a different smearing method was used by setting `ISMEAR = -5` (Tetrahedron method with Blöchl corrections instead of first order Methfessel-Paxton smearing, see Ref. [43])

7. hard PAW pseudopotentials were used instead of soft ones (see Refs. [44, 43])

8. the *xc*-functional was exchanged: PBE [48] was used instead of PW91

None of those calculations modified those results significantly. Hence, they remain inconclusive so far.

The values of all interesting quantities are tabulated in Tab. 4.2. Additionally, this table contains the same information for the five remaining metal|SAM systems, taken from Ref. [21]. As far as accessible from the performed calculations, they were also determined in this work (lowermost part). A comparison shows that only minor differences to the data published in Ref. [21] were seen.

As explained in the first chapter, the dipoles responsible for $\Delta\Phi_{\mathrm{SAM}}$ are not located in the molecular backbone unless Fermi level pinning takes place. This is nicely illustrated by a comparison of systems (**4**) and (**5**). They do only differ in the length of the backbone, i.e., the number of rings. Consequently, the resulting work function modifications are (almost) identical.

4.3 Determining the quantities of interest

Problems. A comparison of the values in the second and third part of Tab. 4.2 shows marginal deviations of a few hundredth of an eV. They stem from two difficulties in the evaluation of the computations.

First, not all values can be determined with the same accuracy. ΔE_{vac}, BD and $\Delta\Phi$ are derived from *numbers* in the VASP output files, so their accuracy is easily estimated from the convergence of the corresponding numbers.[b] In contrast, the positions of energy levels (and therefore also the correction energies) were determined graphically from the DOS, and IPs and EAs graphically from the DOS and the plane averaged electron potential energy. There is a certain imprecision in this technique, which is due to the artificial as well as the physical broadening of the corresponding peaks in the DOS. As an example, a closer look is taken at the DOS projected onto the SAM atoms for a problematic case, the system Au|CN|2P|CN (Fig. 4.3). It illustrates the problems in determining the exact position of the LUPS in this case. While the distinct HOPS peak maximum can be determined with good accuracy, this task is complicated for the broader LUPS peak.

Second, a more subtle problem exists. It concerns the comparison of quantities obtained from different calculations, e.g. the work function of the pristine metal slab with the one of the SAM covered metal slab to determine $\Delta\Phi_{\mathrm{SAM}} = \Phi_{\mathrm{mod}} - \Phi_{\mathrm{Au(111)}}$ (compare Eqns. (2.7) & (2.6)). It seems to be rational to take the value obtained from the isolated metal slab, including the surface reconstructions of a gold surface at vacuum as $\Phi_{\mathrm{Au(111)}}$. Those reconstructions have a slight influence on Φ and therefore the work function at this surface slightly differs from the one of a metal surface without any surface reconstructions. In case of Au(111), the reconstructions imply an increase of Φ from 5.20 to 5.22 eV. Further, Φ is influenced by the Fermi energy of the metal (see Sec. 2.1). In principle, the

[b] Despite the graphical explanations of those quantities in Sec. 2.4.1, they are in fact derived by comparing the compensating dipole moments inserted by VASP (compare Eqn. (2.3)). This technique is more exact than a graphical analysis of the plane-averaged potential energy curves.

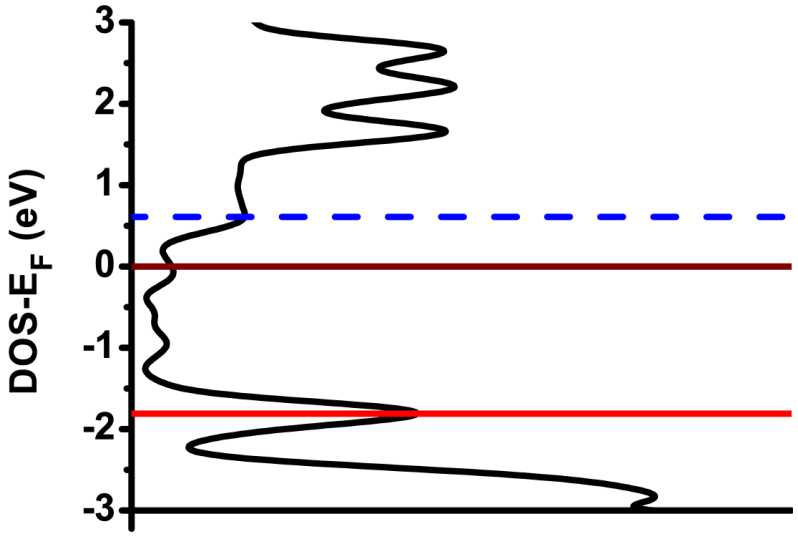

Figure 4.3: The DOS projected onto the SAM atoms for the system Au|CN|2P|CN (compare Fig. 4.2). A certain inaccuracy arises from a visual determination of the positions of the peak maxima, especially for the broad LUPS peak. HOPS, E_F and LUPS are drawn as red, dark red and dashed blue lines.

Fermi energy of a metal is the same in the isolated metal slab and in the SAM covered metal. Hence, a comparison between the work functions of both systems is - in principle - legitimate.

However, since the metal bulk is approximated by only five layers of gold, E_F is usually slightly influenced by the contact to the SAM (electron density with an energy around E_F is added to or removed from the metal), affecting Φ as well. This effect is not accounted for if $\Delta\Phi_{SAM}$ is determined by a comparison of the work function of the pristine metal slab with the one of the SAM covered metal. If one sticks to work functions obtained from only one system, i.e., one defines $\Delta\Phi_{SAM}$ as the difference between the vacuum levels at the *left* side of the metal and the *right* side of the SAM, this problem can be avoided. Since the left three layers of gold atoms are held fixed during geometry relaxation calculations, this approach leaves the surface reconstructions at vacuum unconsidered.

The data in Ref. [21] were generated using the method which considers the surface reconstructions instead of the shift in E_F.

Chosen way out. In this work, the surface reconstructions at vacuum remain unconsidered, but the shift in E_F is considered.

To sum up, the determination of the quantities of interest was performed as follows:

- $\Delta\Phi_{SAM}$: by reading out the dipole moment μ_z of the whole system[c], and multiplying it with some constants according to Eqn. (2.3).

[c]For this purpose, the command `grep dipolm OUTCAR | tail -1` was used.

Table 4.3: $\Phi_{\mathrm{Au(111)}}$ as calculated from Eqns. (2.8), according to the values in Tabs. 4.1 & 4.2, in eV.

system	No.	$\Phi^{\mathrm{HOPS}}_{\mathrm{Au(111)}}$	$\Phi^{\mathrm{LUPS}}_{\mathrm{Au(111)}}$
Au|S|2P|F	6	5.20	5.20
Au|CN|2P|CN	8	5.24	5.24
Au|Pyr|2P|CN	7	5.23	5.23
Au|Pyr|2P|NH_2	1	5.23	5.23
Au|Pyr|2P|H	2	5.23	5.22
Au|CN|2P|H	3	5.25	5.25
Au|S|1P|H	4	5.21	5.20
Au|S|2P|H	5	5.20	5.20
Au|S|2P|CN	9	5.20	5.20

- ΔE_{vac}: by reading out the dipole moment μ_z of the monolayer and multiplying it with some constants according to Eqn. (2.3).
- BD: by substraction according to Eqn. (2.6). Note, that this approach does *not* substract the effect of the dipole moment of the metal slab. **Hence, the ionic reconstructions of the two uppermost metal layers upon bond formation are included in the BD.**
- ΔE-values: graphically from the DOS.
- IPs, EAs: graphically from the averaged electron potential energy and the ΔE-values.
- E_{corr}-values: calculated from other quantities ($E^{\mathrm{HOPS}}_{\mathrm{corr}} = \mathrm{IP}_{\mathrm{right}} - \mathrm{IP}_{\mathrm{SAM}}$, $E^{\mathrm{LUPS}}_{\mathrm{corr}} = \mathrm{EA}_{\mathrm{right}} - \mathrm{EA}_{\mathrm{SAM}}$).

An effect of the methodological problems described above can be easily seen from Eqns. (2.8). Taking the values of Tabs. 4.1 & 4.2, $\Phi_{\mathrm{Au(111)}}$ can be determined twice per system via Eqns. (2.8). The obtained values are listed in Tab. 4.3. Variations amount to 0.04 eV for the systems investigated in the present chapter and to 0.05 eV for all systems, which is acceptable. Due to the definition of the correction energies, $\Phi^{\mathrm{HOPS}}_{\mathrm{Au(111)}}$ and $\Phi^{\mathrm{LUPS}}_{\mathrm{Au(111)}}$ equal for every calculation.

5 Metal|SAM||OSC systems

As the properties of the metal|SAM systems are known now, a monolayer of a prototypical organic semiconductor (OSC) is added to each of the nine systems to investigate and understand the level alignment in the full three component systems. As described above, biphenyl (2P) is chosen as OSC because of its molecular size and its structural similarity to the investigated SAMs. The former helps keeping the computational costs moderate, and the latter facilitates the addition of the 2P to the metal|SAM unit cell.

Before the main results of the present work are presented, the isolated monolayer of biphenyl is studied.

5.1 The 2P monolayer

Similar to the present SAMs, the 2P molecular crystal shows a herringbone pattern (Fig. 5.1). In both cases the lattice vectors **a** and **b**, which span a plane parallel to the metal surface in the present investigations, enclose an angle of 90 °. Going from the 2P bulk cell to the metal|SAM cell, **a** is elongated and **b** is shortened. However, $(|\mathbf{a}| \times |\mathbf{b}|)_{\mathrm{SAM}} \approx 8.86 \times 5.11 \approx 45.3\,\text{Å}^2$ [28] and $(|\mathbf{a}| \times |\mathbf{b}|)_{\mathrm{2P}} \approx 8.12 \times 5.63 \approx 45.7\,\text{Å}^2$

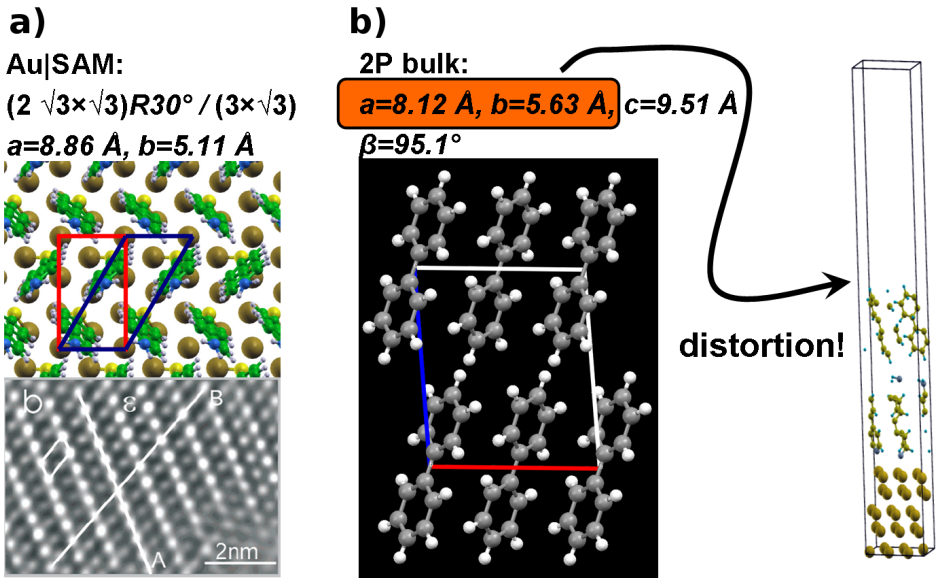

Figure 5.1: a) Experimentally determined structure of the SAMs (upper picture made by G. Heimel, lower picture taken from Ref. [28]). b) Orthorhombic 2P bulk unit cell; it is distorted to match the Au|SAM unit cell.

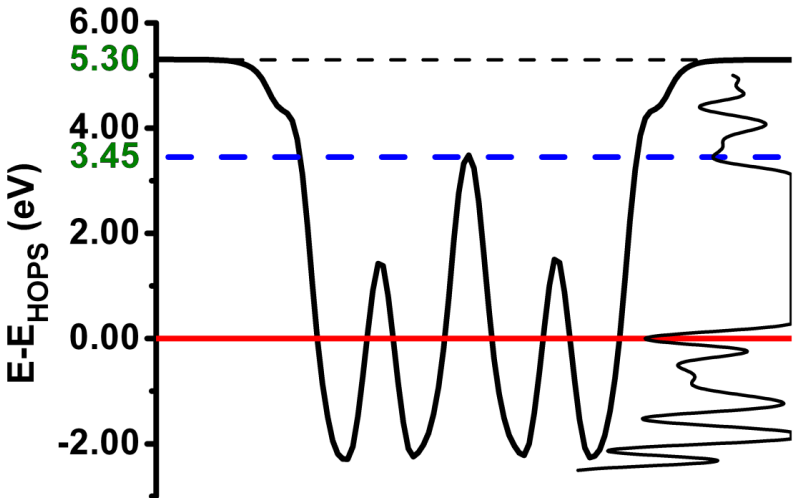

Figure 5.2: Potential energy of an electron across a 2P monolayer, HOPS (red line), LUPS (dashed blue line) and DOS around those levels. The left an right hand vacuum levels are connected by a horizontal, dashed black line to illustrate that they are situated at virtually identical energies.

[49, 50] define an almost identical area in which the two herringbone arranged molecules are placed. The fact that the 2P bulk unit cell is of orthorhombic shape with an angle $\beta := \measuredangle(\mathbf{a}, \mathbf{c}) = 95.1\,^\circ$ does not play a role in the present calculations, because only monolayers are present. It is therefore plausible to construct the full three component unit cells under the assumption, that upon contact at least the first 2P layer adopts the same unit cell as the metal|SAM system. This is also insofar reasonable, as the ability of organic thin films to act as templates for the heteroepitaxial growth of other organic layers has been observed experimentally [51, 52].

The layer was geometry optimized, with the only constrained degrees of freedom being the z-coordinates of the lowermost hydrogen atoms of the layer (to keep the layer even). The potential energy of an electron across this modified 2P monolayer, its HOPS and its LUPS are summarized in Fig. 5.2. Due to the symmetry of the molecules, ΔE_{vac} amounts to a nearly vanishing value of $\Delta E_{\text{vac}} < 0.01\,\text{eV}$ for this monolayer.

Convergence of the dipole moment. In most of the monolayer calculations, great convergence problems were observed. Those computational problems are connected to difficulties in the convergence of the inserted compensating dipole layer perpendicular to the metal surface. Since such problems did not occur elsewhere, it seems that convergence towards zero is problematic. A solution is to switch off the insertion of a dipole layer in a first calculation (by using the tag `LDIPOL=.FALSE.`; this leads to fast convergence), and use the resulting wave functions as initial wave functions in a calculation with switched on dipole layer (`LDIPOL=.TRUE.`). This technique yields values of $\Delta E_{\text{vac}} < 0.01\,\text{eV}$.

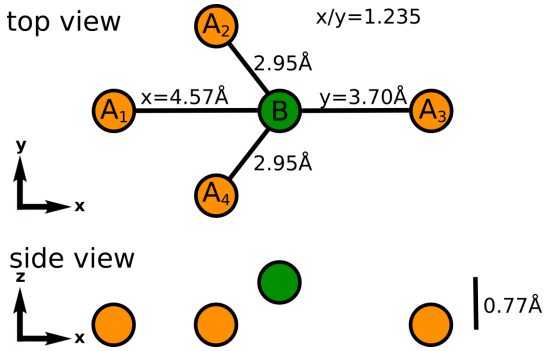

(a) Distances between the lowermost hydrogen atom of a layer of 2P (green) and the four nearest topmost hydrogen atoms in the adjacent layer (orange) in the 2P bulk structure [49] (top) and distance between two layers in the 2P bulk structure (bottom).

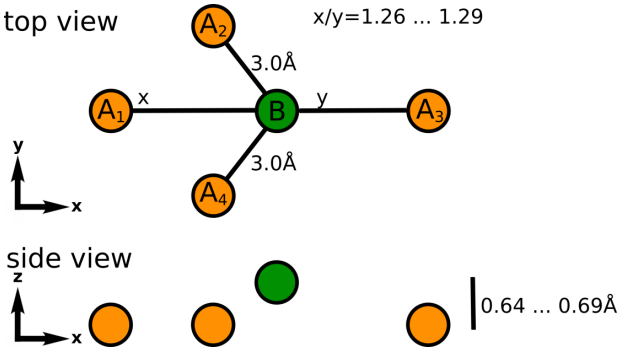

(b) Distances between the lowermost fluorine atom of a layer of 4,4'-Difluorobiphenyl (green) and the four nearest topmost fluorine atoms in the adjacent layer (orange) in the 4,4'-Difluorobiphenyl bulk structure (top) and distance between two layers (bottom). The values are approximate averages over six data sets, obtained from the CCDC [53, 54].

Figure 5.3: Available experimental data to model the geometry at the SAM||2P interface for the SAM head groups hydrogen and fluorine.

5.2 Adding the 2P monolayer

As discussed in Sec. 3.3, van der Waals forces are not correctly accounted for in DFT. For this reason, the geometry at the SAM||2P interface could not be optimized. The approach to handle this problem was to set the position of the biphenyl "by hand" and carefully test to what extend the results depend on the exact position of the 2P. If available, the 2P layer was placed according to experimental data (see below). The biphenyl monolayer was assumed to be strictly even in the present work. Since the two SAM molecules in the unit cell are not equivalent, they can be inclined by (slightly) different tilt angles with respect to the metal surface normal. This implies slightly different heights of the molecules. Therefore, the inter-atomic distances mentioned in the following paragraphs are to be understood as approximate averages over the configurations of both molecules in the unit cell.

Since the interfacial geometry is determined by the head group of the SAM, four different kinds of interfaces had to be considered. The choice of the position of the 2P monolayer for the different head groups is described in the following.

Hydrogen (-H) terminated SAMs: Fig 5.3a shows the distances between the lowermost hydrogen atom of a 2P molecule (center, in green) and the four nearest topmost hydrogen atoms in the adjacent layer (in orange) in the experimentally determined 2P bulk structure. Additionally, the vertical distance between two layers in the bulk structure is shown in a side view. The position of the upper (green) hydrogen atom is symmetric with respect to the y-coordinates of the other hydrogen atoms, and the ratio between its distance to the leftmost and to the rightmost hydrogen atom in the figure, $\overline{A_1B}/\overline{BA_3}$, amounts to approx. 1.235. This ratio is regarded as a physically relevant quantity here, since the

absolute distances, as they are influenced by the unit cell size, can not be kept constant when switching from the 2P bulk to the metal|SAM unit cell. Additionally, the distance between SAM and 2P (defined in analogy to the inter-layer distance in Fig. 5.3) was set to equal the distance between two layers in the 2P bulk structure, implying a reduction of the distances corresponding to $\overline{A_2B} \approx \overline{BA_4}$ to approx. 2.70 Å (instead of 2.95 Å). This value exceeds the sum of the van der Waals radii[a] of the two atoms by approx. 0.3 Å.

Fluorine (-F) terminated SAM: Six different bulk structure measurements of the molecule 4,4'-Difluorobiphenyl were considered as guideline to model this interface, obtained from the Cambridge Crystallographic Data Centre (CCDC) [53, 54]. 4,4'-Difluorobiphenyl is a modified biphenyl molecule, in which the hydrogen atoms at the "end" of the rod-like molecule are substituted by fluorine atoms. In the terminology used for SAMs, it is denoted as F|2P|F. The distances between the lowermost fluorine atom in a layer and the four uppermost fluorine atoms in the layer next to it are depicted in Fig. 5.3b. Since in the present case, only the SAM-side of the interface is fluorine-terminated, i.e., a ...2P|F||H|2P... interface is present instead of a ...2P|F||F|2P... interface, intermediate distances and ratios between those of Figs. 5.3a & 5.3b were assumed to be reasonable values. Again, the ratio $\overline{A_1B}/\overline{BA_3}$ was conserved (approx. 1.258) and the distances $\overline{A_2B} \approx \overline{BA_4}$ were chosen to exceed the sum $r_{\mathrm{F}}^{\mathrm{vdW}} + r_{\mathrm{H}}^{\mathrm{vdW}}$ by approx. 0.3 Å in the modified unit cell. Because $r_{\mathrm{F}}^{\mathrm{vdW}} > r_{\mathrm{H}}^{\mathrm{vdW}}$, this procedure implies a vertical distance between the 2P layer and the SAM of approx. 1.38 Å compared to approx. 0.72 Å, which is the average between the values in Figs. 5.3a & 5.3b. However, fixing the interatomic distances and the ratio $\overline{A_1B}/\overline{BA_3}$ was regarded as more important than fixing the distance between the two monolayers.

Cyano (-CN) terminated SAMs: In this case, no experimental data was available as guide, so that the ratio $\overline{A_1B}/\overline{BA_3}$ could not be regarded as a quantity to stick to. In analogy to the previous head groups, a ratio of approx. 1.24 was assumed. The chosen distance of approx. 3.05 Å again exceeds the sum of the van der Waals radii by approx. 0.30 Å, leading to a distance of approx. 1.58 Å between the two monolayers.

Amino ($-NH_2$) terminated SAMs: The amino terminated SAM differs most from the unsubstituted, hydrogen terminated SAMs in terms of geometry because of the spatial extension of the head group. Short of experimental data, no guidelines were available to choose the interfacial geometry in this case. The z-coordinate of the lowermost hydrogen atoms belonging to the 2P was chosen in a way that their distances to the nearest hydrogen atoms belonging to the amino groups amounted to 2.66 Å and 2.93 Å for the two molecules in the unit cell, respectively.

The (un)importance of the interfacial geometry: Since the strategy to add the 2P to the unit cell described above comprises some assumptions, it is of great importance to test the dependence of the quantities of interest on the exact position of the biphenyl layer. For this purpose, the z-coordinate of the 2P layer was shifted by ±0.3 Å and the x-coordinate was shifted by 1/4 of the lattice vector **a** (long side of the unit cell) for every SAM head

[a] The van der Waals radii of the different species were taken from the database http://webelements.com: $r_{\mathrm{H}}^{\mathrm{vdW}} = 1.20$ Å, $r_{\mathrm{C}}^{\mathrm{vdW}} = 1.70$ Å, $r_{\mathrm{N}}^{\mathrm{vdW}} = 1.55$ Å, $r_{\mathrm{F}}^{\mathrm{vdW}} = 1.47$ Å.

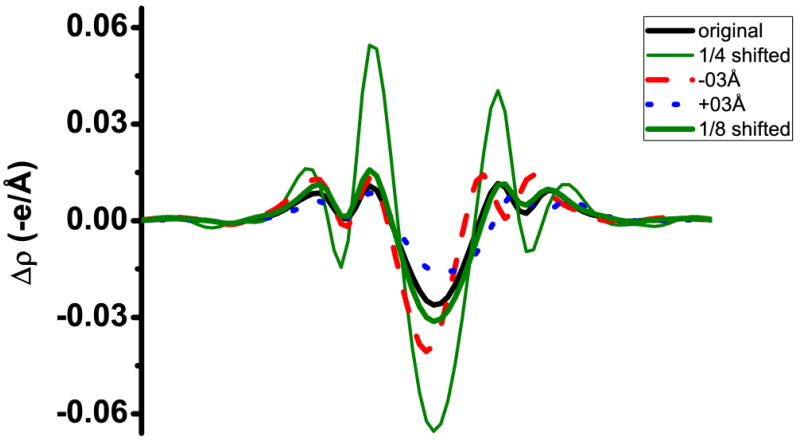

Figure 5.4: Comparison of the charge rearrangements $\Delta\rho$ for four different geometries in a system with hydrogen terminated SAM molecules. The black line shows $\Delta\rho$ for the system as described in the text ("*original*") and the dashed red (dotted blue) line depicts the same quantity for the 2P being shifted by 0.3 Å towards (away from) the SAM. Shifting the 2P by 1/4 of the lattice vector **a** (corresponding to a shift of atom B towards atom A_3 in Fig. 5.3a) yields the result depicted as thin green line. In this case, a quantitatively significantly different result is found, which is due to a too small distance between the interfacial hydrogen atoms ($1.89\,\text{Å} < 2r_{\text{H}}^{\text{vdW}} = 2.40\,\text{Å}$). The deviations vanish if the shift is reduced to 1/8**a** (thick green line).

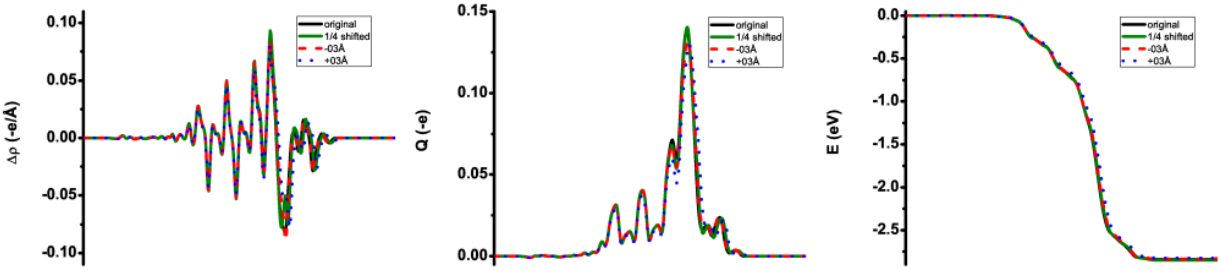

Figure 5.5: Charge rearrangements $\Delta\rho$, cumulative charge transfer Q and effect of $\Delta\rho$ on the electrostatic energy of an electron, E, for four different geometries at the SAM||2P interface in a system with cyano terminated SAM molecules. Black, dashed red, dotted blue and green curves show the results for the geometry as described in the text ("*original*"), shifted by 0.3 Å down- and upwards and by 1/4**a**, respectively. Within this range, the results are very insensitive to the position of the 2P.

group. It was found that the position of the energy levels varies by less than approx. 0.05 eV, and the importance of the changed geometry on the charge rearrangements $\Delta\rho$, cumulative charge transfer Q and the effect of $\Delta\rho$ on the electrostatic energy of an electron E are only minor too, as long as no van der Waals spheres intersect. Intersection of van der Waals spheres was only found once during those tests, namely, when the 2P layer was shifted by 1/4**a** in a system with hydrogen-terminated SAM. The smallest distance between two nearest neighbor hydrogen atoms (corresponding to the distance $\overline{BA_3}$ in Fig. 5.3a) amounts to only 1.89 Å in this configuration. Even in this case, the qualitative picture drawn in this work holds, although the results are affected quantitatively. To illustrate the variation of the results, Fig. 5.4 shows $\Delta\rho$ for a hydrogen terminated SAM for the different interfacial geometries. Without going into detail here about the interpretation of the plot, it is to be stressed again that the shape of all plots is largely independent of the exact position of the 2P and quantitative changes become important only in the case where van der Waals radii intersect (thin green line). If the shift is reduced to 1/8**a**, the quantitative deviations are significantly reduced.

$\Delta\rho$, Q and E are plotted in Fig. 5.5 for the same variations of the interfacial geometry in the case of a cyano head group. In this case, $\Delta\rho$ is much more pronounced (mind the scale!). Still, the changes in the interfacial geometry do not significantly affect any of the quantities.

5.3 Metal|SAM||OSC: level alignment

As described in Sec. 2.4.2, the first part of the main results - the level alignment at nine metal|SAM||OSC systems - is presented here. Fig. 2.9 showed, that three qualitatively different energetic configurations can be constructed by covering the Au(111) surface with a proper SAM:

(i) the Pyr|2P|NH_2 SAM (system (**1**)) causes the situation as depicted in Fig. 2.9c (LUPS pinning expected),

(ii) systems (**2**)-(**5**) correspond to the configuration in Figs. 2.9a & 2.9b (vacuum level alignment expected), and

(iii) systems (**6**)-(**9**) to Fig. 2.9d (HOPS pinning expected). Systems (**6**)-(**9**) differ in the magnitude of $\Delta\Phi_{\mathrm{SAM}}$. Given that HOPS pinning is found indeed, this difference facilitates the analysis of the pinning process: whatever effect it is that prevents the 2P HOPS from lying above E_{F}, it is expected to be more pronounced in system (**9**) than in system (**6**).

The level alignment diagrams which were actually found in the calculations are summarized in Fig. 5.6.

Each diagram shows the work function of the pure gold slab (left third), the change of the work function $\Delta\Phi_{\mathrm{SAM}}$ due to adsorption of the SAM (middle third) and the work function modification $\Delta\Phi_{\mathrm{2P}}$ which arises from the addition of 2P to the metal|SAM system (right third) as black, horizontal lines. $\Delta\Phi_{\mathrm{2P}} = 0$ is equivalent with the statement that the vacuum levels of the systems metal|SAM and 2P align, $\Delta\Phi_{\mathrm{2P}} \neq 0$ expresses a deviation from this so called Schottky-Mott limit. Additionally, the DOS projected onto the SAM (biphenyl) region of the complete three component system is displayed as blue (red) line. The identified HOPS and LUPS are depicted as thin horizontal lines at the respective

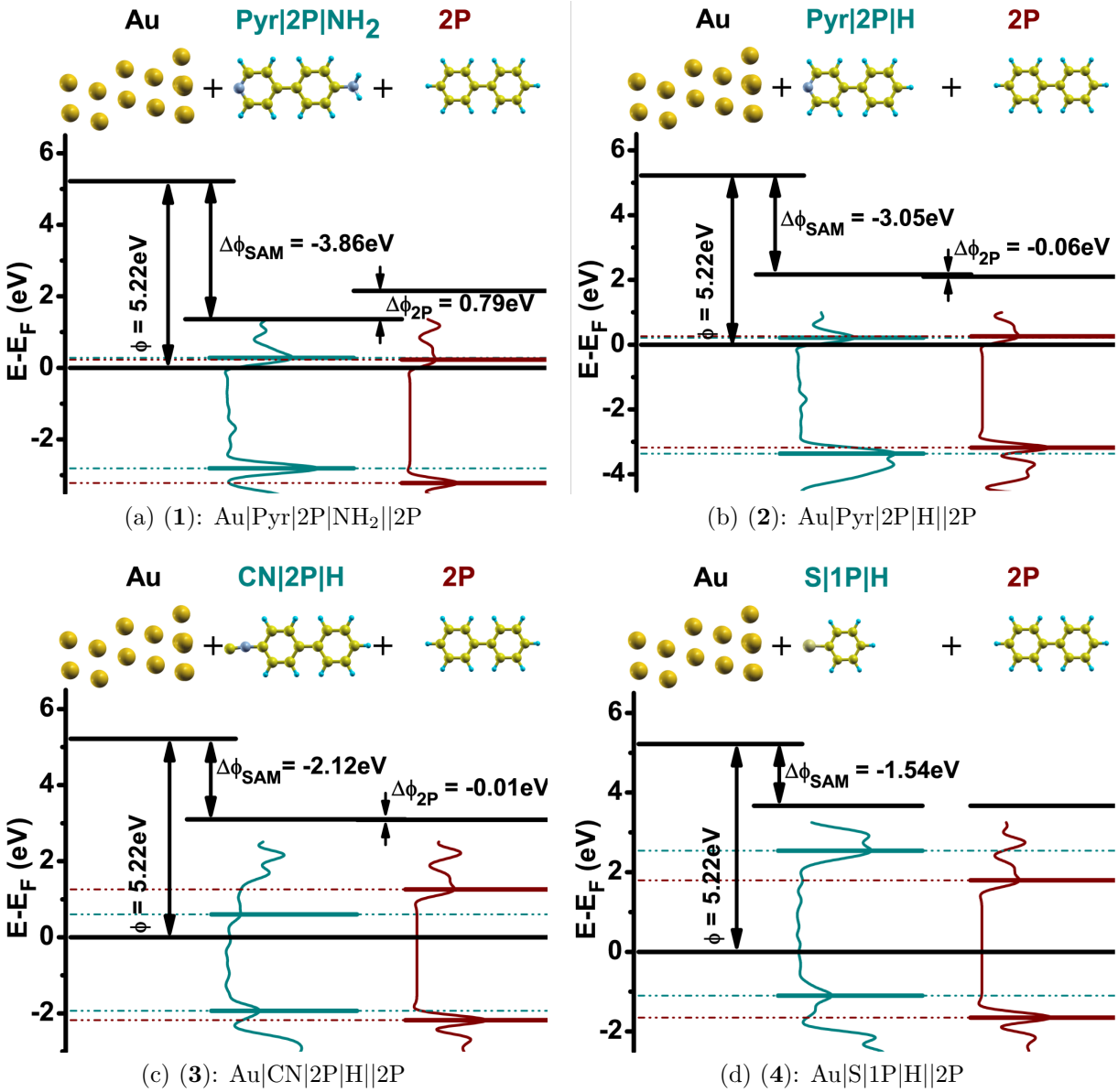

(a) (**1**): Au|Pyr|2P|NH_2||2P

(b) (**2**): Au|Pyr|2P|H||2P

(c) (**3**): Au|CN|2P|H||2P

(d) (**4**): Au|S|1P|H||2P

Figure 5.6: (1st part) Level alignment diagrams for the nine investigated three component systems. Each diagram shows the work function of the pristine gold slab (left third), the change in the work function $\Delta\Phi_{\mathrm{SAM}}$ due to adsorption of the SAM (middle third) and the work function modification $\Delta\Phi_{\mathrm{2P}}$ which arises upon addition of 2P to the metal|SAM system (right third) as black, horizontal lines. Note that the energy axis is shifted by E_{F}. Additionally, the DOS projected onto the SAM (biphenyl) region of the complete three component system is displayed as blue (red) line. The identified HOPS and LUPS are depicted as thin horizontal lines at the respective positions in the DOS. Symbolic representations of the subsequent enhancement of the systems are depicted above the diagrams.

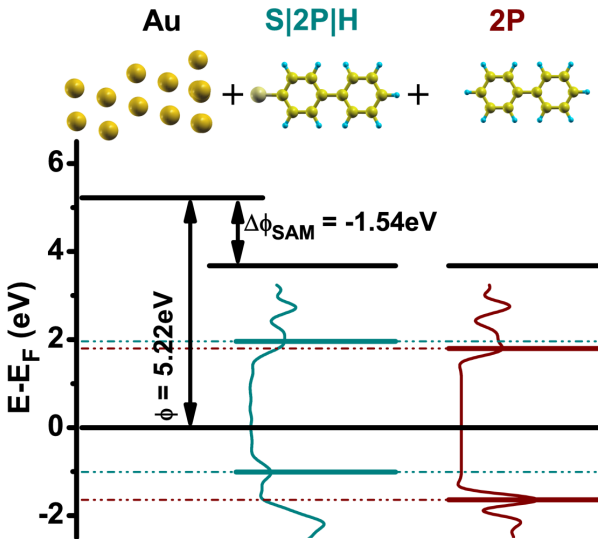

(e) (**5**): Au|S|2P|H||2P

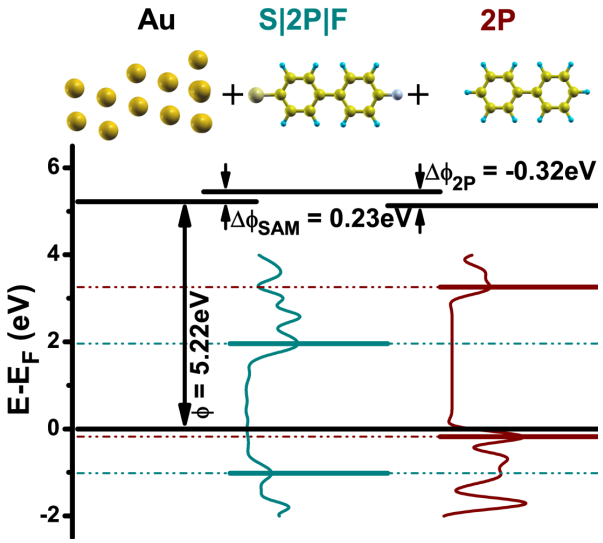

(f) (**6**): Au|S|2P|F||2P

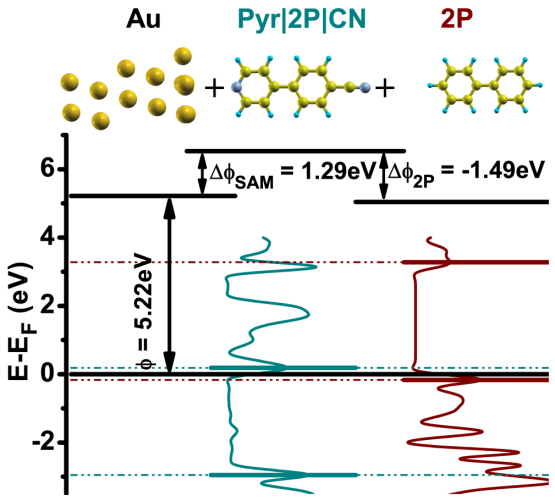

(g) (**7**): Au|Pyr|2P|CN||2P

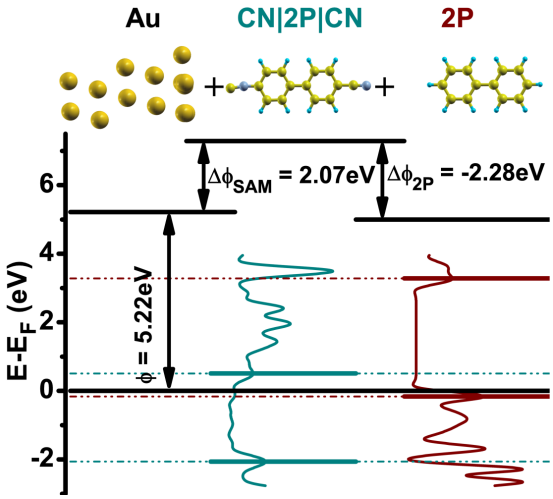

(h) (**8**): Au|CN|2P|CN||2P

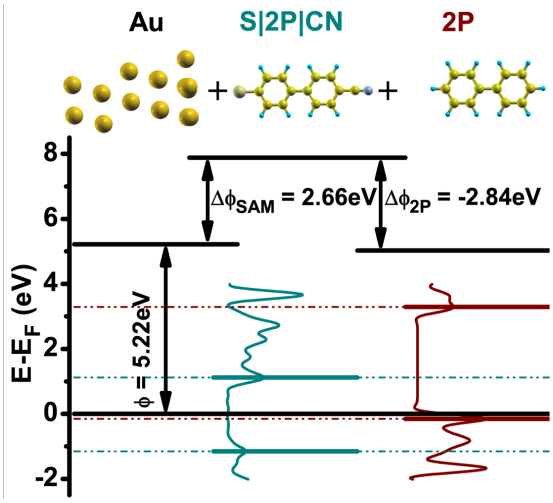

(i) (**9**): Au|S|2P|CN||2P

Figure 5.6: (2nd part).

Table 5.1: The work function modification $\Delta\Phi_{2P}$, ΔE^{SAM}_{HOPS}, ΔE^{SAM}_{LUPS}; ΔE^{2P}_{HOPS} and ΔE^{2P}_{LUPS} which are a measure for the injection barriers between the metal Fermi level and the biphenyl HOPS and LUPS, ionization potential $IP_{2P,c}$ and electron affinity $EA_{2P,c}$ of the 2P in contact with the metal|SAM system, and the band gap of the contacted 2P; all quantities in units of eV. The numbers in the 2nd column sort the systems by ascending $\Delta\Phi_{SAM}$. $\Phi_{Au(111)}$ as calculated from Eqns. (2.13) is listed in the last column (both equations evaluate to the same results).

system	No.	$\Delta\Phi_{2P}$	ΔE^{SAM}_{HOPS}	ΔE^{SAM}_{LUPS}	ΔE^{2P}_{HOPS}	ΔE^{2P}_{LUPS}	$IP_{2P,c}$	$EA_{2P,c}$	Gap	$\Phi_{Au(111)}$
Au|Pyr|2P|NH_2||2P	1	0.79	-2.81	0.28	3.22	0.23	5.38	1.93	3.45	5.23
Au|Pyr|2P|H||2P	2	-0.06	-3.36	0.22	3.18	0.27	5.29	1.84	3.45	5.22
Au|CN|2P|H||2P	3	-0.01	-1.93	0.62	2.18	1.27	5.29	1.84	3.45	5.24
Au|S|1P|H||2P	4	0.00	-1.09	2.54	1.65	1.80	5.30	1.85	3.45	5.19
Au|S|2P|H||2P	5	0.00	-1.02	1.96	1.64	1.81	5.30	1.85	3.45	5.20
Au|S|2P|F||2P	6	-0.32	-1.02	1.96	0.19	3.26	5.29	1.84	3.45	5.19
Au|Pyr|2P|CN||2P	7	-1.49	-2.95	0.19	0.17	3.28	5.21	1.76	3.45	5.24
Au|CN|2P|CN||2P	8	-2.28	-2.06	0.51	0.16	3.29	5.18	1.73	3.45	5.23
Au|S|2P|CN||2P	9	-2.84	-1.14	1.14	0.16	3.29	5.17	1.72	3.45	5.19

positions in the DOS[b].

As expected, the vacuum levels of the systems Au|Pyr|2P|NH_2 and 2P do not align (Fig. 5.6a). Instead, an additional work function modification $\Delta\Phi_{2P}$ arises which counteracts $\Delta\Phi_{SAM}$. This shift amounts to a value (0.79 eV) that is necessary to prevent the biphenyl LUPS from being below E_F (LUPS level pinning).

Disregarding the shift by −0.06 eV (Fig. 5.6b) for the moment[c], the vacuum levels do indeed align in systems (**2**)-(**5**), as expected (Fig. 5.6b - 5.6e). This allows for a direct control of the injection barriers in those systems: the more negative $\Delta\Phi_{SAM}$ is, the more the biphenyl LUPS approaches E_F, while the distance between E_F and biphenyl HOPS increases.

Like in system (**1**), a counteracting work function modification $\Delta\Phi_{2P}$ is found in the remaining four systems (Fig. 5.6f - 5.6i). $\Delta\Phi_{2P}$ is negative in those systems since it shifts the 2P energy levels downwards so that the biphenyl HOPS is not located above the metal Fermi level. At least at first glimpse (for a detailed discussion, see below), the relative position of the HOPS with respect to E_F becomes independent of $\Delta\Phi_{SAM}$, in contrast to the situation in systems (**2**)-(**5**): the injection barriers are no longer controlled by $\Delta\Phi_{SAM}$.

The energy level alignment for the various systems is summarized numerically in Tab. 5.1. In analogy to the discussion in the previous chapter, one can easily construct equations for the injection barriers (compare Sec. 2.4.2):

$$\begin{aligned} \Delta E^{2P}_{HOPS} &= -(\Phi_{Au(111)} + \Delta\Phi_{SAM} + \Delta\Phi_{2P} - IP_{2P,c}) \quad , \\ \Delta E^{2P}_{LUPS} &= \Phi_{Au(111)} + \Delta\Phi_{SAM} + \Delta\Phi_{2P} - EA_{2P,c} \quad . \end{aligned} \qquad [2.13]$$

According to Eqn. (2.12), the work function modification upon addition of the 2P layer equals the interface dipole (ID) due to charge rearrangements upon addition of the layer:

$$\Delta\Phi_{2P} = ID \quad . \qquad [2.12]$$

$IP_{2P,c}$ and $EA_{2P,c}$ stand for the IP and EA of this prototypical organic semiconductor. The indices "c" are used to account for changes of those quantities that may arise upon ***c***ontact with the metal|SAM system. Since all of the other quantities were obtained in the analysis of the calculations, $\Phi_{Au(111)}$ can be calculated using Eqns (2.13). This way two values $\Phi^{HOPS}_{Au(111)}$ and $\Phi^{LUPS}_{Au(111)}$ per system are found. Like in the the previous chapter, both equal; the values are tabulated in Tab. 5.1. Again, the minor deviations from the correct value of 5.20 eV for the unrelaxed gold surface is the sum of two errors (compare Sec. 4.3):

(i) the inexactness immanent in the graphical extraction of the position of energy levels from the DOS and

(ii) the shift in E_F due to the extension of the systems.

Anyhow, increasing the size of the metal slab is a prohibitive task because of the increase of computation time that goes along with that. Further, it is to emphasize that the interest of this study on the energy level alignment lies in the *changes* of energy values instead of their absolute magnitude. The change in the absolute value of E_F due to the addition of

[b] The respective peak maxima were used to assign single energy values to the peaks of finite energetic width.

[c] An explanation for this unexpected shift is available and will be given in the next section (Sec. 5.4). The shift by −0.01 eV in system (**3**) does not obfuscate the picture drawn here because of its almost vanishing magnitude.

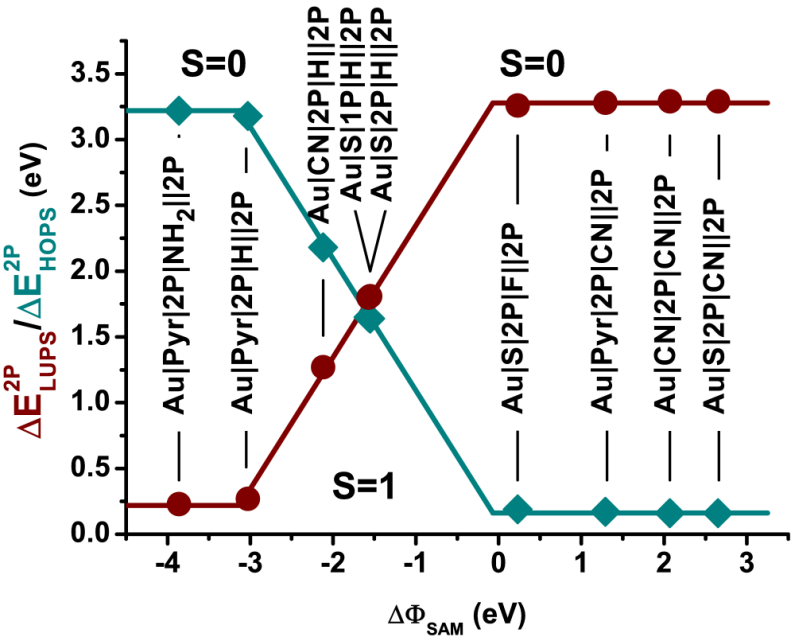

Figure 5.7: $\Delta E^{2P}_{LUPS} := (E^{2P}_{LUPS} - E_F)$ and $\Delta E^{2P}_{HOPS} := (E_F - E^{2P}_{HOPS})$, which measure the electron injection barrier and the hole injection barrier for the nine investigated systems. The lines serve as guide to the eye.

molecules to the metal slab is mainly responsible for the slightly differing values of $\Phi_{Au(111)}$. However, it is not expected to effect results on work function *modifications*.

To characterize different energy level alignment configurations, a *slope parameter* S can be defined [4, 5, 2]:

$$S = -\frac{d(E_F - E_{HOPS})}{d(\Delta\Phi_{SAM})} \quad . \tag{5.1}$$

The dependence of ΔE^{2P}_{LUPS} and ΔE^{2P}_{HOPS}, which measure the electron injection barrier (EIB) and the hole injection barrier (HIB), on $\Delta\Phi_{SAM}$ is depicted in Fig. 5.7 for the nine systems (see Tab. 5.1). They are directly controlled by $\Delta\Phi_{SAM}$ only in the middle region of the plot ($S = 1$). The injection barriers have the largest (smallest) values at the left and right side of the plot and become essentially independent of $\Delta\Phi_{SAM}$ ($S = 0$ in those regions). Hence, the slope parameter distinguishes vacuum level alignment from Fermi level pinning.

The magnitude of the maximal and minimal injection barrier depends on the size of the band gap of the OSC. In case of 2P, the gap amounts to 3.45 eV (see Fig. 5.2).[d] However, according to Fig. 5.7 and Tab. 5.1, the largest (smallest) injection barriers amount to approx. 3.25 eV and 0.20 eV. The difference of approx. 0.2 eV relative to the expected energetic distances of 3.45 eV and 0.00 eV in the pinning regions of the plot essentially stems from the applied broadening of 0.2 eV: as described in Sec. 3.5, the DOS is artificially broadened in the numerical calculations to improve convergence. When it comes to pinning of a biphenyl level, the distance between the peak maximum of the pinned level and E_F is determined by the broadening. To illustrate this effect, the DOS projected onto the biphenyl region of system (**9**) around E_F is plotted in Fig. 5.8 for different broadening

[d] Because DFT calculations underestimate the band gap of semiconductors, this value is too small. However, the band gap of oligophenylenes decreases with increasing number n of phenyl rings according to the "$1/n$ law" [55, 56]. 2P may therefore be understood as a substitute for an oligophenylene with a larger number of rings.

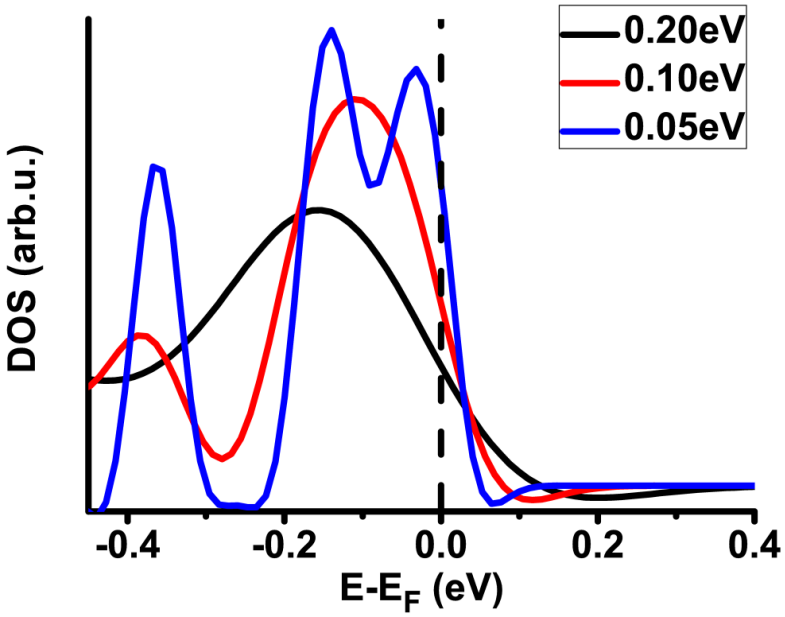

Figure 5.8: DOS projected onto the 2P near E_F in system (**9**) for broadening values of 0.20, 0.10 and 0.05 eV. The distance between the biphenyl HOPS peak maximum and E_F is determined by the applied broadening.

values. The distance between the peak maximum and E_F is directly determined by the broadening width.

A comparison of ΔE^{2P}_{HOPS}-values for different pinning cases shows, that this energetic distance is also determined by the magnitude of the ID ($\Delta\Phi_{2P}$). Going from system (**6**) to (**9**) in Tab. 5.1, ΔE^{2P}_{HOPS} is reduced from 0.19 eV (**6**) to 0.16 eV (**9**). In other words, the HOPS peak maximum approaches E_F with increasing ID. This effect is depicted in Fig. 5.9, which shows the DOS projected onto the 2P near E_F for those systems.

A closer look at Tab. 5.1 also shows, that the ionization potential and electron affinity $IP_{2P,c}$ and $EA_{2P,c}$ of the *contacted* biphenyl monolayer keep their original values only in the vacuum level alignment regime. In other words, upon contact only the vacuum level is shifted by exactly $\Delta\Phi_{2P}$ in the pinning regimes; the energy levels of the biphenyl monolayer are shifted by a slightly different value. This effect is illustrated in Fig. 5.10, where the difference between the IPs and EAs of the contacted ("*2P,c*") and isolated ("*2P*") monolayer of 2P are depicted for the nine systems. Notably, all deviations are identical for IPs and EAs. This corresponds to a constant band gap of the 2P, see Tab. 5.1. If not as controlled as for IP and EA of the 2P layer, an equivalent trend is found for the quantities ΔE^{SAM}_{HOPS} and ΔE^{SAM}_{LUPS} (see Tab. 5.1 & Fig. 5.11). An explanation of this phenomenon will be given in the next section, where the microscopic effects leading to Fermi level pinning are discussed in detail.

5.4 Metal|SAM||OSC: $\Delta\rho$, Q and E

To get a deeper insight into the investigated systems and to understand which processes cause Fermi level pinning, an analysis similar to the analysis of the metal|SAM systems in the last chapter can be performed. First, one can take a look at the charge rearrangements upon addition of 2P,

$$\Delta\rho = \rho_{metal|SAM||2P} - (\rho_{metal|SAM} + \rho_{2P}) \quad . \tag{5.2}$$

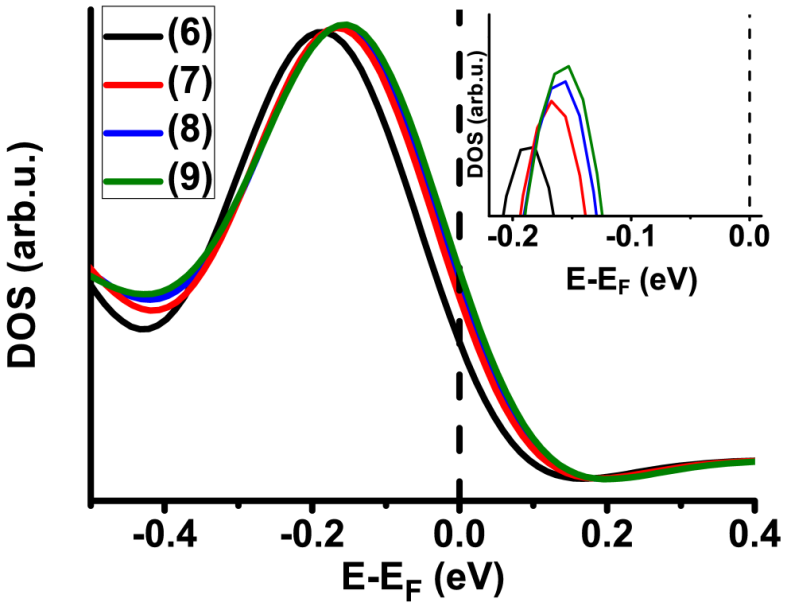

Figure 5.9: DOS projected onto the 2P near E_F in systems (**6**)-(**9**). The greater $\Delta\Phi_{2P}$ (the higher the system number), the smaller ΔE^{2P}_{HOPS}. The inset shows a zoom of the peak maxima.

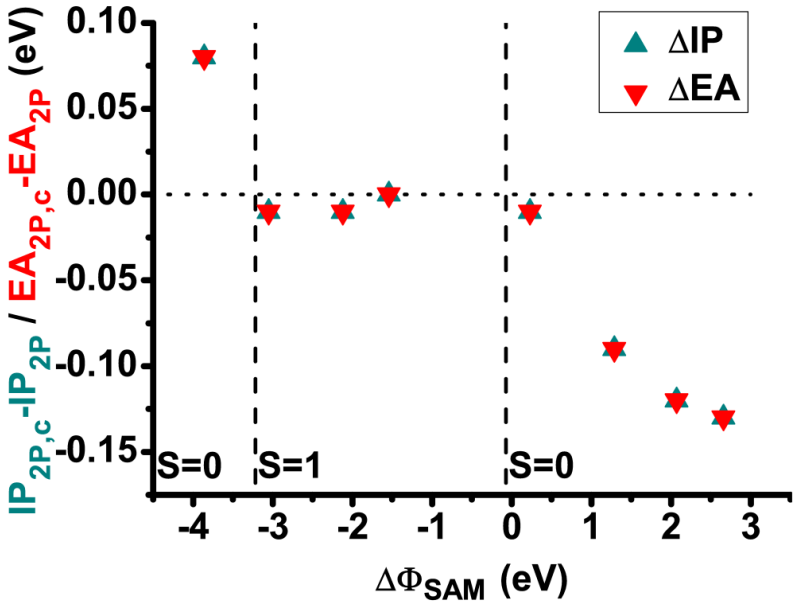

Figure 5.10: Difference between the ionization potential (electron affinity) of the 2P in contact with the metal|SAM slab $IP_{2P,c}$ ($EA_{2P,c}$) and IP_{2P} (EA_{2P}) of the isolated 2P monolayer. Nonzero differences are found in the pinning regimes. They equal in magnitude for both quantities, IP and EA.

Again, $\Delta\rho$ is a three dimensional quantity. For the reasons described in the previous chapter, primarily the quantity $\Delta\rho(z)$, being $\Delta\rho$ integrated over the plane parallel to the substrate surface ($\Delta\rho(z) = \iint \Delta\rho(x,y,z)dxdy$) in units of $-e/\text{Å}$ is discussed. Here, z is the Cartesian coordinate directed perpendicular to the metal surface. The integral over $\Delta\rho(z)$, $Q(z)$ and the solution of the one dimensional Poisson equation (2.5) are the other quantities of interest. Because the biphenyl layer is not chemically adsorbed on the SAM - as indicated by the "||" in the notation -, the name bond dipole appears to be inadequate

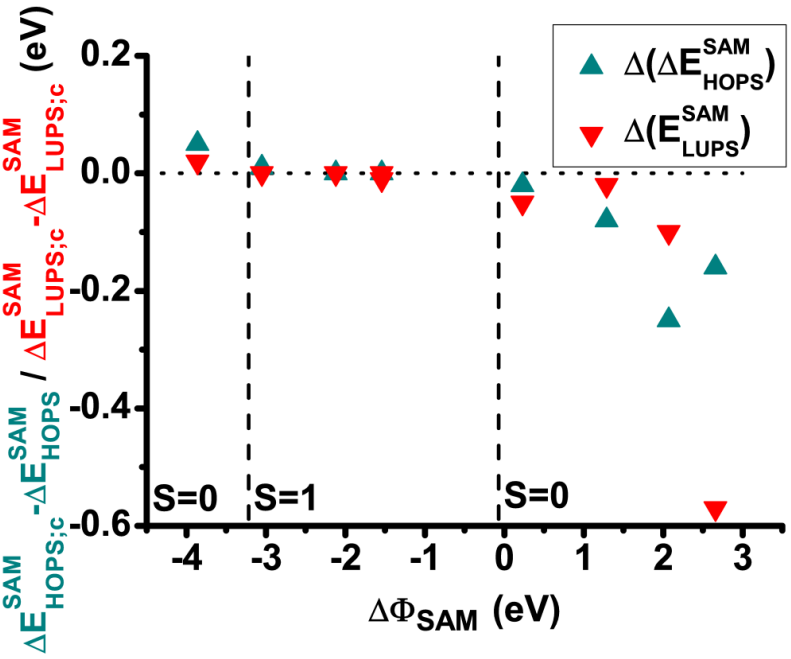

Figure 5.11: Difference between $\Delta E^{\mathrm{SAM}}_{\mathrm{HOPS}}$ (and $\Delta E^{\mathrm{SAM}}_{\mathrm{LUPS}}$) after and before contact with the 2P monolayer.

here. Instead, the net effect of $\Delta\rho$ on $E(z)$ is merely denoted as the interface dipole (ID) here (compare Sec. 2.4.2).

In the following, those three quantities $\Delta\rho(z)$, $Q(z)$ and $E(z)$ are discussed for four out of the nine systems:

(i) a vacuum level alignment situation, system (**5**);
(ii) the HOPS pinning cases with minimal (system (**6**)) and
(iii) maximal $\Delta\Phi_{2\mathrm{P}}$ (system (**9**)) and
(iv) the only LUPS pinning situation, system (**1**).

A comparison of those representative systems allows an analysis of the mechanism that causes $\Delta\Phi_{2\mathrm{P}}$.

To start with the simplest case, vacuum level alignment (system (**5**)) is discussed first. The three quantities described above are depicted in the leftmost panel of Fig. 5.12. Reminiscent of Pauli push back [1, 57] at metal/organic interfaces, electron density is pushed away from the interfacial region (blue area) and accumulates within the S|2P|H SAM and the 2P. Those charge rearrangements are almost completely symmetric with respect to the interface, so that no net charge transfer across the interface takes place. This is confirmed by the Q-plot for this system. The antisymmetry of Q corresponds to the symmetry of $\Delta\rho$. Q crosses the zero line at the interface, expressing that no charge is transferred from regions above (i.e., the biphenyl region) to below (i.e., the metal|SAM region) the interface; the charge rearrangements are local within the layers. According to this symmetry, the overall effect of $\Delta\rho$ on the electrostatic energy of an electron, the ID, is essentially zero (disregarding the small negative dip directly at the interface).[e] This is consistent with the vanishing $\Delta\Phi_{2\mathrm{P}}$ in system (**5**).

In contrast, in the pinning cases the significant $\Delta\Phi_{2\mathrm{P}}$ must be caused by some charge transfer. Intuitively, one might expect that this charge transfer should be between the

[e] The small net ID is attributed to slight asymmetries at the SAM||2P interface.

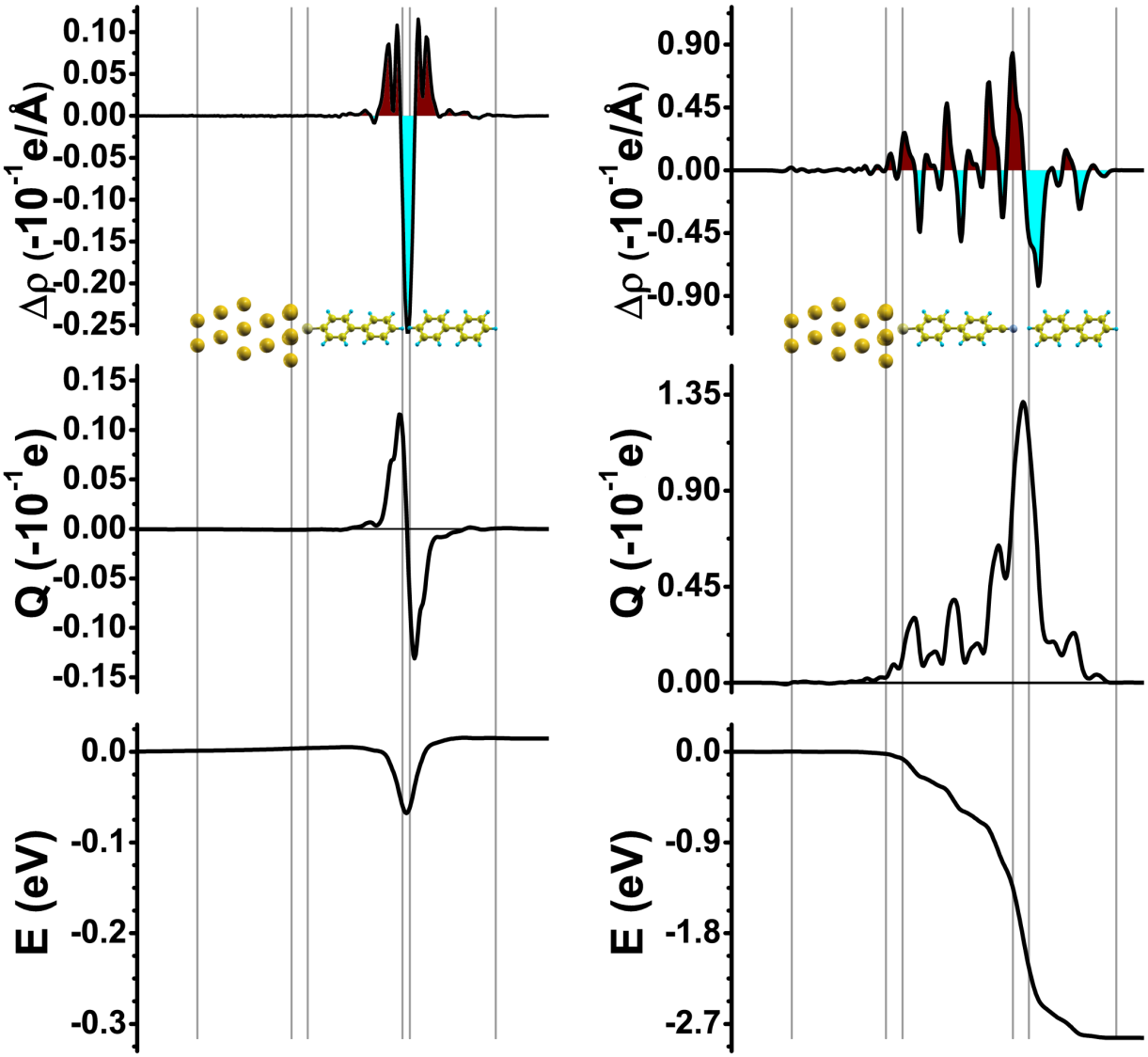

(a) (**6**): Au|S|2P|H||2P (b) (**8**): Au|S|2P|CN||2P

Figure 5.12: (1st part) The top panels show the charge rearrangements $\Delta\rho$ upon addition of 2P, integrated over the plane parallel to the gold surface (units: $-e/\text{Å}$) for systems (**5**), (**9**), (**6**) and (**1**) ((a) to (d)). The red areas indicate electron density accumulation and the blue areas electron density depletion. Below, the accumulated charge transfer $Q(z)$ (units: $-e$) is depicted. Additionally, the effect of $\Delta\rho$ on the electrostatic energy of an electron, $E(z)$, is shown in eV. The plots for system (**9**) differ by a factor nine [three] in scale from the plots for system (**6**) [(**1**)].

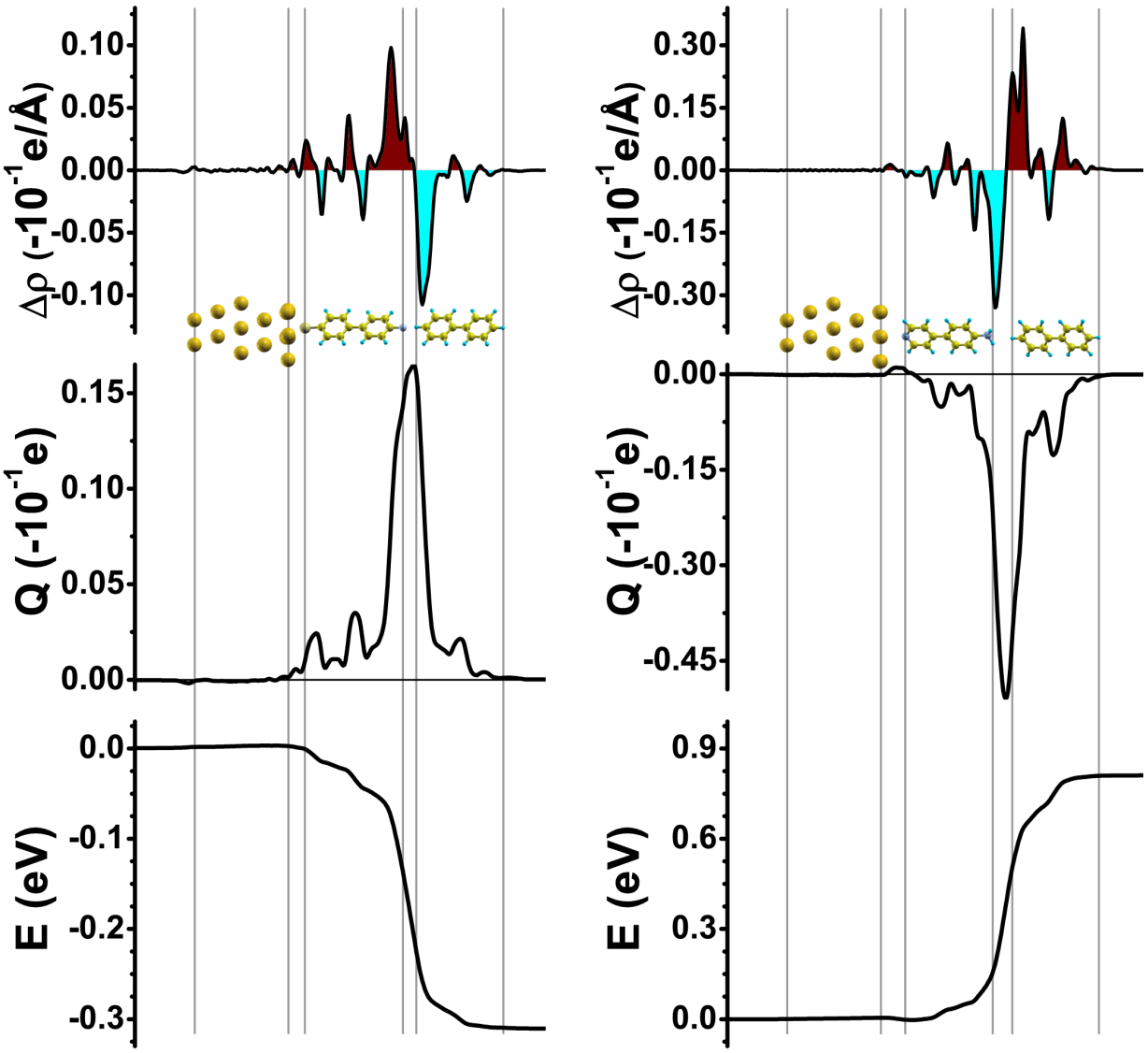

(c) (**7**): Au|S|2P|F||2P

(d) (**1**): Au|Pyr|2P|NH_2||2P

Figure 5.12: (2^{nd} part) The plots for system (**9**) differ by a factor nine [three] in scale from the plots for system (**6**) [(**1**)].

OSC layer and the metal, as it prevents the occupied (unoccupied) states of the 2P layer from lying above (below) the *metal* Fermi level in thermodynamic equilibrium. Considering the large charge transfer distance, the absolute magnitude of the transferred charge could be comparably small to yield the necessary shift of the levels. Nothing like that is, however, observed here. The situation for the HOPS pinning case with the largest $\Delta\Phi_{2P}$ (Au|S|2P|CN||2P; system (**9**)) is depicted in panel (b) of Fig. 5.12. There is no long range charge transfer from 2P to the gold. Instead two other effects give rise to $\Delta\Phi_{2P}$: Significant electron transfer occurs in the SAM||2P interface region from the 2P layer to the SAM (pronounced peaks in $\Delta\rho$ and Q and corresponding sharp drop in E); additionally, the SAM is polarized, i.e., charge is redistributed within the SAM giving rise to a series of dipoles (see $\Delta\rho$ plot). The long range transfer within the SAM remains relatively small (see Q plot). As a net effect, the potential energy drops by $-2.84\,\mathrm{eV}$, corresponding to the $\Delta\Phi_{2P}$ of system (**9**) (see E plot). A similar situation is observed for system (**6**), Au|S|2P|F||2P (Fig. 5.12c; note the different scales compared to Fig. 5.12b). It shows $\Delta\Phi_{2P}$ amounting to $-0.32\,\mathrm{eV}$, which is about one ninth of the value for system (**9**). Consequently, both the interfacial charge transfer as well as the polarization of the SAM are reduced. Interestingly, the reduction of the latter effect is more pronounced.

The overall situation for LUPS pinning in Au|Pyr|2P|NH2||2P (system (**1**)) is intermediate between those two cases ($\Delta\Phi_{2P} = +0.79\,\mathrm{eV}$) with the main qualitative difference being a reversal of the sign of the charge rearrangements, consistent with a reversal of the sign of $\Delta\Phi_{2P}$.

The observation that a qualitatively similar behavior is observed in all three displayed pinning cases and that $\Delta\rho$ extends over the whole SAM instead of just across the interfacial region supports the notion that the observed charge rearrangements are characteristic of Fermi level pinning for OSCs on SAM covered metals rather than a mere consequence of some type of surface reaction between the head groups of the SAM and the 2P layer.

Having this tool of analysis at hand, it is now possible to understand the unexpected $\Delta\Phi_{2P}$ which was found in system (**2**), Fig. 5.6b. Altough system (**2**) is in the vicinity of LUPS pinning (compare Fig 5.7 and Tabs. 4.1 & 4.2), this effect can be definitely excluded here. Here, $\Delta\Phi_{2P}$ does not counteract $\Delta\Phi_{SAM}$ like in the pinning cases, but *supports* $\Delta\Phi_{SAM}$, i.e., they have the same sign. The reason for this effect lies in a result presented in Ref. [21, Fig. 3]. Its relevant detail is reproduced in Fig. 5.13. Upon adsorption of the Pyr|2P|H SAM on Au(111), the SAM LUPS is pinned at E_F, similar to the Pyr|2P|CN SAM discussed in the previous chapter. As a consequence, a series of dipoles is induced in the SAM (the SAM is polarized), see dashed lines in Fig. 5.13. They reduce the bond dipole to a value which prevents the SAM LUPS to lie below E_F (see Eqn. (2.3) and Tabs. 4.1 & 4.2). If the 2P monolayer is placed on top of the SAM, those polarization effects are found to extend into it and give rise to an additional change of the work function. This extension of the polarization into the subsequent monolayer is best seen when both, the SAM and the 2P, are simultaneously added to the metal. Then, the charge rearrangements are calculated according to

$$\Delta\rho = \rho_{\mathrm{metal|SAM||2P}} - (\rho_{\mathrm{metal}} + \rho_{\mathrm{SAM||2P}}) \quad . \tag{5.3}$$

Fig. 5.14 shows a comparison of $\Delta\rho$ upon addition of the SAM (black solid line) and upon addition of SAM and 2P simultaneously (red dashed line). In the presence of 2P, the

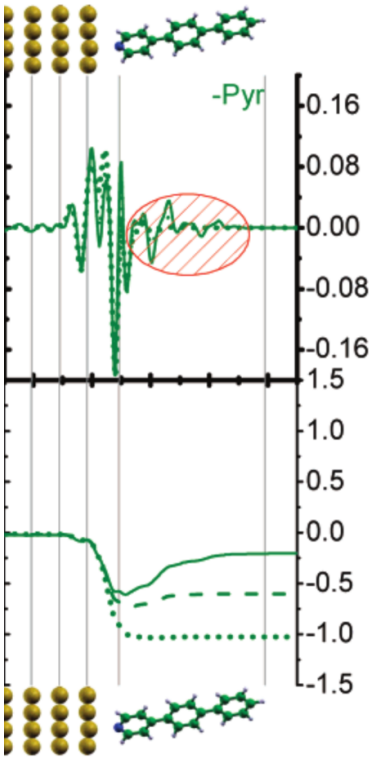

Figure 5.13: Charge rearrangements and their effect on the electron potential energy, $E(z)$, for the systems Au|Pyr|xP|H, with $x = 1$ (dotted), $x = 2$ (dashed) and $x = 3$ (solid), taken from Ref. [21].

rearrangements are comparable to those in Fig. 5.13, with three rings present ($x = 3$; solid line).

The second observed phenomenon to be discussed here is the decrease (increase) of the biphenyl IP and EA in the HOPS (LUPS) pinning regime (Fig. 5.10). A look at the bottom panels of Figs. 5.12b,c&d shows, that the steps in the electrostatic energy are not sudden at the interface, but extend into the SAM and 2P layer [17]. This effect is illustrated in Fig. 5.15. It shows the plane averaged electron potential energy across a 2P monolayer (black solid line) and its modification (red solid line) due to the effect of charge rearrangements on the electrostatic energy E (black dashed line). The caused energetic asymmetry shifts the 2P energy levels upwards with respect to the vacuum level $\mathrm{VL}_{\mathrm{right}}$ that is used to define $\mathrm{IP}_{\mathrm{2P,c}}$ and $\mathrm{IP}_{\mathrm{2P,c}}$ (see Sec. 2.4.2).

Concerning $\Delta E^{\mathrm{SAM}}_{\mathrm{HOPS}}$ and $\Delta E^{\mathrm{SAM}}_{\mathrm{LUPS}}$, the same explanation can be given. Here, one has to take into account that also the SAM is affected by the finite extension of E. So far, the less controlled way in which those quantities are modified remains unexplained.

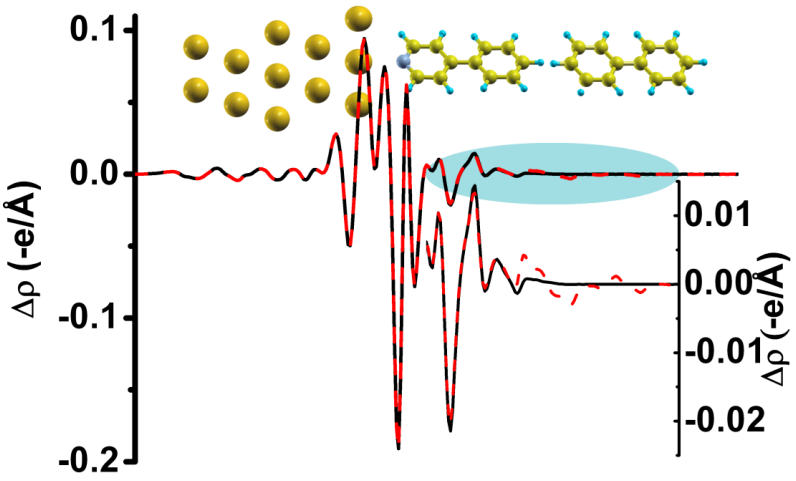

Figure 5.14: The charge rearrangements $\Delta\rho$ upon adsorption of the Pyr|2P|H SAM on a Au(111) surface (black line) and upon connecting both, SAM and 2P, simultaneously with the gold (dashed red line). The inset shows a zoom of the shaded region. A schematic representation of the system serves as guide to the eye.

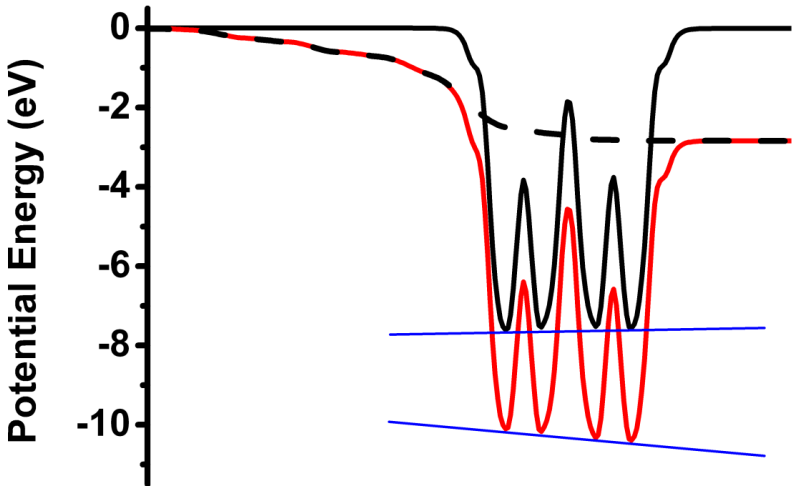

Figure 5.15: Plane averaged electron potential energy across the 2P monolayer (black curve), $E(z)$ upon contact with system (**9**) (black, dashed curve) and their sum (red curve). The blue lines hint at the energetic asymmetry in the monolayer caused by the finite extension of $E(z)$. A negative (positive) BD implies an effective downward (upward) shift of the energy levels with respect to the right vacuum energy level.

6 Geometry relaxations in internal coordinates

Introduction. A geometry relaxation is a calculation in which the ionic coordinates of a system of N atoms are optimized with respect to the total energy of the system. The calculation of the total energy in DFT is - especially with growing number of atoms - a computationally expensive task. Hence, the fewer evaluations of the DFT ground state energy a certain optimization strategy needs, the better. The optimization problem would be completely solved if the total energy hypersurface $E = E(\mathbf{r}_1, \ldots, \mathbf{r}_N)$ was known. Such comprehensive knowledge about an atomic system can in general not be reached. Starting from a certain configuration of atoms, a more realistic goal is to search for a *local* minimum of the total energy.

A variety of different optimization strategies exists. Many of them start with the calculation of the DFT total energy for a certain configuration of ionic positions. A guess of the local shape of E follows. A sensible trial geometry is then proposed on the basis of this approximate local energy hypersurface. The DFT energy is again evaluated at the new atomic positions. This procedure is repeated until a chosen convergence criterion is

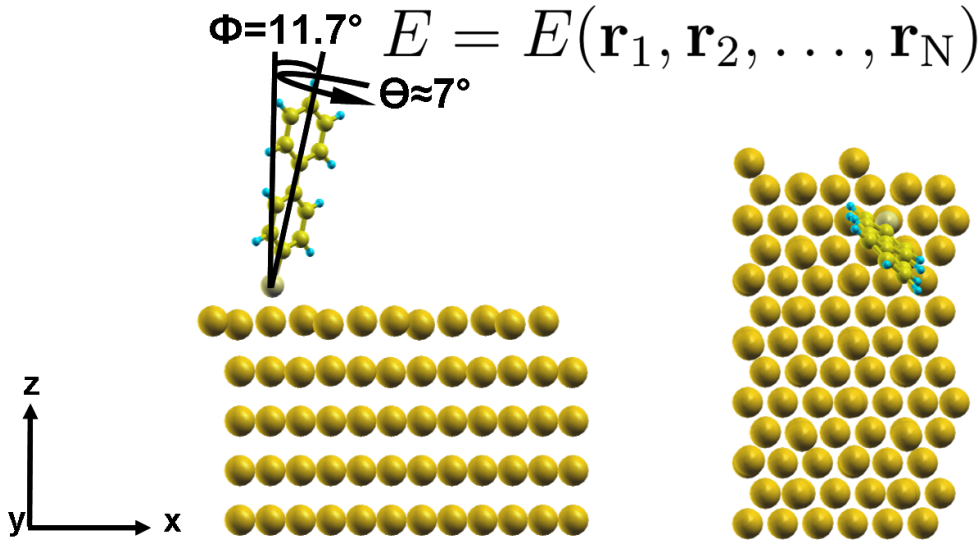

Figure 6.1: Unrelaxed system Au|S|2P|H at a coverage of $\Theta = 1/8$ (surface unit cell: $p(6 \times 2\sqrt{3})$), side (left panel) and top view (right panel). The tilt angle of the SAM molecule with respect to the surface normal Φ amounts to 11.7°, the inter-ring twist angle Θ to 7°. This geometry is the starting point for the following calculations.

reached. For this purpose, a certain change in the total energy may be used. More conveniently, a geometry is regarded as converged as soon the maximum force on an ion falls below a certain value.

Motivation. In our group, an interesting trend was observed concerning the results of geometry relaxation calculations of SAMs on surfaces performed with VASP. Two degrees of freedom are hardly modified in comparison to the input geometry of the calculation provided by the user. The first concerns primarily oligophenyl derivates: it is the twist angle between the rings. The tilt angle of the molecules with respect to the metal surface normal is the other one. Those degrees of freedom are especially interesting at a coverage low enough to provide sufficient space for them to be varied.

It may be an artifitial result of the internal VASP optimizer that twist and tilt angle hardly change during optimizations. VASP performs the optimization process in Cartesian coordinates. In geometry optimizations of molecules, so-called *internal coordinates* (see below) have proven to perform significantly better than Cartesian coordinates [58, 59, 60, 61]. Therefore, it is reasonable to employ such a set of internal coordinates in metal|SAM optimizations, too. One can expect a better, or at least more efficient description of the molecular part of the system using internal coordinates. An internal coordinate optimizer for solid state total energy codes is implemented in the free software GADGET [22]. Tomáš Bučko, one of its authors, was very helpful in adjusting the software to our purposes. I am deeply thankful for his willingness to support me and answer my frequent questions.

The system. A biphenylthiol SAM on gold (Au|S|2P|H) was used as prototypical example to benchmark the effect of the used coordinates on the geometry optimization. The calculation was performed at a coverage of $\Theta = 1/8$, which is obtained by removing seven eighth of the SAM molecules in comparison to the densly packed monolayers investigated so far ($\Theta = 1$). One ends up with a $p(6 \times 2\sqrt{3})$ surface unit cell containing one molecule (see Fig. 6.1). Using a cell height of ≈ 45Å, the vacuum gap amounts to > 20Å as usual.

Methodology. A 2×4 k-point mesh was used. The large size of the unit cell made the usually applied convergence criterion unfeasible. Instead of demanding the maximum force to be smaller than 0.01 eV/Å a less strict requirement was employed. In the preliminary results presented here, GADGET calculations did converge to forces smaller than 0.0515 eV/Å, while native VASP optimizations converged to forces smaller than 0.0272 eV/Å. Although this discrepancy complicates a comparison of the resulting geometries, trends can be clearly identified in the calculations on the present model system. Currently running continuation calculations not only support the picture drawn below, but hint to even more conclusive results. The following tags were set in the GADGET input file `INPDAT`:

- `ECRITER = 1e-5`: convergence criterion for the energy in atomic units (Hartree)
- `GCRITER = 0.001`: convergence criterion for the forces in atomic units (0.001 Hartee per Bohr radius correspond to 0.051546392 eV/Å)

- `SCRITER = 5.02`: convergence criterion for the change of any internal coorinate; effectively switched off by setting it to 5.02
- `CART = 0`: optimize in delocalized internal coordinates (Cartesian coordinates, if set to `1`)
- `ASCALE = 1.3`: scaling factor for automatic coordinate identification [62]. Each atom A of a fragment has at least one neighbor B at a maximum distance of $(r_A + r_B)$*`ASCALE`.
- `BSCALE = 1.6`: like `ASCALE`; `ASCALE`*`BSCALE` is used for atoms belonging to different fragments (compare `FRAGCOORD`)
- `CSCALE = 1.3`: obsolete tag
- `FRAGCOORD = 0`: Cartesian coordinates are used for all fragments but the largest. Only one fragment is present in the current calculcations; see `inputer.py` for values `1`, `2` and `3`
- `RELAX = 0`: relaxation of atomic positions only (`0`); `1`: relaxation of atomic positions and lattice parameters
- `HESSIAN = 3`: Hessian matrix initialized according to Fischer's model [63]; see file `inputer.py` for values `0`, `1` and `2`
- `HUPDATE = 1`: use the Broyden-Fletcher-Goldfarb-Shanno (BGFS) update formula for the Hessian matrix (see Ref. [22])
- `OPTENGINE = 0`: use direct inversion in the iterative subspace (DIIS) optimization engine, see Refs. [22, 64]; `1`: RFO
- `NFREE = 5`: number of history-steps involved in DIIS (see Ref. [22])

An overview over the available tags and their default values is given in the file `inputer.py`.

Before the results are presented, the importance of the chosen set of coordinates on the optimization process is illustrated.

6.1 Impact of the set of coordinates

In Cartesian coordinates, space is described by an arbitrarily chosen point of origin and three orthogonal linear axes which intersect at this origin. The position of an object is defined as a triple of numbers, each denoting the distance of the object from the planes defined by two of the axes. Distances, angles etc. between objects are in general described as nonlinear functions of those coordinates. For example, the bond length r_{12} between two ions 1 and 2 is to be calculated as $r_{12} = \sqrt{\sum_{i=1}^{3}(x_1^i - x_2^i)^2}$. Sets of coordinates can be defined which exclusively use *internal* quantities such as bond lengths (r), angles (Θ), torsions (Φ) etc. instead of Cartesian coordinates. Such *internal coordinates* are illustrated

in Fig 6.2.

In contrast to a Cartesian description, internal coordinates may easily become highly redundant. For N atoms in a unit cell of fixed shape and size, $3N-3$ [43, 22, 65] degrees of freedom exist. This number almost equals the number of Cartesian ionic coordinates ($3N$) necessary to describe the system. No such "natural" restriction of the number of internal coordinates exists, so that usually much more than $3N-3$ internal coordinates can be constructed for a system of N atoms. Handling redundant coordinates is computationally problematic, so that a system of non-redundant internal coordinates is desired. Linear combinations of internal coordinates with this property can be generated [59, 22]. Such "*delocalized internal coordinates*" are used by GADGET.

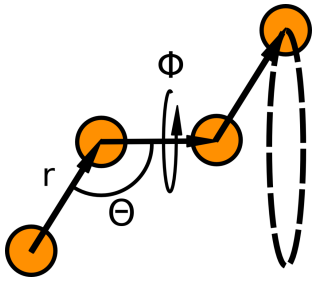

Figure 6.2: Schematic illustration of some internal coordinates: bond length r, angle Θ and dihedral angle (torsion) Φ.

Independent of the coordinate system, the total energy can be expanded in a Taylor series at a certain position $\mathbf{x}$:

$$E(\mathbf{x}+\delta\mathbf{x}) - E(\mathbf{x}) = -\mathbf{f}^t\delta\mathbf{x} + \frac{1}{2}\delta\mathbf{x}^t\mathbf{F}\delta\mathbf{x} + \dots \quad , \tag{6.1}$$

where $\mathbf{f}$ is the force vector, $\mathbf{f} = -dE/d\mathbf{x}$, and the Hessian matrix $\mathbf{F}$ contains the second derivatives of the total energy with respect to the coordinates x_i (the force constants),

$$\mathbf{F} = \begin{pmatrix} \frac{\partial^2 E}{\partial x_1^2} & \frac{\partial^2 E}{\partial x_1 \partial x_2} & \cdots & \frac{\partial^2 E}{\partial x_1 \partial x_{3N}} \\ \frac{\partial^2 E}{\partial x_2 \partial x_1} & \frac{\partial^2 E}{\partial x_2^2} & \cdots & \frac{\partial^2 E}{\partial x_2 \partial x_{3N}} \\ \vdots & \vdots & \ddots & \vdots \\ \frac{\partial^2 E}{\partial x_{3N} \partial x_1} & \frac{\partial^2 E}{\partial x_{3N} \partial x_2} & \cdots & \frac{\partial^2 E}{\partial x_{3N}^2} \end{pmatrix} \quad . \tag{6.2}$$

(6.3)

Many optimizers - including GADGET - make use of such a truncated (at 2nd degree) Taylor expansion. This way, the energy hypersurface is locally approximated by a harmonic potential; cubic and *higher order couplings* between the coordinates are neglected [60, 66]. Frequently, also the Hessian matrix is not calculated exactly to save computation time. GADGET, e.g., performs approximate updates of an initial guess (see Ref. [22] for details). As Refs. [60, 66] point out, the unconsidered higher order couplings can be reduced by choosing a set of proper coordinates. Especially for "bad" initial geometries, i.e., geometries far from equilibrium, higher order couplings can hamper convergence or may even cause divergence. Different sets of coordinates become equivalent only near equilibrium. For molecular systems, internal coordinates are in general superior to Cartesian coordinates with respect to the avoidance of higher order couplings since they describe molecular degrees of freedom more properly.

However, Ref. [22] accentuates that the internal coordinates used in this study are superior mainly regarding the speed of convergence. This is attributed to the ease in which a reasonable initial Hessian matrix can be proposed in internal coordinates. A simple diagonal matrix with fixed values for bonds, angles and torsions works well already [22, 67]. To benchmark GADGET, a series of thoughtfully chosen bulk calculations was performed in the study documented in Ref. [22]. In a comparison between the obtained results with the ones of a Cartesian optimizer implemented in VASP (conjugate gradient), identical results were found within the precision of the calculations.

The prototypical system investigated here, a SAM covered metal surface, differs in many ways from the bulk materials used in the aforementioned study. In contrast to the bulk calculations, an important dependence of the resulting geometry on the applied system of coordinates was found.

6.2 Results

6.2.1 Geometry

The input geometry (Fig. 6.1) shows an inter-ring twist angle of $\Theta_{\text{start}} \approx 7°$ and a tilt angle of $\Phi_{\text{start}} \approx 11.7°$.

Determining twist and tilt angles

Twist angle. The inter-ring twist angle was determined graphically by rotating the upper ring until the molecule appeared as a flat object. The rotation axis was defined by the vector connecting the lowermost and the uppermost carbon atom of the upper ring. Reproducibility of the measurements was found to be best when looking at the molecules from the *side* (instead of from the top).

Tilt angle. The tilt angle was determined more accurately, according to the equation

$$\Phi = \cos^{-1}\left(\frac{\mathbf{a}\cdot\mathbf{e}_z}{|\mathbf{a}|\,|\mathbf{e}_z|}\right) = \cos^{-1}\left(\frac{a_z}{|\mathbf{a}|}\right) \quad , \tag{6.4}$$

where the long molecular axis $\mathbf{a}$ is defined as the vector connecting the lowermost and uppermost atom belonging to the molecule (sulfur and hydrogen), and $\mathbf{e}_z$ is the unit vector in z-direction (perpendicular to the surface).

Optimizations

Fig. 6.3 shows the relaxed geometries obtained by a Cartesian coordinate (bluely shaded atoms) and an internal coordinate optimization (golden atoms). Further on, geometries obtained by the (Cartesian) VASP optimizer will be denoted as "VASP geometries", whereas results of internal coordinate relaxations will be referred to as "GADGET geometries".

VASP geometry: The tilt angle was slighty reduced to $\Phi = 11.4°$ and the twist angle changed by only $\approx 1°$. Instead of significantly modifying those degrees of freedom, the whole molecule moved downwards by $< 0.07\,\text{eV/Å}$. In Tab. 6.1, which summarizes the

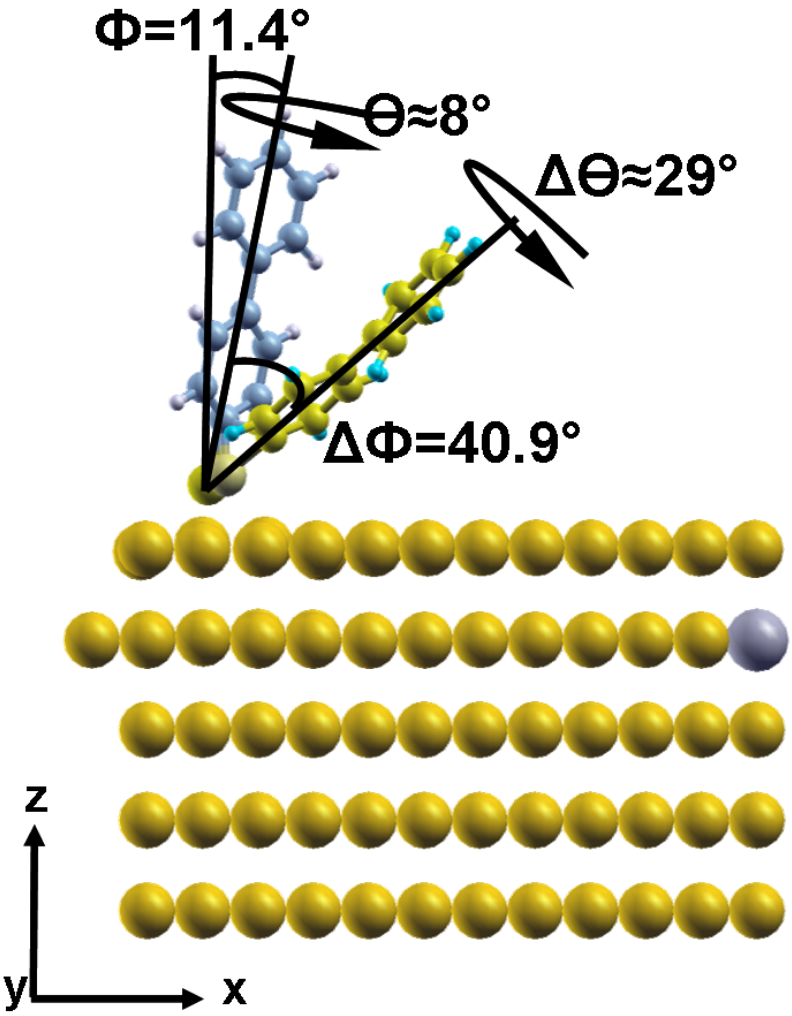

Figure 6.3: The system Au|S|2P|H at a coverage of $\Theta = 1/8$, relaxed in Cartesian (blue) and in internal coordinates (golden). The results differ significantly. The common initial geometry is depicted in Fig. 6.1.

obtained results numerically, the energy of this geometry was set to zero, i.e., the VASP geometry serves as the reference geometry in the following.

GADGET geometry: In internal coordinates, a completely different geometry was found (golden molecule in Fig. 6.3). The twist was increased by 30° to $\Theta \approx 37°$ and the tilt angle Φ by 40.6° to $\Phi = 52.3°$. The energy associated with the converged GADGET geometry is by 0.08 eV lower compared to the energy of the reference geometry.

Tests

To test the GADGET geometry on its stability, two tests were performed. The molecule was rotated by 15° ("***Test 1***") and 30° ("***Test 2***") using the y-axis $(0, 1, 0)$ as rotation axis, the sulfur atom being the center of rotation. This implies initial tilt angles of $\Phi = 65.3°$ and $\Phi = 78.7°$ and energies of +0.04 eV and +1.55 eV compared to the energy of the reference geometry. Starting from those geometries, additional optimizations were performed in Cartesian and internal coordinates, respectively.

Test 1. The results of **Test 1** are shown in Fig. 6.4. Both the tilt and the twist angle did not change at all in the Cartesian optimization (Tab. 6.1). Mainly local reconstructions at

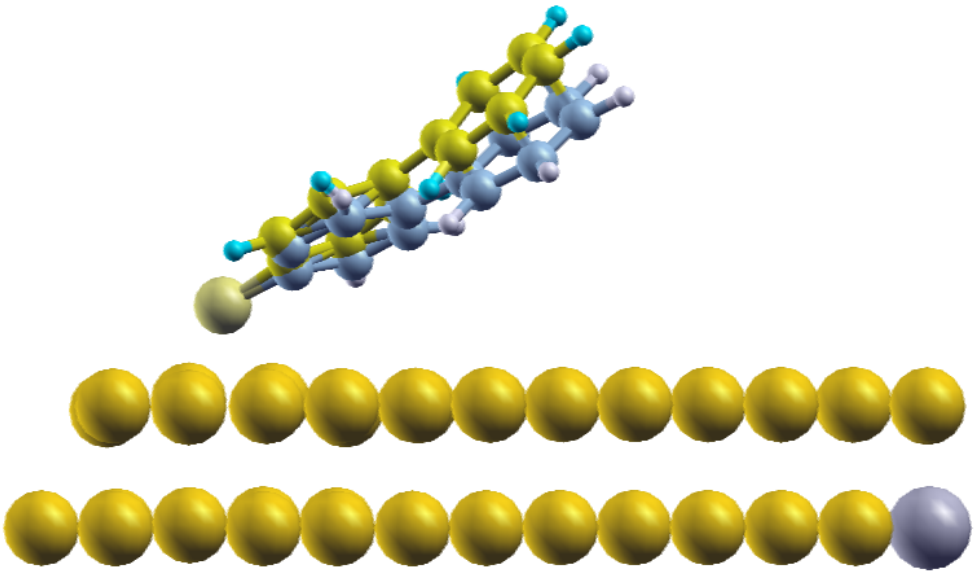

Figure 6.4: **Test 1**: The system Au|S|2P|H at a coverage of $\Theta = 1/8$, relaxed in Cartesian (blue) and in internal coordinates (golden); bottom three Au layers are not shown. Both calculations were started from the GADGET geometry (golden color in Fig. 6.3), rotated by 15° around the y-axis (the sulfur atom being the center of rotation).

the docking group were seen which result in a geometry more favorable than the reference geometry (−0.04 eV).

In contrast, GADGET reduced the molecular inclination by 7.7° (out of 13°; $\Phi = 57.6°$), reaching an energy as low as the energy of the previous GADGET geometry (−0.08 eV).

Test 2. Concerning **Test 2**, a comparison of the initial geometry (golden) with the VASP geometry (blue, Fig. 6.5a) and between the two converged geometries (Fig. 6.5b) is shown in Fig. 6.5.

GADGET geometry: With GADGET, a reduction of Φ by 20.8° (of the 26.4° relative to the first minimum) was found, almost reaching $\Phi = 57.6°$ of **Test 1** again. An energy as low as in the previous two GADGET calculations was found (−0.08 eV).

VASP geometry: This time, the extreme initial tilt angle of $\Phi = 78.7°$ led to a modification of the geometry also with the "native" VASP optimizer. Not the whole molecule reduced its tilt angle, but only the lower phenyl ring (78.7° → 74.0°). For the upper ring it even increased to 85.9° in order to stay bonded to the lower ring with - in terms of Cartesian coordinates - as little atomic motion as possible; Fig. 6.5d illustrates the resulting kink. No such molecular bending was present in the initial molecular geometry (Fig. 6.5c), nor is it predicted by GADGET (Fig. 6.5e). Concerning the energy, this result is the least favorable converged geometry (+0.08 eV).

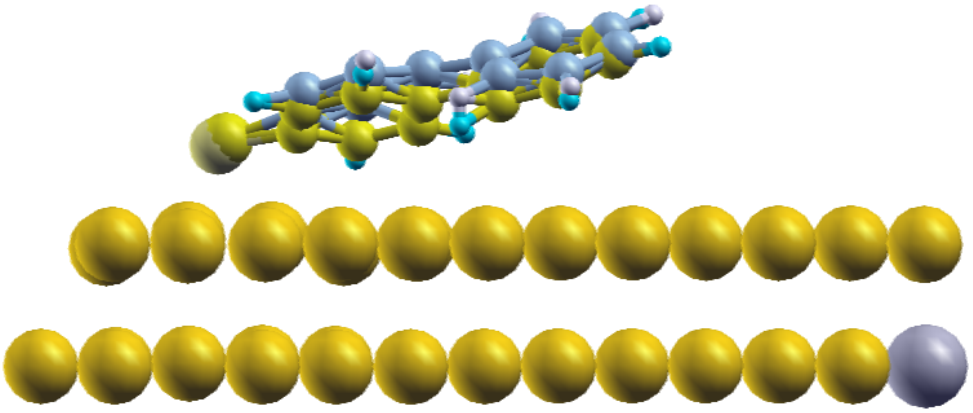

(a) Comparison of the initial geometry (golden) and the converged geometry (blue); Cartesian optimizer (bottom three Au layers not shown)

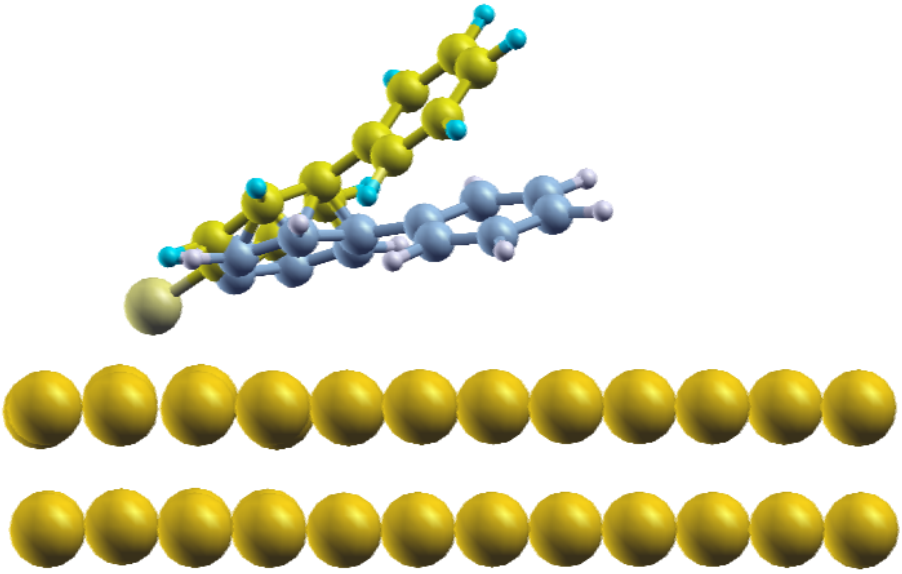

(b) Comparison of the converged geometries. Blue: Cartesian optimizer. Golden: GADGET (bottom three Au layers not shown).

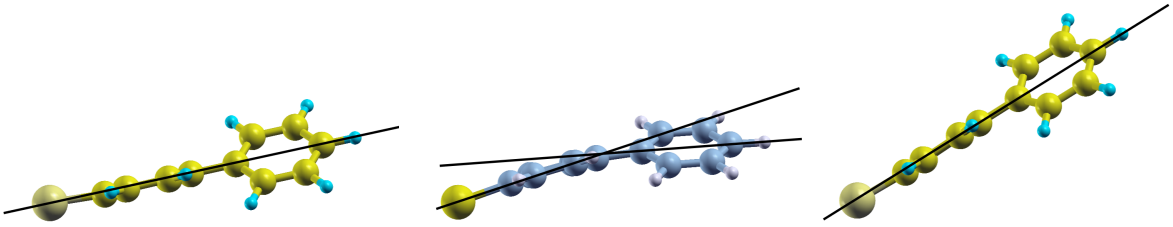

(c) Initial geometry. (d) Converged: native VASP. (e) Converged: GADGET.

Figure 6.5: **Test 2**: (a)&(b): The system Au|S|2P|H at a coverage of $\Theta = 1/8$, relaxed in Cartesian and in internal coordinates. The impact of the chosen set of coordinates is significant. Both calculations were started from the geometry depicted in golden color in Fig. 6.3, rotated by 30° around the y-axis (the sulfur atom being the center of rotation). (c)-(e): Comparison of molecular geometries in (a)&(b). The black, straight lines illustrate (the absence of) kinks along the long molecular axis.

Table 6.1: Summary of the geometry optimization calculations. Tilt angle Φ, inter-ring twist angle Θ, difference of the total energy with respect to the first VASP geometry. For a detailed description of the calculations, see text.

geometry	angles Φ	angles Θ	energy [eV]	optimizer
1st STOP	11.4°	8°	:= 0	VASP
	52.3°	37°	−0.08	GADGET
Test 1 START	65.3°	37°	+0.04	-
Test 1 STOP	65.3°	37°	−0.04	VASP
	57.6°	37°	−0.08	GADGET
Test 2 START	78.7°	37°	+1.55	-
Test 2 STOP	74.0°/85.9°	24°	+0.08	VASP
	57.9°	37°	−0.08	GADGET

Summary

Tab. 6.1 summarizes the results. Interestingly, the tilt angle is found to be quite a soft degree of freedom. Φ were probably less of a soft degree of freedom if van der Waals forces were fully accounted for in the calculations. Their importance is expected to increase at larger tilt angles. Taking the modest convergence criterion into account, the tilt angle predicted by GADGET is a quite stable quantity. Depending on the chosen initial geometry, a variation of $\approx 6°$ was found. A stricter criterion most likely reduces this (acceptable) value significantly (see next section).

6.2.2 Issues concerning the interpretation of the results

Convergence criterion.

First, the convergence criterions in GADGET and VASP calculations were not the same. Both GADGET and VASP calculations currently continue until all forces are smaller than 0.02 eV/Å. In those calculations, the dependence of the tilt angle on the initial geometry found in the GADGET optimizations will likely be reduced or may even vanish due to the stricter convergence criterion. Also, the kink that was found in the VASP geometry denoted as **Test 2** gets more pronounced in the continuation calculation.

Different optimization engines.

The optimization strategy used by GADGET is based on the direct inversion in the iterative subspace (DIIS), improved by Farkas and Schlegel (see Refs. [22, 64] for details). The method traditionally used in our group is a damped *molecular dynamics (MD)* strategy. It is suggested by the VASP manual [43] for bad initial geometries. The damped MD optimizer was chosen here in order to stick to the methodology of our group, i.e., to compare GADGET optimizations to calculations as they are performed in our group.

In this strategy, a damped equation of motion,

$$\ddot{\mathbf{x}} = -2 * \alpha \mathbf{F} - \mu \dot{\mathbf{x}} \qquad , \tag{6.5}$$

is integrated. The damping is controlled by μ and α controls the time step.

Consequently, the significant differences found in the comparison above may not solely be due to the change of the applied set of coordinates, but also due to the change of the opimization engine (DIIS vs. damped MD). A test calculation was performed using another optimizer implemented in VASP. For this purpose, a conjugant gradient method was chosen instead of damped MD (`IBRION = 2`). Compared to the damped MD optimization, a by $\approx 25°$ larger twist angle was found. In contrast, the tilt angle remained essentially unchanged just like when using damped MD. However, at least in this quick test the optimization process was found to be very unstable with respect to the forces. More than 200 ionic steps were needed to reach convergence compared to 23 steps using damped MD.

Initial Hessian matrix.

`HESSIAN = 3` is the implementation of an empirical model for the initialization of a Hessian matrix as described in Ref. [63]. Currently running calculations show that the choice of the inital Hessian greatly influences the optimization process (compare Ref. [61]). Three GADGET calculations are currently performed to differentiate the influence of the chosen coordinates from the importance of the initial Hessian (while sticking to the DIIS engine, using GADGET):

- `HESSIAN = 1 & CART = 0`: Perform the optimization in internal coordinates but initialize a diagonal Hessian in internal coordinates
- `HESSIAN = 3 & CART = 1`: Initialize a Fischer model Hessian but perfrom the optimization in Cartesian coordinates
- `HESSIAN = 0 & CART = 1`: Initialize a diagonal Hessian in Cartesian coordinates and perform the optimization in Cartesian coordinates

So far, the following trends are observed in those calculations:

- Using internal coordinates combined with a diagonal inital Hessian in internal coordinates instead of a Fischer model Hessian leads to an optimization process quite similar to when using the model Hessian. At this point, no statement can be made about the speed of convergence and the quality of the result.
- Using Cartesian coordinates and a diagonal inital Hessian in Cartesian coordinates does essentially not modify the inital geometry, comparable to the damped MD optimization.
- Using Fischer's model Hessian, both tilt and twist angle are significantly modified during the optimization also when Cartesian coordinates are used! Again, no statement can be made about the speed of convergence and the quality of the result yet. However, this calculation demonstrates the importance of the choice of the initial

Hessian. It is to be emphasized here, that the optimization is not "purely Cartesian", even if `CART` is set to `1`. Fischer's model is intrinsically based on internal coordinates as well as the step control as suggested by Farkas and Schlegel [64, 22]. It is the DIIS and the Hessian update which are performed by means of Cartesian coordinates.

Accuracy of the energy; free energy F and total energy E_0.

A consequence of using the Methfessel-Paxton occupation scheme is that the total energy E_0 is no variational quantity anymore [43]. Instead, a generalized free energy F becomes variational. However, F is physically meaningless, so that the difference $F - E_0$ has to be kept as small as possible. Convergence of F towards E_0 is reached by increasing the order N of the Methfessel-Paxton approximation (compare Sec. 3.5) [46, 68]. All calculations in this work were done at order $N = 1$.

For the results presented in Tab. 6.1, the significant difference of $F - E_0 \approx 0.02\,\text{eV}$ was found. Anyhow, for the energy differences presented in this table, differences ΔF were found to coincide with differences ΔE_0. The effect of an unconverged free energy F on the ionic forces during geometry optimizations are, however, unknown so far and will be subject to further investigations. The impact on geometry optimizations will be checked as well as potential consequences on the comparison of different geometries with respect to their total energy.

6.2.3 Interface energetics

For the geometries denoted as "1st STOP" in Tab. 6.1, the analysis known from Chapter 4 was performed. In graphs, data based on the GADGET geometry (VASP geometry) are depicted as solid black (dashed red) lines. First, the energetics of the monolayers before adsorption is studied.

The isolated monolayers

Fig. 6.6 shows the electron potential energy across both monolayer geometries (multiplied by a factor 10), together with the respective HOPS and LUPS. Tab. 6.2 summarizes the main parameters. The band gap of the GADGET geometry exceeds the one of the VASP geometry by 0.21 eV (3.29 vs. 3.08 eV; see Tab. 6.2), which is attributed to the significantly different twist angles. The difference in the tilt angle implies a notably different extension of the layer in the z-direction. Additionally, the larger tilt angle reduces the impact of the molecular dipole moment μ on ΔE_{vac} (Tab. 6.2).

Table 6.2: Step in the electron potential energy ΔE_{vac} across a 2D infinite layer of molecules and left- and right-hand side IPs (EAs) IP_{left} (EA_{left}) and IP_{right} (EA_{right}), in eV.

geometry	ΔE_{vac}	IP_{left}	IP_{right}	EA_{left}	EA_{right}
GADGET	-0.06	5.41	5.35	2.12	2.06
VASP	-0.09	5.32	5.23	2.24	2.15

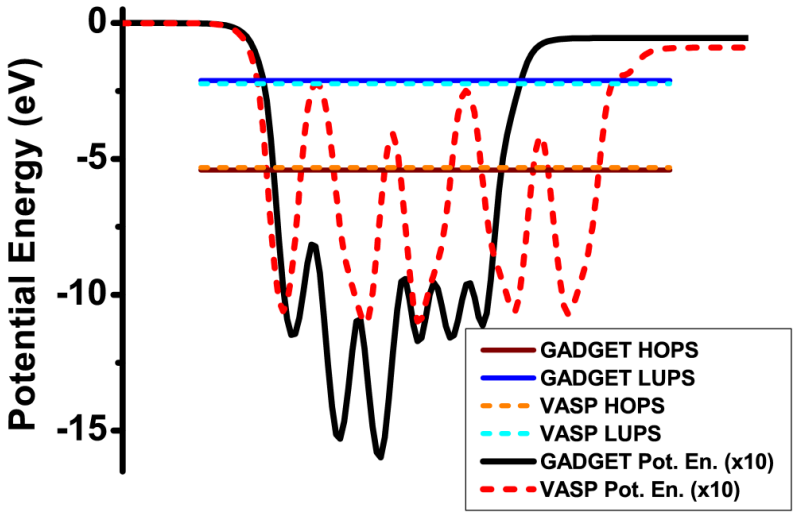

Figure 6.6: Electron potential energy across the HS|2P|H monolayer at coverage $\Theta = 1/8$ (GADGET (solid black line) and VASP (dashed black line) geometry). The systems are aligned by plotting $(E - \text{VL}_{\text{left}})$, the HOPS and LUPS are indicated by horizontal (dashed) lines. Note, that the potential energy curves are multiplied by a factor 10.

The metal|SAM systems

Fig. 6.7 shows the charge rearrangements

$$\Delta\rho = \rho_{\text{metal|SAM}} - [(\rho_{\text{metal}} + \rho_{\text{SAM}}) - \rho_{\text{H}})] \qquad [4.2]$$

integrated over the x, y-plane, $Q(z) = \int_0^z \Delta\rho(z')dz'$ and the effect of $\Delta\rho$ on the electron electrostatic energy E (Eqn.(2.5)) for both geometries. For small z-coordinates, maxima and minima are found to be at approximately the same z-coordinates in both $\Delta\rho$-plots. This similarity disappears at larger z-values. A pronounced effect of the geometry on the magnitude of the peaks is found. While the magnitude of the peaks directly at the interface is greater for the GADGET geometry, the peak magnitude decays faster with the distance from the interface for this geometry.

Except for the highest peak, less charge is shifted along the z-axis in this geometry (see Q-plot). The large tilt angle additionally reduces the charge transfer distances along the z-axis (see Q-plot at larger z-values). As an effect, the BD is reduced by 44 %.

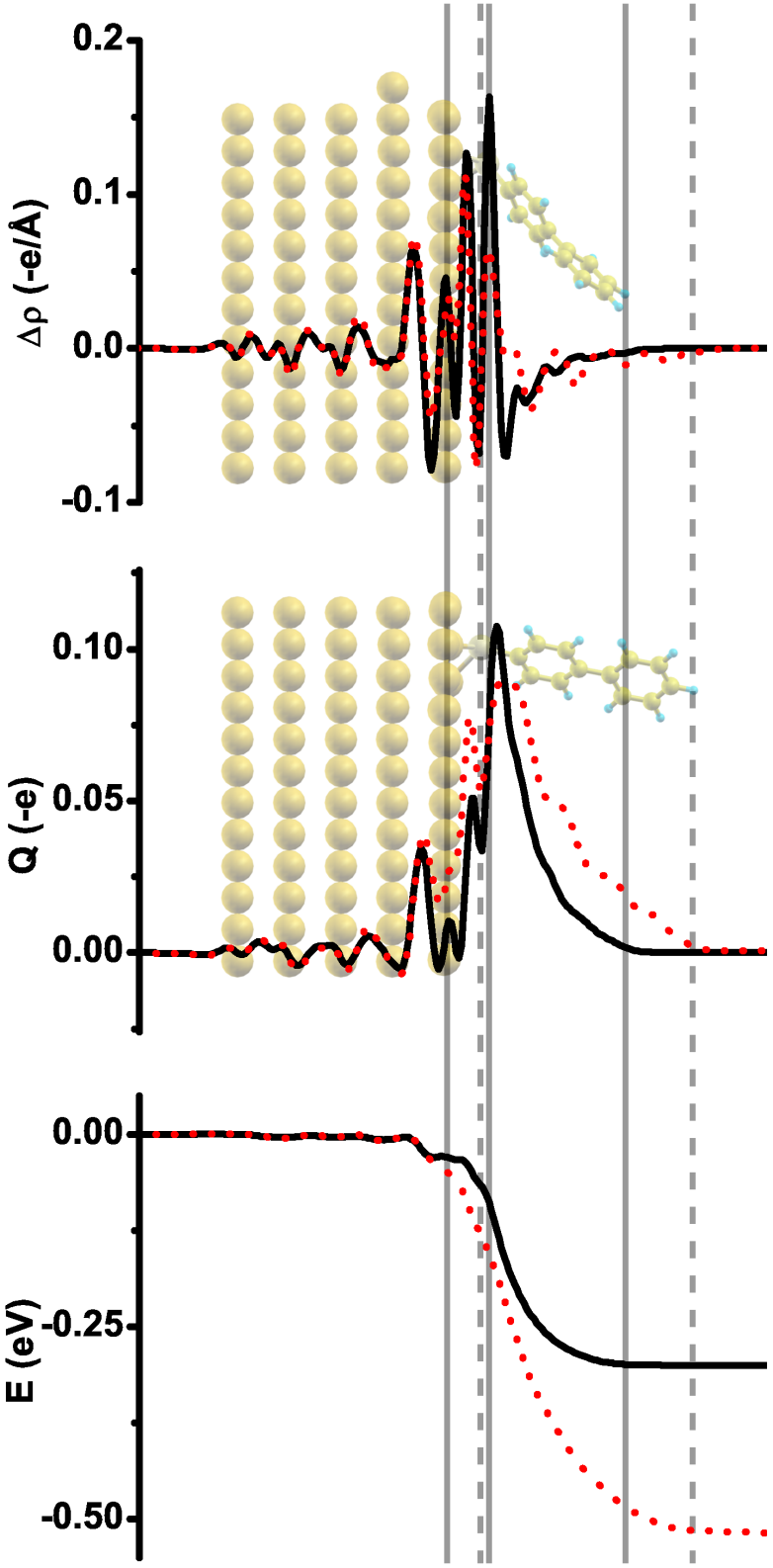

Figure 6.7: Charge rearrangements $\Delta\rho$ upon adsorption of the HS|2P|H SAM at $\Theta = 1/8$, integrated over the plane parallel to the gold surface (top panel). Below, the accumulated charge transfer $Q(z)$ is depicted. The lowermost panel shows the effect of $\Delta\rho$ on the electron electrostatic energy E. Results for the GADGET (VASP) geometry are depicted in black solid (red dashed) lines. The vertical lines and the pictures in the background serve as guide to the eye.

The main parameters are summarized in Fig. 6.8 and Tab. 6.3. As a consequence of the reduction of both, ΔE_{vac} and BD, with increasing tilt angle, also $\Delta\Phi_{\mathrm{SAM}}$ is reduced. $\Delta\Phi_{\mathrm{SAM}}$ in the GADGET geometry amounts to only approx. 58 % of the value for the VASP geometry (-0.34 vs. -0.59 eV).

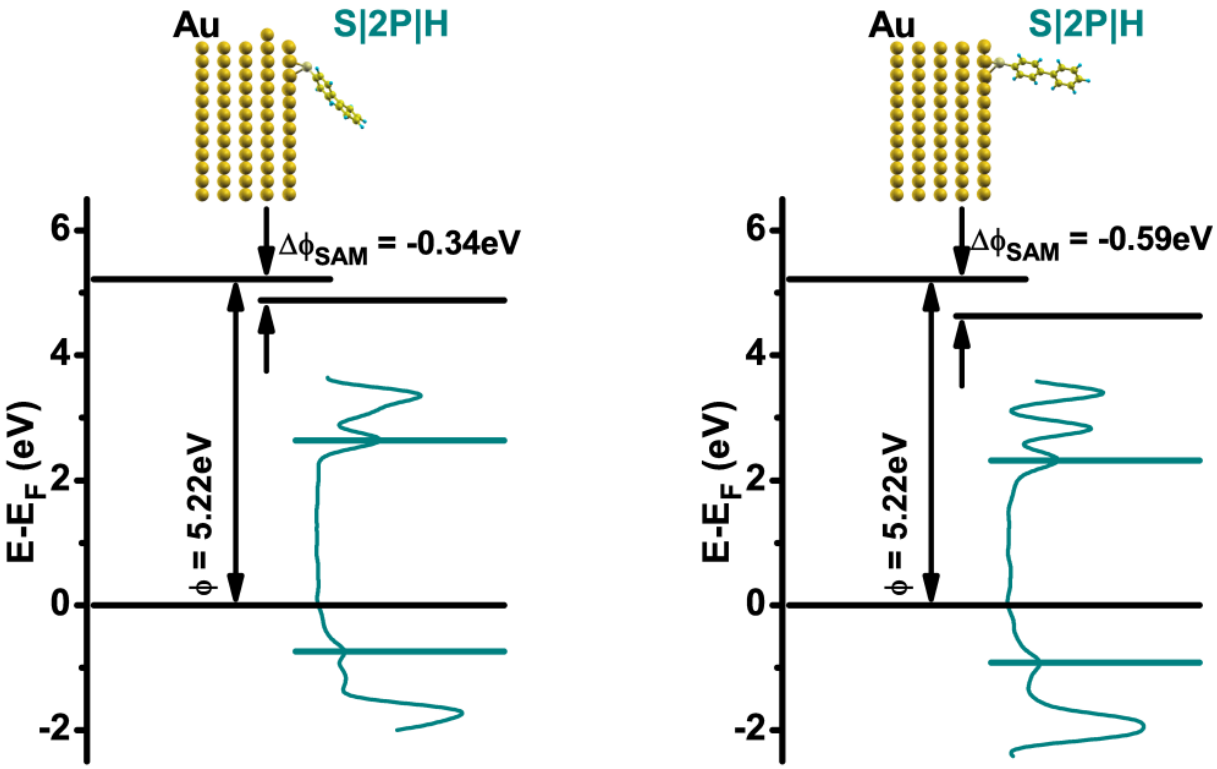

Figure 6.8: Level alignment diagrams for Au|S|2P|H at $\Theta = 1/8$ for the GADGET (left panel) and the VASP geometry (right panel). Each diagram shows the work function of the pristine gold slab (left half) and the change in the work function $\Delta\Phi_{\mathrm{SAM}}$ due to adsorption of the SAM (right half) as black, horizontal lines. Note that the energy axis is shifted by E_{F}. Additionally, the DOS projected onto the SAM region of the system is displayed as a blue line. The identified HOPS and LUPS are depicted as thin horizontal lines at the respective positions in the DOS. Symbolic representations of the systems are depicted above the diagrams.

Table 6.3: The bond dipole (BD), the work function modification $\Delta\Phi_{\mathrm{SAM}}$, ionization potential $\mathrm{IP}_{\mathrm{SAM}}$ and electron affinity $\mathrm{EA}_{\mathrm{SAM}}$ of the bonded SAM, energetic distortion of the HOPS and LUPS ($\mathrm{E}_{\mathrm{corr}}^{\mathrm{HOPS}}$, $\mathrm{E}_{\mathrm{corr}}^{\mathrm{LUPS}}$) upon bond formation and energetic distances ΔE_{HOPS} and ΔE_{LUPS} for Au|S|2P|H at $\Theta = 1/8$ for the GADGET and the VASP geometry; all quantities in units of eV.

Optimizer	BD	$\Delta\Phi_{\mathrm{SAM}}$	$\mathrm{IP}_{\mathrm{SAM}}$	$\mathrm{EA}_{\mathrm{SAM}}$	$\mathrm{E}_{\mathrm{corr}}^{\mathrm{HOPS}}$	$\mathrm{E}_{\mathrm{corr}}^{\mathrm{LUPS}}$	ΔE_{HOPS}	ΔE_{LUPS}
GADGET	-0.28	-0.34	5.62	2.24	-0.27	-0.18	-0.74	2.64
VASP	-0.50	-0.59	5.55	2.31	-0.32	-0.16	-0.92	2.32

Bibliography

[1] Hisao Ishii, Kiyoshi Sugiyama, Eisuke Ito, and Kazuhiko Seki. Energy level alignment and interfacial electronic structures at organic/metal and organic/organic interfaces. *Advanced Materials*, 11(8):605–625, 1999. 1, 4, 5, 51

[2] Antoine Kahn, Norbert Koch, and Weiying Gao. Electronic structure and electrical properties of interfaces between metals and π-conjugated molecular films. *Journal of Polymer Science: Part B: Polymer Physics*, 41(21):2529–2548, 2003. 1, 48

[3] Norbert Koch. Energy levels at interfaces between metals and conjugated organic molecules. *Journal of Physics: Condensed Matter*, 20(18):184008, 2008. doi: 10.1088/0953-8984/20/18/184008. 1

[4] Norbert Koch. Organic electronic devices and their functional interfaces. *ChemPhysChem*, 8(10):1438–1455, 2007. doi: 10.1002/cphc.200700177. 1, 12, 14, 48

[5] Annica Crispin, Xavier Crispin, Mats Fahlmann, Magnus Berggren, and William R. Salaneck. Transition between energy level alignment regimes at a low band gap polymer-electrode interfaces. *Applied Physics Letters*, 89(21):213503.1–213503.3, 2006. doi: 10.1063/1.2396899*. 1, 14, 48

[6] J.X. Tang, C.S. Lee, and S.T. Lee. Electronic structures of organic/organic heterojunctions: From vacuum level alignment to Fermi level pinning. *Journal of Applied Physics*, 101, 2007. doi: 10.1063/1.2710297*. 1, 14

[7] M.A. Baldo and S.R. Forrest. Interface-limited injection in amorphous organic semiconductors. *Physical Review B*, 64(8):085201, 2001. doi: 10.1103/PhysRevB.64.085201. 1

[8] I.D. Parker. Carrier tunneling and device characteristics in polymer light-emitting diodes. *Journal of Applied Physics*, 75(3):1656–1666, 1994. 1

[9] I.H. Campbell, J.D. Kress, R.L. Martin, D.L. Smith, N.N. Barashkov, and J.P. Ferraris. Controlling charge injection in organic electronic devices using self-assembled monolayers. *Applied Physics Letters*, 71(24):3528–3530, 1997. 1

[10] Eric L. Bruner, Norbert Koch, Amelia R. Span, Steven L. Bernasek, Antoine Kahn, and Jeffrey Schwartz. Controlling the work function of indium tin oxide: Differentiating dipolar from local surface effects. *Journal of the American Chemical Society*, 124 (13):3192–3193, 2002. 1

[11] C. Bock, D.V. Pham, U. Kunze, D. Käfer, G. Witte, and Ch. Wöll. Improved morphology and charge carrier injection in pentacene field-effect transistors with thiol-treated electrodes. *Journal of Applied Physics*, 100(11):114517.1–114517.7, 2006. doi: 10.1063/1.2400507*. 1

[12] He Yan, Qinglan Huang, Ji Cui, Jonathan G.C. Veinot, Matthew M. Kern, and Tobin J. Marks. High-brightness blue light-emitting polymer diodes via anode modification using a self-assembled monolayer. *Advanced Materials*, 15(10):835–838, 2003. doi: 10.1002/adma.200304585. 1

[13] Kamal Asadi, Fatemeh Gholamrezaie, Edsger C.P. Smits, Paul W.M. Blom, and Bert de Boer. Manipulation of charge carrier injection into organic field-effect transistors by self-assembled monolayers of alkanethiols. *Journal of Materials Chemistry*, 17(19): 1947–1953, 2007. doi: 10.1039/b617995a. 1

[14] Robert W. Zehner, Bradley F. Parsons, Richard P. Hsung, and Lawrence R. Sita. Tuning the work function of gold with self-assembled monolayers derived from X-$[C_6H_4\text{-}C{\equiv}C\text{-}]_n C_6H_4$-SH ($n$ = 0, 1, 2; X = H, F, CH_3, CF_3, and OCH_3). *Langmuir*, 15 (4):1121–1127, 1999. 1

[15] Bert de Boer and Afshin Hadipour. Tuning of metal work functions with self-assembled monolayers. *Advanced Materials*, 17(5):621–625, 2005. doi: 10.1002/adma.200401216. 1

[16] Georg Heimel, Lorenz Romaner, Jean-Luc Brédas, and Egbert Zojer. Interface energetics and level alignment at covalent metal-molecule junctions: π-conjugated thiols on gold. *Physical Review Letters*, 96(19):196806.1–196806.4, 2006. doi: 10.1103/PhysRevLett.96.196806. 1, 7

[17] Lorenz Romaner, Georg Heimel, and Egbert Zojer. Electronic structure of thiol-bonded self-assembled monolayers: Impact of coverage. *Physical Review B*, 77(4): 045113, 2008. doi: 10.1103/PhysRevB.77.045113. 1, 55

[18] Georg Heimel, Lorenz Romaner, Jean-Luc Brédas, and Egbert Zojer. Organic/metal interfaces in self-assembled monolayers of conjugated thiols: A first-principles benchmark study. *Surface Science*, 600(19):4548–4562, 2006. doi: 10.1016/j.susc.2006.07.023. 1, 9, 10, 15

[19] M.G. Betti, A. Kanjilal, C. Mariani, H. Vázquez, Y.J. Dappe, J. Ortega, and F. Flores. Barrier formation at organic interfaces in a Cu(100)-benzenethiolate-pentacene heterostructure. *Physical Review Letters*, 100(2):027601, 2008. doi: 10.1103/PhysRevLett.100.027601. 1

[20] I.G. Hill and A. Kahn. Energy level alignment at interfaces of organic semiconductor heterostructures. *Journal of Applied Physics*, 84(10):5583–5586, 1998. 1, 12

[21] Georg Heimel, Lorenz Romaner, Egbert Zojer, and Jean-Luc Brédas. Toward control of the metal−organic interfacial electronic structure in molecular electronics: A first-principles study on self-assembled monolayers of π-conjugated molecules on noble metals. *Nano Letters*, 7(4):932–940, 2007. 1, 7, 9, 10, 29, 31, 35, 36, 54, 55

[22] Tomáš Bučko, Jürgen Hafner, and János G. Ángyán. Geometry optimization of periodic systems using internal coordinates. *The Journal of chemical physics*, 122(12): 124508.1–124508.10, 2005. doi: 10.1063/1.1864932. 2, 59, 60, 61, 62, 66, 68

[23] Christian Weißmantel and Claus Hamann. *Grundlagen der Festkörperphysik*. Springer, 1979. 4

[24] A. Natan, Leeor Kronik, Hossam Haick, and Raymond T. Tung. Electrostatic properties of ideal and non-ideal polar organic monolayers: Implications for electronic devices. *Advanced Materials*, 19(23):4103–4117, 2007. doi: 10.1002/adma.200701681. 6

[25] G. Heimel, L. Romaner, E. Zojer, and J.-L. Bredas. The interface energetics of self-assembled monolayers on metals. *Accounts of Chemical Research*, 41(6), 2008. doi: 10.1021/ar700284q. 6, 7, 10

[26] Wolfgang Nolting. *Grundkurs Theoretische Physik 3: Elektrodynamik*. Springer Berlin Heidelberg, 8th edition, 2007. 6

[27] A. Kokalj. Computer graphics and graphical user interfaces as tools in simulations of matter at the atomic scale. *Computational Materials Science*, 28(2):155, 2003. doi: 10.1016/S0927-0256(03)00104-6. 8

[28] Waleed Azzam, Claus Fuxen, Alexander Birkner, Hai-Tao Rong, Manfred Buck, and Christof Wöll. Coexistence of different structural phases in thioaromatic monolayers on Au(111). *Langmuir*, 19(12):4958–4968, 2003. 15, 38

[29] K. Oura, V.G. Lifshits, A.A. Saranin, A.V. Zotov, and M. Katayama. *Surface Science, An Introduction*. Advanced Texts in Physics. Springer-Verlag Berlin Heidelberg New York, 2003. 15

[30] Wolfram Koch and Max C. Holthausen. *A Chemist's Guide to Density Functional Theory*. Wiley-VCH, 2nd edition, 2001. 17

[31] Frank Jensen. *Introduction to Computational Chemistry*. Wiley, 2nd (reprinted) edition, 2007. 17

[32] Gerd Czycholl. *Theoretische Festkörperphysik*. Springer-Lehrbuch. Springer Berlin Heidelberg, 3rd edition, 2007. 17

[33] H. Sormann and E. Schachinger. Theoretische Festkörperphysik. Script, 2006. 17

[34] P. Hohenberg and W. Kohn. Inhomogeneous electron gas. *Physical Review Letters*, 136(3B):B864–B871, 1964. 17

[35] J. F. Janak. Proof that $\partial E/\partial n_i = \epsilon_i$ in density-functional theory. *Physical Review B*, 18(12):7165–7168, 1978. 18

[36] R.O. Jones and O. Gunnarson. The density functional formalism, its applications and prospects. *Reviews of modern physics*, 61(3):689–756, 1989. 18

[37] John P. Perdew and Yue Wang. Accurate and simple analytic representation of the electron-gas correlation energy. *Physical Review B*, 45(23):13244–13249, 1992. 18

[38] M. Dion, H. Rydberg, E. Schröder, D.C. Langreth, and B.I. Lundqvist. Van der Waals density functional for general geometries. *Physical Review Letters*, 92(24): 246401, 2004. doi: 10.1103/PhysRevLett.92.246401. 18

[39] Priya Sony, Peter Puschnig, Dmitrii Nabok, and Claudia Ambrosch-Draxl. Importance of van der Waals interaction for organic molecule-metal junctions: Adsorption of thiophene on Cu(110) as a prototype. *Physical Review Letters*, 99(17):176401, 2007. doi: 10.1103/PhysRevLett.99.176401. 18

[40] R. Stowasser and R. Hoffmann. What do the Kohn-Sham orbitals and eigenvalues mean? *Journal of the American Chemical Society*, 121(14):3414–3420, 1999. 18

[41] A. Savin, C.J. Umrigar, and X. Gonze. Relationship of Kohn–Sham eigenvalues to excitation energies. *Chemical Physics Letters*, 288(2-4):391–395, 1998. 18

[42] G. Kresse and J. Furthmüller. Efficient iterative schemes for ab initio total-energy calculations using a plane-wave basis set. *Physical Review B*, 54(16):11169–11186, 1996. 19

[43] Georg Kresse and Jürgen Furthmüller. VASP the GUIDE. Internet, March 2007. http://cms.mpi.univie.ac.at/vasp/vasp/. 19, 26, 27, 34, 35, 61, 66, 68

[44] G. Kresse and D. Joubert. From ultrasoft pseudopotentials to the projector augmented-wave method. *Physical Review B*, 59(3):1758–1775, 1999. 19, 35

[45] Hendrik J. Monkhorst and James D. Pack. Special points for Brillouin-zone integrations. *Physical Review B*, 13(12):5188–5192, 1976. 20

[46] M. Methfessel and A.T. Paxton. High-precision sampling for Brillouin-zone integration in metals. *Physical Review B*, 40(6):3616–3621, 1989. 23, 24, 25, 68

[47] Georg Heimel, Lorenz Romaner, Egbert Zojer, and Jean-Luc Brédas. A theoretical view on self-assembled monolayers in organic electronic devices. In Paul L. Heremans, Michele Muccini, and Eric A. Meulenkamp, editors, *Organic Optoelectronics and Photonics III. Proceedings of the SPIE, Volume 6999*, pages 699919–699919–12, 2008. 29

[48] John P. Perdew, Kieron Burke, and Matthias Ernzerhof. Generalized gradient approximation made simple. *Physical Review Letters*, 77(18):3865–3868, 1996. 35

[49] G.P. Charbonneau and Y. Delugeard. Biphenyl: three-dimensional data and new refinement at 293 K. *Acta Crystallographica Section B*, 33(5), 1977. 39, 40

[50] G.P. Charbonneau and Y. Delugeard. Structural transition in polyphenyls. III. Crystal structure of biphenyl at 110 K. *Acta Crystallographica Section B*, 32(5), 1976. 39

[51] Georg Koller, Stephen Berkebile, Joachim R. Krenn, Falko P. Netzer, Martin Oehzelt, Thomas Haber, Roland Resel, and Michael G. Ramsey. Heteroepitaxy of organic-organic nanostructures. *Nano Letters*, 6(6):1207–12, 2006. doi: 10.1021/nl060629l. 39

[52] Daniel Käfer, Lars Ruppel, and Gregor Witte. Growth of pentacene on clean and modified gold surfaces. *Physical Review B*, 75(8):085309.1–085309.14, 2007. doi: 10.1103/PhysRevB.75.085309. 39

[53] M.H. Lemée, L. Toupet, Y. Délugeard, J.C. Messager, and H. Cailleau. Crystal structure and thermal-motion analysis of 4,4'-difluorobiphenyl. *Acta Crystallographica Section B*, 43(5):466–470, Oct 1987. doi: 10.1107/S0108768187097477. URL http://dx.doi.org/10.1107/S0108768187097477. 40, 41

[54] J. Wąsicki, A.V. Belushkin, V.G. Khomenko, I. Natkaniec, Yu.V. Telezhenko, and T. Wasiutyński. Low-temperature structure and lattice dynamics of 4,4',-difluorobiphenyl. *Physica Status Solidi (B)*, 145(2):445–453, 1988. 40, 41

[55] C. Ambrosch-Draxl, P. Puschnig, R. Resel, and G. Leising. Electronic properties of PPP-oligomers investigated from first-principles. *Synthetic Metals*, 101(1-3):673–674, 1999. 48

[56] Peter Puschnig and Claudia Ambrosch-Draxl. Density-functional study for the oligomers of poly(*para*-phenylene): Band structures and dielectric tensors. *Physical Review B*, 60(11):7891–7898, 1999. 48

[57] Gregor Witte, Simon Lukas, Paul S. Bagus, and Christof Wöll. Vacuum level alignment at organic/metal junctions: "Cushion" effect and the interface dipole. *Applied Physics Letters*, 87, 2005. doi: 10.1063/1.2151253*. 51

[58] Péter Pulay, Géza Fogarasi, Frank Pang, and James E. Boggs. Systematic ab initio gradient calculation of molecular geometries, force constants, and dipole moment derivatives. *Journal of the American Chemical Society*, 101(10):2550–2560, 1979. 59

[59] Jon Baker, Alain Kessi, and Bernard Delley. The generation and use of delocalized internal coordinates in geometry optimization. *Journal of Chemical Physics*, 105(1): 192–212, 1996. 59, 61

[60] Géza Fogarasi, Xuefeng Zhou, Patterson W. Taylor, and Péter Pulay. The calculation of ab initio molecular geometries: Efficient optimization by natural internal coordinates and empirical correction by offset forces. *Journal of the American Chemical Society*, 114(21):8191, 1992. doi: 10.1021/ja00047a032. 59, 61

[61] Elena F. Koslover and David J. Wales. Geometry optimization for peptides and proteins: comparison of Cartesian and internal coordinates. *The Journal of Chemical Physics*, 127(23):234105, 2007. doi: 10.1063/1.2807227. 59, 67

[62] Salomon R. Billeter, Alexander J. Turner, and Walter Thiel. Linear scaling geometry optimisation and transition state search in hybrid delocalised internal coordinates. *Physical Chemistry Chemical Physics*, 2(10):2177–2186, 2000. 60

[63] Thomas H. Fischer and Jan Almlöf. General methods for geometry and wave function optimization. *Journal of Physical Chemistry*, 96(24):9768–9774, 1992. 60, 67

[64] Ödön Farkas and H. Bernhard Schlegel. Methods for optimizing large molecules. Part III. An improved algorithm for geometry optimization using direct inversion in the iterative subspace (GDIIS). *Physical Chemistry Chemical Physics*, 4(1):11–15, 2002. doi: 10.1039/b108658h. 60, 66, 68

[65] Valéry Weber, Claude Daul, and Matt Challacombe. Exchange energy gradients with respect to atomic positions and cell parameters within the Hartree-Fock Γ-point approximation. *The Journal of Chemical Physics*, 124(21):214105, 2006. doi: 10.1063/1.2207625. 61

[66] P. Pulay and G. Fogarasi. Geometry optimization in redundant internal coordinates. *Journal of Chemical Physics*, 96(4):2856–2860, 1992. 61

[67] Roland Lindh, Anders Bernhardsson, Gunnar Karlström, and Per-Åke Malmqvist. On the use of a Hessian model function in molecular geometry optimizations. *Chemical Physics Letters*, 241(4):423–428, 1995. 62

[68] Lorenz Romaner. *Modelling of Organic Semiconductorsn and their Interaction with metallic surfaces*. PhD thesis, Graz University of Technology, June 2007. 68